Vorticity-streamfunction formulation of the Navier-Stokes equations for predicting unsteady flow past bodies in arbitrary movement

Nygreen, Per Jørgen; Sørensen, Jens Nørkær; Larsen, Poul Scheel

Publication date:
1997

Document Version
Publisher's PDF, also known as Version of record

ET-PHD9702 Februar 1997

INSTITUT FOR ENERGITEKNIK
Fluid Mekanik
ISSN 1396-5611

DTU

A VORTICITY-STREAMFUNCTION FORMULATION OF THE NAVIER-STOKES EQUATIONS FOR PREDICTING UNSTEADY FLOW PAST BODIES IN ARBITRARY MOVEMENT

Per Jørgen Nygreen

DANMARKS TEKNISKE UNIVERSITET

Preface

The work presented in this dissertation is carried out during the period September 1st 1993 to February 28th 1997 at the Dept. of Energy Engineering, (former Dept. of Fluid Mechanics), Technical University of Denmark, (DTU). The study was interrupted for a half year period while the author was taking care of his new born child.

The present Ph.D. study has been carried out under guidance of Ass. Professor, Lic. techn. Jens Nørkær Sørensen, DTU, Professor Ph.D. Poul Scheel Larsen, DTU and Senior Scientist, Ph.D. Jess A. Michelsen, DTU.

This study was supported by the Danish Technical Research Council under grant STVF-5.26.16.31, and the European research programs *European Computational Aerodynamics Research Project, ECARP*, CEC Project No. 2003, CT-Nr AER2-0031 and *HELISHAPE, subtask 1.1*, CEE AER2-CT92-0047.

Figures in this dissertation are mainly located at the end of each chapter. Citation is done by a number e.g. [1] and all references are gathered last in this dissertation. References to sections are done by e.g. chapter 3 section (3.5.1) denoting section 5.1 in chapter 3. Symbols are explained first time they appear and is for completeness listed in a nomenclature list.

Technical University of Denmark,
Lyngby, February 28, 1997

Per Jørgen Nygreen

Abstract

A 2-dimensional vorticity-streamfunction formulation of the Reynolds averaged Navier-Stokes equations in primitive variable form has been considered for laminar and turbulent flow past airfoils. A new method for establishing boundary distribution of vorticity and streamfunction at limiting boundaries of the calculation domain is suggested. The method guarantees a unique pressure distribution on a solid body.

Eddy-viscosity has been introduced for modeling the Reynolds stresses and is calculated by use of the algebraic model of Baldwin & Lomax, the 1-equation turbulence models of Baldwin & Barth and Spalart & Allmaras and the 2-equation $K-\omega$-BSL/SST turbulence model by Menter. Correct implementation of the turbulence models has been regarded for flow past a flat plate with finite thickness and rounded leading edge.

The developed Navier-Stokes solver has been used for computing stationary and in-stationary laminar and turbulent airfoil flow with great success.

Laminar flow situations has been regarded by three different flow situations past a NACA 0012 airfoil: A low incidence case, an impulsive start at high incidence and an airfoil oscillating in pitch between 0^o and 20^o incidence.

Turbulent airfoil flows past a stationary Onera-A airfoil was considered profoundly at incidences 10.1^o, 13.3^o, 17.6^o, 25^o and 40^o and comparisons are made with experiment at incidences below 25^o. The Michel criterion was used to predict transition positions in some cases.

Dynamic stall was considered by calculating a light and deep stall case for a NACA 0015 airfoil with the different turbulence models. The light stall case is characterized by a mean incidence equal 11.37^o and a variation of the incidence of 7.55^o. The reduced frequency was 0.102. The deep stall case is characterized by a mean incidence equal 19.58^o and a variation of the incidence of 6.83^o. The reduced frequency was 0.154. In both cases the Reynolds number was $1.5 \cdot 10^6$ and the results was compared with experiments.

Abstrakt (in Danish)

En 2-dimensional strømfunktion-vorticity formulering af de tidsmidlede Navier-Stokes ligninger i primitiv variabel formulering er blevet benyttet til beregning af laminære og turbulente aerodynamiske strømninger. En ny metode er foreslået til at beregne fordeling af vorticity og strømfunction på randene af et beregningsdomaine. Metoden vil garantere en entydig trykfordeling på overfladen at et fast legeme.

Reynolds spændingerne er blevet modelleret v.hj.a. en eddy-viskositet som er blevet beregnet ved den algebraiske turbulens model af Baldwin & Lomax, 1-lignings modellerne af Baldwin & Barth og Spalart & Allmaras og 2-lignings turbulens modellen af Menter. Implemteringen af turbulens modellerne blev verificeret gennem strømning over en flad plade med endelig tykkelse og afrundet forkant.

Den udviklede Navier-Stokes løser er med succes andvendt til at beregne både stationære og instationære, laminære og turbulente strømninger.

Tre forskellige laminære strømninger over et NACA 0012 vingeprofil er blevet undersøgt: en ved lav indfaldsvinkel, en impulsiv start ved høj indfaldvinkel og et oscillerende profil med en indfaldsvinkel, som varierer imellem 0^o og 20^o.

En turbulent strømning over et Onera-A vingeprofil er blevet undersøgt, specielt ved indfaldsvinklerne 10.1^o, 13.3^o, 17.6^o, 25^o og 40^o. Sammenligninger med eksperimenter er foretaget for indfaldsvinkler mindre end 25^o. Michel criteriet blev i nogle tilfælde benyttet til at beregne transition punkter.

Dynamisk stall er undersøgt for to forskellige tilfælde, et let stall og et kraftigt stall. Det lette stall tilfælde er kendetegnet ved en middel indfaldsvinkel på 11.37^o og en variation af indfaldsvinklen på 7.55^o. Den reducerede frekvens var 0.102. Det kraftige stall tilfælde er kendetegnet ved ved en middel indfaldsvinkel på 19.58^o og en variation af indfaldsvinklen på 6.83^o. Den reducerede frekvens var 0.154. I begge tilfælde var Reynolds tallet lig $1.5 \cdot 10^6$ og resultaterne blev sammenlignet med experimenter.

Contents

Preface i

Abstract iii

Abstrakt (in Danish) vii

Contents vii

1 Introduction 1

2 Vorticity-streamfunction formulation of the Navier-Stokes equations 7

2.1 Governing equations 8

2.2 Boundary conditions for the $\gamma - \psi$ formulation 12

2.2.1 Boundary conditions in simply connected domains . . . 15

2.2.2 Boundary conditions in multiply connected domains . . 16

2.3 Discretization of the governing equations and solution procedure 20

2.3.1 Numerical treatment of the boundary conditions for airfoil flows 24

2.3.2 Solution procedure 26

2.4 Variants of the vorticity-streamfunction formulation 28

2.4.1 3-Dimensional forms of the vorticity formulation 28

2.4.2 2-Dimensional variants of the vorticity streamfunction formulation 29

2.5 Aerodynamic forces and boundary layer parameters 32

3 Turbulence modeling 35

3.1 Short review of turbulence modeling 35

3.2 The Baldwin-Lomax turbulence model 39

3.3 The Baldwin-Barth turbulence model 41
3.4 The Spalart-Allmaras turbulence model. 43
3.5 The K-ω / K-ϵ turbulence model 45
3.5.1 The K-ω-BSL turbulence model 45
3.5.2 The K-ω-SST turbulence model 48
3.6 Transtion 48
3.7 Turbulence models applied in non-inertial systems 50

4 Turbulent flow past a flat plate **51**
4.1 Numerical setup 52
4.2 Results for flow past a flat plate with finite thickness 53
4.3 Summary 55

5 Laminar flow past airfoils **59**
5.1 Laminar stationary flow past a NACA 0012 airfoil 60
5.2 Impulsive start of a NACA 0012 airfoil 60
5.3 Flow past an oscillating NACA 0012 airfoil 63
5.4 Summary 65

6 Turbulent flow past a stationary airfoil **75**
6.1 General discussion of flow past an Onera-A airfoil 76
6.2 Results for the Onera-A airfoil up to incidence equal **17.6°** . . 78
6.2.1 Transition considerations 81
6.3 Results for the Onera-A airfoil at incidences higher than **17.6°** 82
6.4 Summary 84

7 Turbulent flow past an airfoil oscillating in pitch **91**
7.1 General description of dynamic stall 91
7.2 Numerical setup for calculation of dynamic stall 94
7.3 Dynamic light stall airfoil flows 95
7.4 Dynamic deep stall airfoil flows 97
7.5 Summary 99

Conclusion **107**

Bibliography **111**

Nomenclature **119**

A Derivation of the vorticity-pressure coupling at a solid wall 127

Chapter 1

Introduction

The rapid increase in computer performance has made computational fluid dynamic in three space dimension possible at quite low cost. Even though 3-dimensional Navier-Stokes solvers has matured to a level where the predicted results can strongly be relied upon, there is still a need for studying 2-dimensional flows.

The present work concerns the development of a Navier-Stokes solver applicable for predicting unsteady flow past a bodies in arbitrary movement f.i. flow past a wind turbine blade or flow past a helicopter rotor in a forward flight situation. These flow situations are by nature

- 3-dimensional
- unsteady
- compressible
- govern by turbulence

It is authors believe that no limitation is present today which could disable a computation of a flow consisting of the phenomenon listed above although such a computation in many cases be would unnecessary. A time true 3-dimensional, compressible and turbulent Navier-Stokes computation would require very power full computers and still the computation time would be very long. In many case a steady state solution is aimed at and in these cases acceleration techniques such as local time stepping is typically applied. A special variant of a local time stepping algorithm has been developed for

unsteady flow calculations in 2-dimension [66]. Whether this scheme can be applied for 3-dimensional flow is not known by the author but in general it should be possible.

For the flow past helicopter rotors and wind turbines it is general believed that a local 2-dimensional approach, eventual with boundary conditions taken from a 3-dimensional potential flow solution, will be able to describe as local quantities satisfactorily as long as the flow is only mildly separated. The flow past helicopter rotors is in some situations characterized by unsteady separation influenced by a pitching movement of the airfoil relative to the oncoming flow. This phenomenon is called dynamic stall and is more broadly defined as the unsteady separation on an airfoil subject to a forced movement typically of sinusoidal form where the lift-stall is significant different from static stall.

Dynamic stall is maybe one of the less understood phenomena within fluid dynamic and it is believed that in order to fully understand the nature of the processes one must regard the very small structures of the flow. Many attempts to study dynamic stall has been done by experiments mainly in 2-dimensional flows where methods such as Particle Image Velocimetry can be very use full [42] but the very fine resolution in time and space afforded by numerical simulations is much better suited for looking into such details, if the physics is adequately captured.

In real flows the influence of 3-dimensional flow effects on dynamic stall are only limited known [28] but in order to understand the physics of the unsteady separation process a 2-dimensional approach is well suited due to relative simplicity of the flow situation compared to a 3-dimensional flow. At the same time it is widely believed that the knowledge gained by such 2-dimensional computations can be applied when a understanding of the 3-dimensional flow situation is looked for.

Considering helicopter rotors the flow was previously govern by compressible effects mainly close to the tip of the rotors but today the tip speed are gradually decreased demanded to some extend by a lowering of emitted noise. Even though the tip speed has decreased some compressible effects are still present. As dynamic stall is not fully understood it is general accepted that an attempt to gain knowledge can be by use of an incompressible approach even though the phenomenon has a large dependency of compressible effects. The source of this approach is perhaps of practical reasons because experiments are more easily conducted in a incompressible flow situation.

For many years wind turbines has been studied at the the Dept. of Energy

Engineering where this Ph.D. study has been carried out. Flow past wind turbines has always been characterized by nearly incompressible flow and the present work is related to the afore mentioned research where a demand of studying the effects of unsteady incompressible flow past airfoils are present.

Airfoil flows has in many situations been studied profoundly for compressible flows due to a very large commercial interest. By this a large effort has previously been put into solving the compressible 2-dimensional Navier-Stokes equation. Mainly the convective terms has been investigated profoundly and a lot of very good numerical schemes such as shock fitting/capturing and fluctuation splitting schemes has been constructed for the solution of the Euler/Navier-Stokes equations [22]. In these approaches the viscous terms are typically treated as source terms to the Euler equations. The Euler equations for compressible fluids are some how easier to solve because a strong coupling between the pressure and the continuity equation is present.

Today incompressible flows are becoming more and more interesting and many of the techniques, such as upwinding of the convective terms, applied in compressible flow solvers are applied in incompressible flow solvers. Solution of the incompressible Navier-Stokes equations was previously considered very difficult because the coupling between pressure and a solenoidal velocity field vanish. Different approaches has been suggested in the past where the artificial compressibility method maybe is the most direct connection to the compressible Navier-Stokes equations. A scheme original invented for the compressible Euler/Navier-Stokes equations has with great luck been applied to the artificial compressibility method [14].

The most common way of solving the incompressible, turbulent Navier-Stokes equations is based on the equations put in primitive variables. In the 2-dimensional case this results in two momentum equations for the velocity components, (U, V), and a Poisson equation for the pressure, p. The latter, which is normally obtained by applying the divergence operator on the momentum equations, must be strongly coupled to continuity since mass conservation are assured only if a correct pressure distribution is obtained.

An alternative formulation consists of eliminating the pressure by taking the curl of the momentum equations and introducing the vorticity, γ, and a streamfunction, ψ. As a result, the resulting system consists of only one momentum equation (for transport of vorticity) and a Poisson equation for the streamfunction. The main advantage of introducing a streamfunction is that continuity is automatically satisfied. In the laminar case the formulation

of the Navier-Stokes equations in $\gamma-\psi$ variables is relatively straightforward, whereas in the turbulent case the time-averaging may cause some difficulties.

As mentioned previously one of the intentions with this Ph.D. study was to develop a Navier-Stokes solver for predicting unsteady flows. In case of a transient or a general unsteady 2-dimensional flow situations the vorticity-streamfunction formulation is a very attractive alternative to the primitive variable formulation of the Navier-Stokes equations. For the primitive variable formulation a linearization of the momentum equations must be performed if an implicit schemes are used. In the vorticity-streamfunction formulation, which consist of a transport equation for vorticity and a Poisson equation for the streamfunction, the two equations can easily be solved coupled or the two equations can be applied in a simple predictor-corrector scheme. In these cases no linearization is needed.

When introducing vorticity and streamfunction the boundary conditions are no longer straight forward defined as in the case with the primitive variable formulation of the Navier-Stokes equations. Many attempts to utilize the vorticity-streamfunction method in the past has failed because boundary conditions was imposed that provided a solution that did not satisfy the primitive form of the Navier-Stokes equations.

In case of a dynamic stall situation the airfoil is no longer fixed relative to an inertial coordinate system and the flow can profitably be calculated by applying the vorticity-streamfunction formulation in a coordinate system fixed relative to the airfoil. The vorticity-streamfunction formulation of the Navier-Stokes equation are very simple to apply when a non-inertial reference system is considered. In this case the vorticity-streamfunction formulation is basically identical to the formulation in an inertial reference system.

Even though a tendency of decreasing the tip speed of helicopter rotors, (and by this the Reynolds number), are found turbulence is still present and plays a major role in the flow. The same large influence of turbulence is found for wind turbines and many other flows of practical interest. Turbulence is by nature full 3-dimensional and is typically studied in a three levels order, Direct Numerical Simulation (DNS), Large Eddy Simulation (LES), and Reynolds Averaging (RA). DNS is often applied to 3-dimensional flows and the LES and RA method is often utilized in 2-dimensional flow situations with great success. Where the DNS method is a valuable tool in studying the nature of the large and small details of a turbulent flow, the LES method serves as a method between DNS and RA providing time varying results for the larger structures of the flow.

The RA method has proven to predicts local and global mean values of turbulent flows in 2-dimensional flows very well when the Reynolds stresses are modeled by an eddy-viscosity concept. A lot of different but good methods ranging from algebraic to transport models are available for calculating the eddy-viscosity. The intention of this Ph.D. study was not to investigate the nature of turbulence and by this it is natural to adopt the RA averaging techniques with the eddy-viscosity concept.

Application of a RA method has in past often been linked to a flow situation with a stationary mean flow and the method has proven to mimic the time averaged flow properties well. When applying a RA method to a non stationary flow situation the borders between the LES and the RA are some how vanishing because the final mathematical outcome look similar and both methods utilize an eddy-viscosity concept.

When considering aerodynamic flows transition from laminar to turbulent flow often plays a dominant role in the flow. Different method has been applied in the past for computing the location at which a laminar flow begins to undergo transition to a turbulent flow where the e^n-method has been widely discussed [10]. More typically used are the empirical methods based on experiment where the Michel criterion [38] is frequently used in literature.

As some of the ideas with this Ph.D. study was to perform computations of unsteady, turbulent and incompressible flow past bodies in arbitrary movement at least to some level of approximation we can summarize the demands to the Navier-Stokes solver by the following items

- 2-dimensional
- unsteady
- incompressible
- modeling of turbulence

The relative simplicity of the vorticity-streamfunction formulation of the Navier-Stokes equations for predicting 2-dimensional unsteady flow past bodies in arbitrary movement was the argument for choosing this approach. At the same time the vorticity-streamfunction formulation is by the author regarded as a very interesting formulation. As only a turbulence modeling was aimed at and not an investigation of the nature of turbulence the eddy-viscosity concept was adopted.

This dissertation deals with the development of a time true 2-dimensional Navier-Stokes solver applicable for calculating laminar and turbulent flows in both inertial and non-inertial frames of references. The work is to some extend based on a laminar vorticity-streamfunction based Navier-Stokes solver where boundary conditions was imposed without paying any attention to the fact that the solution also should satisfy the Navier-Stokes equations in terms of U, V, P.

Chapter 2

Vorticity-streamfunction formulation of the Navier-Stokes equations

In this chapter an vorticity-streamfunction, $\gamma - \psi$, algorithm developed as a part of the authors Ph.D. study is described. The governing equations and their solution will be presented, the time-averaging problem will be addressed. Boundary conditions for the vorticity-streamfunction methods is discussed an a new method to determine boundary conditions will be presented in detail. Finally a review of related work will be given in order to relate the present work with the present status of solving the Navier Stokes equation in terms of vorticity. In the next chapter the utilized turbulence models will be described and in the following chapters results obtained with the developed code will be shown.

2.1 Governing equations

In a coordinate system rotating with angular velocity Ω_i, the primitive variables formulation of the Navier-Stokes equations are written as

$$\frac{\partial \tilde{u}_i}{\partial t} + \tilde{u}_j \frac{\partial \tilde{u}_i}{\partial x_j} + 2\epsilon_{ijk}\Omega_j \tilde{u}_k + \epsilon_{ijk}\epsilon_{klm}\Omega_j \Omega_l x_m + \epsilon_{ijk}\dot{\Omega}_j x_k$$

$$= -\frac{1}{\rho}\frac{\partial \tilde{p}}{\partial x_i} + \nu \frac{\partial^2 \tilde{u}_i}{\partial x_j \partial x_j} \quad , \tag{2.1}$$

$$\frac{\partial \tilde{u}_i}{\partial x_i} = 0 \quad , \tag{2.2}$$

where $\tilde{u}_i$ is the velocity relative to the rotating coordinate system at a point x_i. Here a tilde denotes the instantaneous value of the variable at (x_i, t), ν is the kinematic viscosity and ρ denotes the density of the fluid.

Decomposing the instantaneous velocity, $\tilde{u}_i$, into a mean flow component U_i and a velocity fluctuation u_i, we get that

$$\tilde{u}_i = U_i + u_i \quad , \tag{2.3}$$

where the time-average of U_i is defined by

$$U_i = \frac{1}{T}\int_{t_0}^{t_0+T} \tilde{u}_i dt \quad . \tag{2.4}$$

The averaging period, T, has to be sufficiently large in order to model correctly the small-scale turbulence. On the other hand, in order to maintain the time-terms in the equations it has to be much smaller than a characteristic rotation period. Employing the same decomposition for the pressure and taking the time average of Navier-Stokes equations, results in the Reynolds momentum equations (here defined in a rotating coordinate system)

$$\frac{\partial U_i}{\partial t} + U_j \frac{\partial U_i}{\partial x_j} + 2\epsilon_{ijk}\Omega_j U_k + \epsilon_{ijk}\epsilon_{klm}\Omega_j \Omega_l x_m + \epsilon_{ijk}\dot{\Omega}_j x_k$$

$$= -\frac{1}{\rho}\frac{\partial P}{\partial x_i} + \nu \frac{\partial}{\partial x_j}\left[(1 + \frac{\nu_t}{\nu})\frac{\partial U_i}{\partial x_j}\right], \tag{2.5}$$

$$\frac{\partial U_i}{\partial x_i} = 0, \tag{2.6}$$

where the Reynolds stresses have been modeled by the eddy-viscosity, ν_t,

$$-\overline{u_i u_j} = \nu_t \frac{\partial U_i}{\partial x_j}. \tag{2.7}$$

For the $\gamma - \psi$ formulation, one can either first apply the rotation operator and next make the Reynolds averaging or first make the Reynolds averaging and next define the vorticity as the curl of the time-averaged velocity components. In the first approach it is necessary to model vorticity-velocity correlations f.i. by [55]

$$\overline{u_i \gamma'} = -\nu_t \frac{\partial \gamma}{\partial x_i} \ , \tag{2.8}$$

where the vorticity has been decomposed as

$$\tilde{\gamma} = \gamma + \gamma' \ . \tag{2.9}$$

In the other approach, which is the one followed here, the vorticity is defined as

$$\gamma = \frac{\partial V}{\partial x} - \frac{\partial U}{\partial y}, \tag{2.10}$$

Considering a coordinate system rotating with an angular frequency, Ω_{rot}, the 2-dimensional form of eq.(2.5) in vorticity-streamfunction formulation is

$$\frac{\partial}{\partial t}\left[\gamma + 2\Omega_{rot}\right] - \frac{\partial}{\partial x}\left(\frac{\partial \psi}{\partial y}\gamma\right) + \frac{\partial}{\partial y}\left(\frac{\partial \psi}{\partial x}\gamma\right)$$

$$= \nu \frac{\partial^2}{\partial x^2}\left[\left(1 + \frac{\nu_t}{\nu}\right)\gamma\right] + \nu \frac{\partial^2}{\partial y^2}\left[\left(1 + \frac{\nu_t}{\nu}\right)\gamma\right] + S_\gamma, \tag{2.11}$$

where

$$S_\gamma = 2\left[\frac{\partial U}{\partial y}\left(\frac{\partial^2 \nu_t}{\partial x^2}\right) - \left(\frac{\partial U}{\partial x} - \frac{\partial V}{\partial y}\right)\left(\frac{\partial^2 \nu_t}{\partial x \partial y}\right) - \frac{\partial V}{\partial x}\left(\frac{\partial^2 \nu_t}{\partial y^2}\right)\right] \ . \tag{2.12}$$

This term is seen to depend only on second derivatives of the eddy-viscosity and may be omitted.

From the definition of the streamfunction

$$U = -\frac{\partial \psi}{\partial y}, \qquad V = \frac{\partial \psi}{\partial x} \ , \tag{2.13}$$

and the definition of vorticity, a Poisson equation is obtained for ψ

$$\frac{\partial^2 \psi}{\partial x^2} + \frac{\partial^2 \psi}{\partial y^2} = \gamma \ . \tag{2.14}$$

By introducing the chord length of the airfoil, c, as the characteristic length scale, and the free stream velocity, U_0, as the characteristic velocity scale, the variables are made dimensionless as shown below

$$(x^*, y^*) = \left(\frac{x}{c}, \frac{y}{c}\right), \quad (U^*, V^*) = \left(\frac{U}{U_0}, \frac{V}{U_0}\right), \quad \Omega^*_{rot} = \Omega_{rot}\frac{c}{U_0} \ ,$$

$$t^* = t\frac{U_0}{c}, \quad \psi^* = \psi\frac{c}{U_0}, \quad \gamma^* = \gamma\frac{c}{U_0}.$$

The superscript $*$ will be left out from hereon. Introducing the Reynolds number, $Re = U_o c/\nu$, and neglecting S_γ, the resulting system of governing equations are given as

$$\frac{\partial}{\partial t}\left[\gamma + 2\Omega_{rot}\right] - \frac{\partial}{\partial x}\left(\frac{\partial \psi}{\partial y}\gamma\right) + \frac{\partial}{\partial y}\left(\frac{\partial \psi}{\partial x}\gamma\right) = \frac{1}{Re}\left[\frac{\partial^2 \epsilon\gamma}{\partial x^2} + \frac{\partial^2 \epsilon\gamma}{\partial y^2}\right], \tag{2.15}$$

$$\frac{\partial^2 \psi}{\partial x^2} + \frac{\partial^2 \psi}{\partial y^2} = \gamma, \tag{2.16}$$

where $\epsilon = 1 + \nu_t/\nu$. In the following ν_t/ν will be denoted ν_t^* where the superscript $*$ indicate a non-dimensionalized eddy-viscosity, which is not non-dimensionalized with U_0 and c.

A transformation from the Cartesian coordinates, (x, y), to a boundary-fitted curvilinear mesh is carried out by introducing the general transformation

$$\xi = \xi(x, y) \ , \quad \eta = \eta(x, y) \ ,$$

where (ξ, η) denotes the coordinates in the curvilinear system. The transformation Jacobian is given as

$$\boldsymbol{J} = \begin{vmatrix} \xi_x & \xi_y \\ \eta_x & \eta_y \end{vmatrix},$$

with the inverse transformation

$$\boldsymbol{J}^{-1} = \begin{vmatrix} x_\xi & x_\eta \\ y_\xi & y_\eta \end{vmatrix}.$$

The Jacobian may also be expressed as

$$\boldsymbol{J} = \frac{Cofactor(\boldsymbol{J}^{-1})}{J^{-1}}$$

where

$$J^{-1} = \left| \boldsymbol{J}^{-1} \right| = x_\xi y_\eta - x_\eta y_\xi,$$

which results in the metric coefficients

$$\xi_x = \frac{y_\eta}{J^{-1}}, \quad \xi_y = -\frac{x_\eta}{J^{-1}}, \quad \eta_x = -\frac{y_\xi}{J^{-1}}, \quad \eta_y = \frac{x_\xi}{J^{-1}}.$$

Applying the chain-rule of differentiation, after some manipulations the governing equations (2.15) and (2.16) are formulated in strong conservative form as follows

$$[J^{-1}(\gamma + 2\Omega_{rot})]_t - \left(\frac{\partial \psi}{\partial \eta}\gamma\right)_\xi + \left(\frac{\partial \psi}{\partial \xi}\gamma\right)_\eta$$

$$= \frac{1}{Re}\left[\left[C^1\frac{\partial(\epsilon\gamma)}{\partial \xi}\right]_\xi + \left[C^2\frac{\partial(\epsilon\gamma)}{\partial \eta}\right]_\eta + \left[C^3\frac{\partial(\epsilon\gamma)}{\partial \eta}\right]_\xi + \left[C^3\frac{\partial(\epsilon\gamma)}{\partial \xi}\right]_\eta\right], \quad (2.17)$$

$$\left(C^1\frac{\partial \psi}{\partial \xi}\right)_\xi + \left(C^2\frac{\partial \psi}{\partial \eta}\right)_\eta + \left(C^3\frac{\partial \psi}{\partial \eta}\right)_\xi + \left(C^3\frac{\partial \psi}{\partial \xi}\right)_\eta = J^{-1}\gamma, \quad (2.18)$$

where

$$C^1 = \frac{x_\eta^2 + y_\eta^2}{J^{-1}}, \quad C^2 = \frac{x_\xi^2 + y_\xi^2}{J^{-1}}, \quad C^3 = -\frac{y_\eta y_\xi + x_\eta x_\xi}{J^{-1}}. \tag{2.19}$$

The streamfunction is now defined as

$$\frac{\partial \psi}{\partial \xi} = V^c, \quad \frac{\partial \psi}{\partial \eta} = -U^c \ , \tag{2.20}$$

where superscript c denotes contra-variant components

$$U^c = y_\eta U - x_\eta V \ , \quad V^c = -y_\xi U + x_\xi V \ . \tag{2.21}$$

For later use it should be stresses that the convective terms of eq.(2.17) of course can be written as

$$-\left(\frac{\partial \psi}{\partial \eta}\gamma\right)_\xi + \left(\frac{\partial \psi}{\partial \xi}\gamma\right)_\eta = (U^c\gamma)_\xi + (V^c\gamma)_\eta \ . \tag{2.22}$$

The reason wy the formulation eq.(2.17) typically is preferred is that the velocity to some extend is a redundant variable for the vorticity-streamfunction formulation of the Navier-Stokes equations.

An important feature of the vorticity-streamfunction formulation is that it maintains it basic formulation if one considers a fixed or an arbitrary moving coordinate system. This is easily recognized by considering eq.(2.17), from which it is seen that the only difference between a fixed system and an oscillating one is the angular acceleration term within time derivative of vorticity.

2.2 Boundary conditions for the $\gamma - \psi$ formulation

In the following section boundary conditions for the vorticity-streamfunction formulation will be outlined. In order to ease the discussion, the description is done only in an inertial frame of reference. Later, the boundary conditions in a non-inertial system will be shown.

When considering a description of a flow in terms of vorticity the following theorem, as stated by Wu and Gulcat [63], is very use full

Theorem 1 *The motion of a fluid which fills infinite space and is at rest at infinity is determined when the values of the vorticity are known at all points of the space. Similarly, the motion of a fluid which occupies a limited simply connected region is determined when the values of the vorticity are known at all points in the region and the values of the normal velocity are known at all points of the region's boundary. In the case of a multiply connected region, the values of the circulation in the several circuits of the region must also be known.*

This theorem [1] is expressed mathematically by

$$\nabla \times \vec{U} = \vec{\gamma} \ , \ \ \nabla \cdot \vec{U} = 0 \ . \tag{2.23}$$

The equivalence of eq.(2.23) in terms of the streamfunction for a 2-dimensional flow situation is

$$\nabla^2 \psi = \gamma \ , \tag{2.24}$$

where the specification of the normal velocity at limiting boundaries provide the streamfunction at these boundaries. As the theorem states, and also the Poisson equation, the vorticity needs only to be known in the interior of the calculation domain in order to determine the velocities. When solving for vorticity by use of the transport equation boundary conditions for γ are typically specified in some sense. These boundary conditions for vorticity are by this often referred to as *extraneous boundary condition*. The Poisson equation for ψ can provide a velocity field which is not a solution to the Navier-Stokes equation even though the vorticity field is, if wrong boundary conditions for ψ are imposed. This means that only one set of boundary conditions for the Poisson equation will provide a solution to the Navier-Stokes equations and that the Navier-Stokes equations in terms of $\gamma - \psi$ must consist of the transport equation for vorticity and the Poisson equation for the streamfunction with additional constrains.

Examining the transport equation for vorticity, eq.(2.15), the transport process consist of convection and diffusion, processes which cannot generate or destroy vorticity but only redistribute vorticity. Consequently vorticity is introduced in the fluid domain only at the solid/fluid interface [47] where the no-slip boundary condition provides a mechanism for the generation or depletion of vorticity. This form a contrast to the Navier-Stokes equations

[1] When solving the U, V, P formulation of the Navier-Stokes equations circulation also plays an important role [56].

in primitive variable form where boundary conditions at solid walls can be derived from the momentum equations for U and V and support the concept of the extraneous boundary condition for vorticity.

The Navier-Stokes equations in primitive variable form can be regarded to establish conditions which must be full filled for the vorticity-streamfunction formulation to be complete. The pressure has been removed mathematically from the momentum equations when defining the $\gamma - \psi$ formulation but has to be inherent in Navier-Stokes equations in terms of vorticity. From the Navier-Stokes equations we can derived the following conditions which must be satisfied for the solution found by the vorticity-streamfunction formulation [64]

$$\nabla \times \mathcal{L}(\vec{U}) = 0 \ , \ \vec{n} \times \mathcal{L}_A(\vec{U}) = -\vec{n} \times \nabla P_A \ , \tag{2.25}$$

$$\nabla^2 P = -\nabla \cdot \mathcal{L}(\vec{U}) \ , \ \left(\frac{\partial P}{\partial n}\right)_A = -\vec{n} \cdot \mathcal{L}(\vec{U})_A \ , \tag{2.26}$$

and

$$\left(\frac{\partial P}{\partial s}\right)_A = -\vec{s} \cdot \mathcal{L}(\vec{U})_A \ , \tag{2.27}$$

where A denotes a solid wall boundary and $\vec{n}$ is the normal vector to this and $\vec{s}$ is tangential to the solid wall. $\mathcal{L}(\vec{U})$ is

$$\mathcal{L}(\vec{U}) = \frac{\partial \vec{U}}{\partial t} + \vec{U} \cdot \nabla \vec{U} - \nu \nabla \cdot (\epsilon \nabla \vec{U}) \ . \tag{2.28}$$

As will be shown below the expression in eq.(2.27) is used as a global constrain of the vorticity boundary condition. In the past, as noted by Hafez [20], many attempts to utilize the vorticity-streamfunction formulation of the Navier-Stokes equation was done by only regarding the transport equation for vorticity and the Poisson equation for the streamfunction and not paying any attention to eq.(2.27).

Consider a domain $O = I \cup A \cup B$, with the interior denoted by I and the boundaries by $A \cup B$, where A is boundaries with a no slip condition and B is other boundaries limiting O. The time-averaged Navier-Stokes equation written in terms of vorticity and streamfunction, completed by the no-slip boundary condition in a general domain, is [49]

$$\frac{D\gamma}{Dt} = \frac{1}{Re}\nabla^2(\epsilon\gamma) \ \ in \ I \ , \tag{2.29}$$

$$\nabla^2 \psi = \gamma \ in \ O \ , \tag{2.30}$$

$$\frac{\partial \psi}{\partial n} = 0 \quad on \ A \ , \tag{2.31}$$

$$\psi = const \ on \ A \ , \tag{2.32}$$

$$\oint \frac{\partial P}{\partial s} ds = 0 \quad in \ O \ , \tag{2.33}$$

where n is the direction normal to the solid wall A and s is the direction tangential to this. Eq.(2.31) is the no-slip condition and eq.(2.32) is the demand of no penetration. Eq.(2.33) is, when used along solid walls, actually a constraint of vorticity [2]

$$\oint \frac{\partial P}{\partial s} ds = -\frac{1}{Re} \oint \frac{\partial}{\partial n} [\epsilon \gamma] \, ds = 0 \ . \tag{2.34}$$

In the following the utilized boundary conditions will be described and in order to ease the discussion of the prescribed boundary conditions for airfoil calculations, boundary conditions in a simple flow configuration will be presented first.

2.2.1 Boundary conditions in simply connected domains

As an example of a simply connected domain, consider the channel flow sketched on the figure below

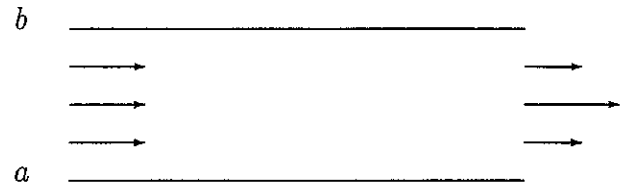

Figure 2.1: *Flow through a channel*

As $\Delta\psi$ equals the flow between two point, the difference in streamfunction between the upper and lower surface is

$$\psi_b - \psi_a = \int_a^b (U dy - V dx) = Q \ , \tag{2.35}$$

[2] In appendix A, eq.(2.34) is derived for a laminar flow case.

where Q is the flow rate through the channel and x is the direction tangential to the wall and y is the direction normal to this. No penetration through the sides of the channel, $(V = 0)$, demands a constant ψ along the two surfaces a and b. Assumptions made for the outlet velocity will provide the streamfunction by the integral relation eq.(2.35).

The boundary condition for γ can be made up by utilizing the definition of γ

$$\gamma = \nabla^2 \psi \ . \tag{2.36}$$

As the only boundary condition enforced, (by putting ψ equal to a constant along a and b), are the no-penetration condition, the vorticity and streamfunction must be specified in order to assure the no-slip condition. The vorticity at the boundaries must be specified in a way that full fill the pressure condition eq.(2.33) and the streamfunction must obey $\partial\psi/\partial y = 0$ at solid walls. [3]

2.2.2 Boundary conditions in multiply connected domains

In the following boundary conditions for the $\gamma - \psi$ formulation in multiply connected regions will be presented. For external flows, such as the ones around airfoils, the domain is not simply connected and an idealized case of such a flow is shown in the figure below.

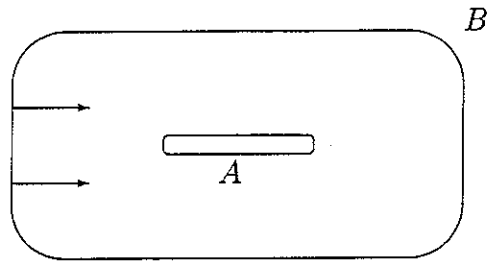

Figure 2.2: *Flow past a solid body*

[3] In [39] the no-slip condition was imposed by applying a second order accurate forward difference approximation to $\gamma_a = \frac{\partial \psi}{\partial y}$

$$\psi_2 = \frac{1}{4}[3\psi_a + \psi_3] \ ,$$

where index $2, 3$ denotes the two points closest to the boundary a.

For this flow configuration the solution of the Poisson equation for ψ consist of the boundary value problem

$$\nabla^2\psi = \gamma \quad \psi = \begin{Bmatrix} \psi_B(s) = \psi_B(s_0) + \int_{s_0}^{s}(U \cdot dy - V \cdot dx) \\ \psi_A = Constant \ \ on \ \ A \end{Bmatrix} \tag{2.37}$$

where s is the direction tangential to the outer boundary and s_0 is an arbitrary point located on the outer surface. Assuming known velocities at the outer boundary, $\psi_B(s)$ is known except for the value of $\psi_B(s_0)$. $\psi_B(s_0) - \psi_A$ equals, (in accordance with eq.(2.35)), the flow rate through a section of the flow domain emanating from the airfoil and ending at the outer boundary at s_0. In symmetric flow situations this flow rate is normally known but in a general case f.i. a cambered airfoil or an airfoil with incidence this flow rate is unknown. By this we can choose either ψ_A or $\psi_B(s_0)$ freely but not both. In this case it becomes necessary to solve the additional integral equation, eq.(2.33), assuring a continuous pressure distribution along the surface A. Evaluating the Navier-Stokes equations along the surface A, we get the following relation for a turbulent flow

$$\oint \frac{\partial P}{\partial s} ds = -\frac{1}{Re} \oint \frac{\partial}{\partial n} [\epsilon\gamma] \, ds = 0 \ , \tag{2.38}$$

where s now is the direction tangential to the airfoil and n is the direction normal to this. This condition may be looked upon as a "viscous Kutta condition" in which a vorticity flux is formed on the surface of the airfoil in order to assure a continuous pressure distribution and constrains the extraneous boundary condition for γ. The condition is related to the fact that the actual value of the streamfunction at the airfoil is not known a priori. Thus the value of the streamfunction on the airfoil has to be adjusted in order to satisfy eq.(2.38).

Suppose a solution to the Poisson equation, which satisfy eq.(2.38), is obtained by solving

$$\nabla^2\psi = \overline{\gamma} \tag{2.39}$$

$$\psi = \overline{\psi}_A \ \ on \ \ A \tag{2.40}$$

$$\psi = \overline{\psi}_B \ \ on \ \ B \ . \tag{2.41}$$

Here an overline means values which make the solution satisfy the viscous Kutta condition eq.(2.38) and will be denoted as the correct values. In accordance with the discussion concerning eq.(2.37) we are free to choose one

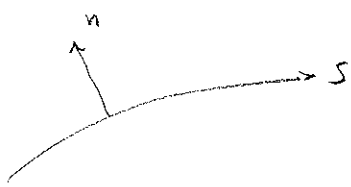

of the boundary conditions for ψ. By choosing the streamfunction at the outer boundary B and arbitrary putting the value of $\psi_A = 0$ a solution ψ_1 can be determined from

$$\begin{aligned} \nabla^2\psi_1 &= \overline{\gamma} && (2.42)\\ \psi_1 &= 0 \ on \ A && (2.43)\\ \psi_1 &= \overline{\psi}_B \ on \ B\,. && (2.44) \end{aligned}$$

This system of equations will in general not satisfy the viscous Kutta condition, eq.(2.38), even though it is a solution obtained with the correct vorticity inside the domain. Then it becomes necessary to produce an additional vorticity on the surface of the airfoil. This is accomplished by solving eq.(2.16) with a zero right-hand side, i.e. $\nabla^2\psi^+ = 0$, subject to the boundary condition, $\psi^+ = \overline{\psi}_A$, on the surface. Such a solution can be established by a vorticity distribution on the surface. Inside the domain the solution can not contain vorticity due to the zero right hands side in the Poisson equation. Since the relation between the vorticity and the streamfunction is linear in ψ we can regard the difference between the correct solution, ψ, and the streamfunction ψ_1, $(\psi^+ = \psi_1 - \psi)$, found by solving the Poisson equation with the correct vorticity but with wrong boundary conditions

$$\begin{aligned} \nabla^2(\psi^+) &= \nabla^2(\psi_1) - \nabla^2(\psi) = 0 && (2.45)\\ \psi^+ &= -\overline{\psi}_A \ on \ A && (2.46)\\ \psi^+ &= 0 \ on \ B\,. && (2.47) \end{aligned}$$

This system can be normalized by $\overline{\psi}_A$

$$\begin{aligned} \nabla^2(\psi^+) &= 0 && (2.48)\\ \psi^+_A &= 1 \ on \ A && (2.49)\\ \psi^+_B &= 0 \ on \ B\,, && (2.50) \end{aligned}$$

so that the actual solution is determined by superposition

$$\psi = \psi_1 - \chi \cdot \psi^+\,, \qquad (2.51)$$

where χ is found by the viscous Kutta condition. As the streamfunction ψ^+ can be calculated prior to any time stepping and is common for a given geometric flow configuration, ψ^+ is called the Base-function.

A comprehension of the Base-function can be established by re-inventing it. The velocity field is made up by summing the velocities found from ψ_1 and ψ^+. At the outer boundary we demand no change in the net flow through the domain due to the Base-function providing a constant streamfunction ψ_B^+. We arbitrarily fix the value to zero i.e. $\psi_B^+ = 0$ and by this choice the streamfunction at the outer boundary, ψ_B, will never be altered. As the flow through the outer boundary due to the Base-function is zero and no penetration is required through the airfoil, ($\psi_A^+ = Constant$), we can normalize the system and get $\psi_A^+ = 1$. At the airfoil we must demand the no slip condition also for the Base-function. Such a flow can be established by a surface vortex sheet with a vorticity located at the surface evaluated by

$$\gamma_A^+ = \lim_{h \to 0} \int_0^h \gamma^+ dn \,. \tag{2.52}$$

Such a solution will introduce circulation into the flow and is by this in accordance with the theorem stated in the beginning of the chapter. If the boundary cells, (the cells adjacent to the airfoil), are small enough we can estimate and distribute the vorticity due to the Base-function in these cells. By distributing γ_A^+ over the boundary cells we will be able to calculate normal derivatives of γ^+ and we have established a relationship between the Base-function and vorticity so the actual value of χ can be calculated from

$$\frac{1}{Re} \oint \frac{\partial}{\partial n} [\epsilon\gamma] \, ds + \chi \cdot \frac{1}{Re} \oint \frac{\partial}{\partial n} \left[\epsilon\gamma^+\right] ds = 0 \,. \tag{2.53}$$

In the next section it will be shown how γ^+ is calculated.

Introducing additional vorticity in the boundary cells provides a way to calculate the vorticity at the same time station as the rest of the domain when considering time intergration of the Navier-Stokes equation. When solving the transport equation, eq.(2.15), the boundary conditions for γ evaluated at $t = t^k$ is utilized in the time integration. By this the vorticity in the interior domain is found at $t = t^{k+1}$ and the vorticity in the boundary cells at $t = t^k$. When evaluating

$$\frac{\partial \left(\epsilon\gamma^{k,k+1}\right)}{\partial n} \tag{2.54}$$

with vorticity at different time station it is no longer certain that the viscous Kutta condition should be satisfied. On the other hands, when adding additional vorticity to the boundary cells by an amount which make the solution

satisfying the viscous Kutta condition and the Poisson equation the total boundary vorticity must be the correct one at $t = t^{k+1}$.

The above derivation of the Base-function is also valid in a rotating frame of reference. As will be shown later on the boundary value problem for ψ has a similar form in the rotating frame of reference. The viscous Kutta condition, on the other hand, now also contain terms arising from the change of reference system. In accordance with eq.(2.5) the viscous Kutta condition is in a non-inertial system rotating around Origo

$$\frac{1}{Re}\oint \frac{\partial}{\partial n}[\epsilon\gamma]\,ds + \chi \cdot \frac{1}{Re}\oint \frac{\partial}{\partial n}\left[\epsilon\gamma^{+}\right] ds = \oint \left[\frac{\Omega_{rot}^2}{2}\frac{\partial}{\partial s}[x^2+y^2] + \dot{\Omega}_{rot}[xy_s - yx_s]\right] ds \ , \tag{2.55}$$

where s and n respectively is the direction tangential and normal to A.

Even though the method was never tested the authors idea to utilize the Base-function in a domain with more than one solid body should be mentioned. In a domain with N solid bodies, N viscous Kutta conditions must be satisfied and N Base-functions must be defined. All Base-functions must guarantee no net inflow through the inflow boundary giving $\psi^{+}_{B,n=1,N} = 0$. Requirement of influencing the $n'th$ body boundary conditions only by the $n'th$ Base-function gives zero streamfunction on all bodies except the $n'th$,

$$\nabla^2 \psi^{+}_{m=1,N} = 0 \tag{2.56}$$

$$\psi^{+}_{B,m=1,N} = 0 \tag{2.57}$$

$$\psi^{+}_{A,m=1,N} = \begin{Bmatrix} \psi^{+}_{A,m} = 1 & m = n \\ \psi^{+}_{A,m} = 0 & m \neq n \end{Bmatrix} \tag{2.58}$$

where n is the body in consideration.

2.3 Discretization of the governing equations and solution procedure

In Figs.(2.3) and (2.4) the computational domain and the boundaries are sketched. The Cartesian coordinate system is located with its Origo at the leading edge, the x-direction along the chord of the airfoil, and the y-direction normal to this. The airfoil is embedded in a C-grid with ξ-coordinates defining the airfoil and outer contour of the mesh. The transformation to the

boundary-fitted mesh is performed such that $\Delta\xi = \Delta\eta = 1$, with $\xi \in [1, nx]$ and $\eta \in [-1, ny]$ with i, j as the counters in ξ and η directions respectively.

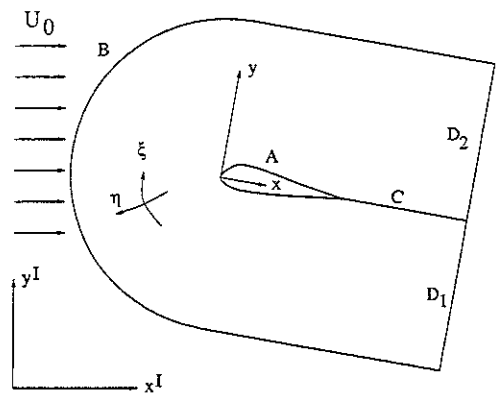

Figure 2.3: *C-grid topology. U_0 is the on-coming flow, superscripts I denotes inertial frame of reference and A,B and D denotes limiting boundaries of the c-grid. C is an overlapping region*

Owing to the C-topology of the grid, the boundaries C_1 and C_2 define an overlapping region between the lower and upper part, respectively, of the grid behind the airfoil, see Fig.(2.4). Here C_1 is located at $\eta = -1$ with $\xi \in [1, nk]$ and C_2 is located at $\eta = -1$ with $\xi \in [nx - nk + 1, nx]$, where $\xi = nk$ and $\xi = nx - nk + 1$ define $\xi =$ constant grid lines emanating from the trailing edge. To assure that the variables and their first and second derivatives are continuous across the common grid line, $\eta = 1$, periodic boundary conditions are defined as follows

$$f_{i,j-2} = f_{nx+1-i,j}, \qquad f_{nx+1-i,j-2} = f_{i,j}, \qquad j = 1, 2 \ , \tag{2.59}$$

which are to be satisfied for both the streamfunction and the vorticity.

At airfoils or other bodies with discontinuity geometries vorticity is singular where the boundary is not differential. A staggered topology is utilized, in order to avoid the singular behavior of γ, with ψ located in the cell-vertex and γ located in cell-centers. The transformed equations is discretized by a Finite-Volume / Finite-Difference method, applying central discretization for Laplacians and upwinding for convective terms. For the former one the algebraic form of the discretization can be found in [23].

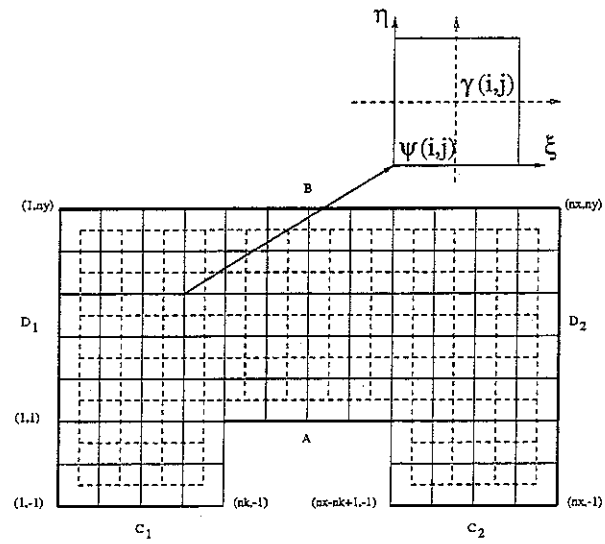

Figure 2.4: *C-grid topology calculation domain*

The upwinding scheme for the convective terms has been formulated in a classical Finite-Volume way [13] [22]

$$\frac{\partial(U^c\gamma)}{\partial\xi} = [a^+(U^c\gamma)^+ + a^-(U^c\gamma)^-]_e - [a^+(U^c\gamma)^+ + a^-(U^c\gamma)^-]_w \ , \quad (2.60)$$

with

$$a^+ = \frac{U^c + |U^c|}{|U^c|} \ , \ a^- = \frac{U^c - |U^c|}{|U^c|} \ . \quad (2.61)$$

Index e and w defines east and west faces respectively, where the east face is positioned at $(i+1/2)$ referring to Fig.(2.4) and the indexing for γ. The cell face values are found by the MUSCL approximation [22], [65]) for $\phi = U\gamma$

$$\begin{aligned} \phi_e^+ &= \phi_i + \frac{1}{4}(1-\kappa)(\phi_i - \phi_{i-1}) + \frac{1}{4}(1+\kappa)(\phi_{i+1} - \phi_i) \\ \phi_e^- &= \phi_{i+1} - \frac{1}{4}(1+\kappa)(\phi_{i+1} - \phi_i) - \frac{1}{4}(1-\kappa)(\phi_{i+2} - \phi_{i+1}) \ . \end{aligned} \quad (2.62)$$

All the results shown in this dissertation are calculated with $\kappa = -1$ giving a linear reconstruction

$$\phi_e^+ = \frac{3}{2}\phi_i - \frac{1}{2}\phi_{i-1} \ , \ \phi_w^+ = \frac{3}{2}\phi_{i-1} - \frac{1}{2}\phi_{i-2} \ , \quad (2.63)$$

which in case of parallel flow reduced to

$$\phi_e^+ - \phi_w^+ = \frac{1}{2}(3\phi_i - 4\phi_{i-1} + \phi_{i-2}) \ , \tag{2.64}$$

resulting in a second order finite-difference scheme [45]. Please notice the difference from utilizing a classic finite-difference second order upwind scheme and the cell face method in cells with in- or outflow at two adjacent cell faces. The former one is unstable and gives rice to wiggles in the solution for non-stationary airfoil flows.

The MUSCL approximation needs special attention in the cell next to solid walls for normal derivatives. Here a one sided finite difference, based on points inside the domain only, must be applied as no information for points located inside the wall is available.

Boundary conditions for vorticity in cells next to the solid wall is determined by evaluating eq.(2.18) at the first cell adjacent to the airfoil. Discretizing eq.(2.18) by a finite-difference method results in the algebraic form

$$\begin{aligned} J^{-1}\gamma_{i+1/2,1/2} = C^1_{i+1,1/2} \ &\cdot \ \left(\psi_{i+3/2,3/2} - \psi_{i+1/2,3/2}\right) - \\ C^1_{i,1/2} \ &\cdot \ \left(\psi_{i+1/2,3/2} - \psi_{i-1/2,3/2}\right) + \\ C^2_{i+1/2,2} \ &\cdot \ \left(\psi_{i+1/2,5/2} - \psi_{i+1/2,3/2}\right) \ , \end{aligned} \tag{2.65}$$

where the tangential velocity at the surface is put equal to zero, (index refers to grid points).

At the wall, the vorticity and its normal derivatives is found by considering a Taylor series expansion for γ_A. The first known vorticity is located in the center of the boundary cells and is denoted by index 1. The Taylor expansion away from the surface is

$$\begin{aligned} \gamma_1 &= \gamma_A + \frac{\partial \gamma_A}{\partial n}\Delta n_1 + \frac{1}{2}\frac{\partial^2 \gamma_A}{\partial n^2}(\Delta n_1)^2 \ldots \\ \gamma_2 &= \gamma_A + \frac{\partial \gamma_A}{\partial n}\Delta n_2 + \frac{1}{2}\frac{\partial^2 \gamma_A}{\partial n^2}(\Delta n_2)^2 \ldots \\ \gamma_3 &= \gamma_A + \frac{\partial \gamma_A}{\partial n}\Delta n_3 + \frac{1}{2}\frac{\partial^2 \gamma_A}{\partial n^2}(\Delta n_3)^2 \ldots \end{aligned} \tag{2.66}$$

where the first vanishing term is of fourth order. The Taylor expansion forms a quadratic system of equations,

$$(\gamma_i)^T = \boldsymbol{M} \cdot \left(\gamma_A, \frac{\partial \gamma_A}{\partial n}, \frac{\partial^2 \gamma_A}{\partial n^2}\right)^T \ , \tag{2.67}$$

where M is a matrix containing only geometry of the grid. The solution of eq.(2.67) contains the magnitude and the derivatives of the surface vorticity to be used in eq.(2.53). The Taylor series expansion is also utilized for the Base-function. Assuming γ^+ to be different from zero in the boundary cells and zero above, we still full fill $\nabla^2\psi^+ = 0$ in the calculation points next to the surface and in the rest of the calculation domain. The magnitude of γ_1^+ is found by utilizing eq.(2.66) for ψ^+. Vorticity is introduced by the Base-function because the no-slip condition is introduced in the same way as for ψ. By solving eq.(2.67) for γ_A^+ and its derivatives, the last integral in eq.(2.53) can be evaluated. Finally χ can be found as the factor which makes the sum of the two integral equal to zero and the solution can be updated.

2.3.1 Numerical treatment of the boundary conditions for airfoil flows

In the general case, the airfoil is assumed to oscillate in pitch about the axis $(x_o, 0)$ with an angle of attack given by

$$\alpha = \bar{\alpha} + \Delta\alpha \sin(f \cdot t), \tag{2.68}$$

where $\bar{\alpha}$ is the mean angle of attack, $\Delta\alpha$ the amplitude, and f is the frequency of oscillation non-dimensionalized by U_o and c. The reduced frequency which is based on the half-chord is then given by $k = \frac{1}{2}f$. The angular velocity is found by taking the time-derivative of the angle of attack

$$\Omega_{rot} = -\dot{\alpha} = 2 \cdot k \cdot \Delta\alpha \cos(2 \cdot k \cdot t) \ . \tag{2.69}$$

(The minus sign is due to the orientation of the coordinate system). The angular acceleration is given by

$$\dot{\Omega}_{rot} = -\ddot{\alpha} = -4 \cdot k \cdot \Delta\alpha \sin(2 \cdot k \cdot t) \ . \tag{2.70}$$

Denoting by superscript I a variable in the inertial frame of reference, we get the following relations

$$\psi^I = \psi + \frac{\Omega_{rot}}{2}[(x - x_o)^2 + y^2] \ , \tag{2.71}$$

$$U^I = U - \Omega_{rot} \cdot y, \quad V^I = V + \Omega_{rot} \cdot (x - x_o) \ , \tag{2.72}$$

$$\gamma^I = \gamma + 2\Omega_{rot} \ . \tag{2.73}$$

The relations between γ, ψ in an inertial and rotating frame of reference provides an easy link between boundary conditions in the rotating frame of reference and in the inertial frame of reference. Even though the governing equations are solved in the rotating frame of reference, some of the utilized boundary conditions are established in the inertial reference system and are then transformed to the rotating frame of reference.

In the non-inertial reference system the airfoil boundary A on Figs.(2.3) and (2.4), located at $\eta = 1$ and $\xi \in [nk, nx - nk + 1]$, defines a streamline. Thus, the streamfunction here takes a constant value, ψ_A, determined from the pressure compatibility condition described above.

When establishing boundary condition for ψ_B the boundary condition will first be derived in the inertial coordinate system ,(x^I, y^I), with the orthonormal basis $(\vec{e}_1^I, \vec{e}_2^I)$, accordingly to Fig.(2.3). In this coordinate system the streamfunction equals

$$\psi^I(x^I, y^I) = \psi^I(0,0) - U_0 \cdot y^I \ , \tag{2.74}$$

in the hole domain if the airfoil was not present and the on-coming flow U_0 is parallel to x^I. At the outer boundary B the velocity is assumed to be equal the undisturbed far field value. Assuming far field values along B and non-dimensionalize U_0, $\psi_B^I(x^I, y^I)$ equals

$$\psi_B^I(x^I, y^I) = -y^I \ , \tag{2.75}$$

when $\psi(0,0)$ is chosen equal to zero. At each time-station, $t = t^k$, the airfoil has in the inertial coordinate system an incidence relative to the on-coming flow α from eq.(2.68). The points (x_B, y_B) in the rotating frame of reference, with the x-axis along the chord and y-axis normal to that, is expressed in a local non-inertial coordinate system, $(\mathcal{X}, \mathcal{Y})$ with basis vectors $\vec{e}_1$ parallel to $\vec{e}_1^I$ and $\vec{e}_2$ parallel $\vec{e}_2^I$

$$\mathcal{X}_B = x_B \cdot cos(\alpha) + y_B \cdot sin(\alpha) \tag{2.76}$$

$$\mathcal{Y}_B = -x_B \cdot sin(\alpha) + y_B \cdot cos(\alpha) \ . \tag{2.77}$$

As the $(\mathcal{X}, \mathcal{Y})$ coordinate system is rotating with the angular velocity Ω_{rot} the streamfunction in this coordinate system is

$$\psi_B = -y^I - \frac{\Omega_{rot}}{2}[(\mathcal{X}_B - \mathcal{X}_o)^2 + (\mathcal{Y}_B)^2] \ , \tag{2.78}$$

where also x_0 is expressed relatively to $(\vec{e}_1, \vec{e}_2)$.

As the far field velocity is supposed to be ir-rotational, no vorticity at the inflow boundary in the inertial system reference is present. In the rotating frame of reference the vorticity equals

$$\gamma_B = -2\Omega_{rot} \ . \tag{2.79}$$

The flow out of the calculation domain through boundary D^1 and D^2, (Figs.(2.3) and (2.4)), are supposed to be dominated only by convection processes. This is of course only true when the boundaries D^1 and D^2 are located very far downstream of the airfoil. When doing airfoil calculations the outflow boundary is typically located 12 chord lengths or more away and expirements with different boundary conditions lead to the conclusion that the wake normally was disappeared before reaching the outflow boundary. The applied boundary condition for vorticity is derived from

$$J^{-1}\frac{\partial \gamma_D}{\partial t} + \frac{\partial U_0^c \gamma}{\partial \xi} + \frac{\partial V_0^c \gamma}{\partial \eta} = 0 \ , \tag{2.80}$$

where the far field values of the velocity is assumed present. Assuming small time variations in vorticity and an orientation of the grid lines nearly along the oncoming flow direction lead to take

$$\frac{\partial \gamma_D}{\partial \xi} = 0 \ . \tag{2.81}$$

A consistent boundary condition for ψ_D with the boundary condition for γ_D is to apply far field values also at the outlet in accordance with eq.(2.78). This boundary condition will at the same time guarantee that no global violation is done to the mass continuity of the flow.

If the airfoil is not oscillating the reduced frequency, k, is zero and all the above boundary conditions is still valid. This means that the non-oscillating airfoil flow can be viewed as a special case of an oscillating airfoil flow.

2.3.2 Solution procedure

The transport equation for γ and the Poisson equation for ψ are solved uncoupled. In general the algebraic equations resulting from the discretization

are solved by the Alternating Direction Implicit, ADI, method by Peaceman and Rachford [44]. In symbolic form the ADI method is

$$2 \cdot \frac{Q^{k+1/2} - Q^k}{\Delta t} - L_\xi^{k+1/2}(Q) = L_\eta^k(Q) + \mathcal{P}^k \tag{2.82}$$

$$2 \cdot \frac{Q^{k+1} - Q^{k+1/2}}{\Delta t} - L_\eta^{k+1}(Q) = L_\xi^{k+1/2}(Q) + \mathcal{P}^k \ , \tag{2.83}$$

where Q can be γ or ψ, L is the operator resulting from the discretization, superscript k defines the time station and $\mathcal{P}$ is a source term arising from the cross derivatives due to the coordinate transformation. For the vorticity transport equation the ADI scheme is second order in time. For the Poisson equation, where an artificial time dependent term has been added, the optimum time step for a sequence of N consecutive iterations is calculated by a Wachspress routine [58].

Points located at the intersection line, C at Fig.(2.3), is solved implicitly. The matrix arising from L_η contains of-diagonal elements destroying the tri-diagonal structure normally established by central discretization of Laplacians. A numerical algorithm developed at DTU [1] was utilized to enable implicit solving for points at the intersection line.

When utilizing the upwind scheme, eq.(2.60), the tri-diagonal structure are maintained by adding the outer-band elements to the right hand side of the algebraic system of equations. This will of course reduce the time accuracy of the ADI scheme when applied to the transport equation for vorticity but as will be shown in the next chapters, the solution strategy are still able to calculate rapid time variating flows.

One time step with the algorithm is established by the following procedure. Assume γ is known at $t = t^k$. An eddy viscosity is calculated by one of the turbulence models outlined in the precedent chapter followed by advancing the transport eq.(2.15) one time step. Then the Poisson equation eq.(2.16) is solved by the Wachspress algorithm. The viscous Kutta condition is applied and ψ is updated, $(\psi = \overline{\psi} + \psi^+)$, together with the vorticity in the boundary cells and the solution is now known at $t = t^{k+1}$. The time advancing algorithm can be viewed as a predictor-corrector method with the transport equation for γ as the predictor and the Poisson equation plus the Base function as the corrector.

When a stationary solution is aimed at a measure of how far the solution is from being stationary or converged is found by consider the following

convergence criterion

$$Res = \frac{\sum_{n=1}^{n=ntot} (\gamma^{k+1} - \gamma^k)}{\overline{\gamma}\Delta t} \ , \ \overline{\gamma} = \frac{\sum_{n=1}^{n=ntot} \left|\gamma^{k+1}\right|}{ntot} \tag{2.84}$$

where *ntot* is equal to the total number of point in the computation domain. A residual constructed in this manner can be thought of as an estimate of the summation of rate of change of vorticity scaled with a characterize vorticity.

Please notice that eq.(2.84) is not a stringent residual. The most common way to construct a residual is to evaluate the deviation of the solution from the system of equation resulting from the discretization of the governing equation

$$Res = L(\gamma) \ , \tag{2.85}$$

where L is the discretized operator of the governing equation.

2.4 Variants of the vorticity-streamfunction formulation

Even though the $\gamma - \psi$ formulation and the $\gamma - \vec{U}$ formulation is rarely used, the method has been utilized in a variety of flow situations in the past. Some of the methods will be reviewed in the following sections together with a single result showing the implementation of a method dealing directly with the problem concerning boundary values for ψ in a multiply connected region.

2.4.1 3-Dimensional forms of the vorticity formulation

The extension from two to three space dimensions for the $\gamma - \psi$ formulation is in some way straight forward, (see f.i. [12]). By defining a streamfunction $\vec{\phi}$ as a vector with two component different from zero, $\vec{\phi} = (0, \psi, \theta)$, and with the velocity component given by

$$U = \frac{\partial \psi}{\partial y} \ , \ V = -\frac{\partial \psi}{\partial x} - \frac{\partial \theta}{\partial z} \ , \ W = \frac{\partial \theta}{\partial y} \ , \tag{2.86}$$

$\vec{\phi}$ will automatically ensure that mass conservation is satisfied. The definition of vorticity for γ_z and γ_x are rewritten in terms of $\vec{\phi}$

$$\gamma_z = -\frac{\partial^2 \psi}{\partial x^2} - \frac{\partial^2 \psi}{\partial y^2} - \frac{\partial^2 \theta}{\partial x \partial z} \tag{2.87}$$

$$\gamma_x = \frac{\partial^2\theta}{\partial y^2} + \frac{\partial^2\theta}{\partial z^2} + \frac{\partial^2\psi}{\partial x \partial z} \ . \tag{2.88}$$

The transport equation for vorticity maintain nearly the same form but the scalar γ in 2-dimensions is in 3-dimensions a vector. Solving for γ_x and γ_z by integrating the transport equations, γ_y can be found by the solenoidal requirement of vorticity

$$\nabla \cdot \vec{\gamma} = 0 \ . \tag{2.89}$$

An alternative to the vorticity streamfunction formulation can be derived by eliminating ψ by the velocity and form a set of Poisson equations for the velocity [53]

$$\nabla^2 \vec{U} = -\nabla \times \vec{\gamma} \ , \tag{2.90}$$

by the use of the continuity equation and the definition of vorticity [21]. This method can of course be used in a 2-dimensional space [48]

2.4.2 2-Dimensional variants of the vorticity streamfunction formulation

The 2-dimensional form are by far the most common one. It has been used in conjunction with a lot of different flows. Typically the different approaches varies in the formulation of the boundary condition, especially for the vorticity. A method where the setup of boundary conditions for the streamfunction strongly based on a potential method to determining the volume flow through any line connecting boundaries of the flow domain has been implemented by the author of this dissertation. The idea is to determine the net flow through an inviscid solution and presume this overall inviscid volume flow equals the overall viscous volume flow. Assume the velocity field as a superimposing of an inviscid and viscous flow [46] [57]

$$\vec{U} = \vec{U}_{viscous} + \vec{U}_{inviscid} \ , \tag{2.91}$$

with

$$\vec{U}_{viscous} = \left(-\frac{\partial\psi}{\partial y}, \frac{\partial\psi}{\partial x} \right) \tag{2.92}$$

$$\vec{U}_{inviscid} = \left(\frac{\partial\phi}{\partial x}, \frac{\partial\phi}{\partial y} \right) \ . \tag{2.93}$$

Applying the definition of vorticity and the continuity equation, the velocity relations are transformed to a Poisson equation

$$\nabla^2\psi + \nabla^2\phi = \gamma \ . \tag{2.94}$$

This problem can be decoupled into two systems of equations

$$\nabla^2\psi = \gamma \quad \nabla^2\phi = 0 \ , \tag{2.95}$$

where the last equation defines the classical potential flow problem. The formulation, eq.(2.95), looks quite similar to the methods outlined in chapter 2 section (2.2) where the Base-function was introduced, but the difference is quite clear when the utilized boundary conditions are outlined. As the net flow is determined totally by the potential flow the difference $\Delta\psi$ f.i. between the inflow boundary and the airfoil equals zero and the viscous velocity fields only redistribute the inviscid volume flow. By this the viscous no-slip condition must be reformulated to a slip condition with a tangential velocity equal the inviscid velocity with opposite sign. This was by the author considered as the biggest problem with the method as indicated on Fig.(2.5), where a U-velocity profile at mid-chord of a NACA 0012 airfoil is shown calculated with the streamfunction-potential method and the Base-function method.

On this figure it is clearly shown that even though the flow in the outer part of the boundary layer are predicted similar with the two methods, discrepancies occur close to the wall, where the summation of the viscid and inviscid velocity does not mimic the no-slip condition. Investigations indicate that the space accuracy are very important when calculating the slip-velocity. One of the anterior parts of the method is the general applicable to flows with more than one solid body e.g. an airfoil with flaps. As the volume flow is determined by the inviscid solution the boundary conditions for ψ is on every boundary zero streamfunction. It is the authors opinion that the method is worth further investigations especially in a lifting case.

A compressible form of the vorticity streamfunction formulation has been utilized in [20]. In this case the continuity and the definition of the streamfunction yields the following Poisson equation

$$\frac{\partial}{\partial x}\left(\frac{1}{\rho}\frac{\partial\psi}{\partial x}\right) + \frac{\partial}{\partial y}\left(\frac{1}{\rho}\frac{\partial\psi}{\partial y}\right) = \gamma \ , \tag{2.96}$$

where ρ is the density. The convective terms in the transport equation for vorticity contains now the mass flow vector instead of the velocity vector. One

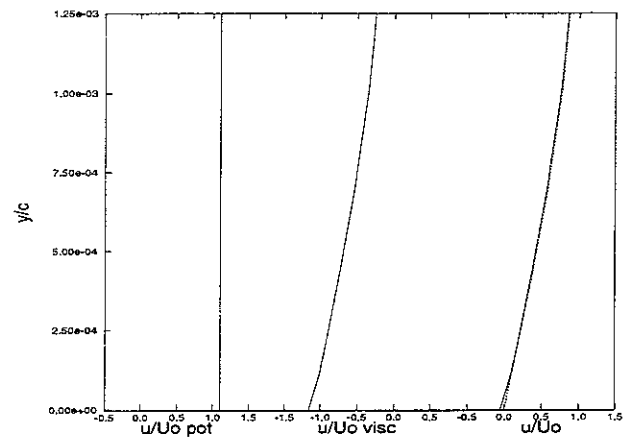

Figure 2.5: *Velocity profiles obtained at mid-chord of a NACA 0012 airfoil with the streamfunction-potential method and the Base-function method.* $Re = 200$. $\alpha = 0°$. u/U_0 *pot is the potential flow solution and* u/U_0 *visc is the viscous part.* u/U_0 *is the resulting velocity profiles from the superimposing method and the conventional stream function vorticity method (dotted line).*

auxiliary relation is of course needed when the density of the fluid has been introduced. Normally the last equation is the energy equation or assuming constant total enthalpy.

By applying the Base-function outlined in chapter 2 section (2.2) we do not explicitly impose the no-slip condition. In [49] a influence matrix techniques has been used which satisfy both the no-slip condition and the viscous Kutta condition. The method also utilize a superimposing principle as the Base-function method but introduce extra vorticity in the hole calculation domain and introduce as many elementary functions as grid points located at the solid wall.

2.5 Aerodynamic forces and boundary layer parameters

To calculate the aerodynamic forces, the pressure and skin friction are integrated along the surface. The pressure is obtained from

$$P(s) = P(s_0) + \int_{s_o}^{s} \left[\frac{\Omega_{rot}^2}{2} \frac{\partial}{\partial s}[(x-x_o)^2 + y^2] + \dot{\Omega}_{rot}[(x-x_o)y_s - yx_s] \right] ds - \frac{1}{Re} \int_{s_o}^{s} \frac{\partial}{\partial n} (\epsilon\gamma)\, ds \,. \tag{2.97}$$

where $P(s_0)$ is the pressure at the front stagnation point of the airfoil. Here and in the rest of this section γ wil denote the vorticity corrected by the Base-function. The vorticity is known at the center of the cell faces so the integration performed numerically by

$$P_i = P_{i-1} + G(i+1/2) \cdot \Delta s \ , \tag{2.98}$$

where $G(i+1/2)$ is the kernel of the integrations in eq.(2.97), is second order in space. Local quantities for pressure and a viscous surface friction are often refer to as pressure coefficient C_p and skin friction coefficient C_f

$$C_p = \frac{P' - P_0'}{\frac{1}{2}\rho U_0^2} \ , \ C_f = \frac{\tau_A}{\frac{1}{2}\rho U_0^2} = -\frac{2}{Re}\gamma_A \ , \tag{2.99}$$

where superscript $'$ on P denotes a pressure which is not non-dimensionalized and τ_A is the wall shear stress. Assuming inviscid flow along the front stagnation line the pressure coefficient at the stagnation line is accordingly to the Bernoulli equation equal to 1. By this assumption a level of C_p is established and eq.(2.97) can be used to provide C_p at the remaining part of the airfoil, with

$$C_p = 1 + 2 \cdot P \ , \tag{2.100}$$

where P is determined from eq.(2.97). Also the following non-dimensionalized global numbers, denoted coefficient of lift, drag and moment, are normally considered

$$C_l = \frac{F_l}{0.5 \cdot \rho U_0 l} \ , \ C_d = \frac{F_d}{0.5 \cdot \rho U_0 l} \ , \ C_m = \frac{M}{0.5 \cdot \rho U_0 l^2} \ , \tag{2.101}$$

where l is the span length, F_l is the total force normal to the free stream velocity, F_d is the total force tangential to the free stream velocity and M is the moment around a point (x_0, y_0). These coefficients can be grouped with respect to pressure and friction

$$C_{lp} = -\frac{2}{l}\oint P(s)\frac{\partial x}{\partial s}ds \ , \ C_{lf} = -\frac{2}{Rel}\oint \gamma(s)\frac{\partial y}{\partial s}ds \quad (2.102)$$

$$C_{dp} = \frac{2}{l}\oint P(s)\frac{\partial y}{\partial s}ds \ , \ C_{df} = -\frac{2}{Rel}\oint \gamma(s)\frac{\partial x}{\partial s}ds \quad (2.103)$$

$$C_{mp} = \frac{2}{l}\oint P(s)\left((x-x_0)\frac{\partial x}{\partial s} + (y-y_0)\frac{\partial y}{\partial s}\right) ds \quad (2.104)$$

$$C_{mf} = \frac{2}{Rel}\oint \gamma(s)\left(-(y-y_0)\frac{\partial x}{\partial s} + (x-x_0)\frac{\partial y}{\partial s}\right) ds \quad (2.105)$$

where subscript p and f, respectively, represent contributions due to pressure and viscous forces and where the moment is considered positive in the clockwise direction. When considering oscillating airfoils it is common to use only forces due pressure and define the normal coefficient, C_n, as the integration of pressure projected on the chord direction of the airfoil and the tangential coefficient, C_t as the summation of pressure projected on a direction tangential to the airfoil chord.

Considering boundary layer parameters these are defined for flow past a flat plate

$$\delta = d \ where \ \frac{U}{U_0} = 0.99 \quad (2.106)$$

$$\delta^* = \int_o^\infty \left(1 - \frac{U}{U_0}\right) \partial y \quad (2.107)$$

$$\theta = \int_o^\infty \frac{U}{U_0}\cdot\left(1 - \frac{U}{U_0}\right) \partial y \quad (2.108)$$

where d is the normal distance from the wall and δ is the boundary layer thickness. δ^* is the displacement thickness and θ is the momentum thickness. In airfoil flows or other flow situations with curved surfaces these definitions are no longer valid due to the upper limit in the integration [54]. The author has used a method dealing with the magnitude of vorticity in order to determine the extension of the boundary layer. In a flow past a solid body with a ir-rotational on-coming flow vorticity is only present in the viscous part. The extension of the viscous part is defined as the boundary layer thickness

δ and is used as upper limit in eq.(2.107) and (2.108). δ is found where the magnitude of vorticity, measured in a path advancing the boundary layer from the top, becomes greater than

$$\gamma_\delta = \frac{\max|\gamma_i|}{\mathrm{Re}} \ , \tag{2.109}$$

where $\max|\gamma_i|$ is the maximum vorticity at the considered boundary layer station, $\xi = i$. This choice is some how arbitrary, but serves as filtering mechanism for numerical errors such as spreading and generation of vorticity outside the boundary layer. The velocity used in eq.(2.108) and (2.107) are the velocity vector $\vec{U}$ projectet on the tangential direction $\vec{s}$ of the surface.

Chapter 3

Turbulence modeling

The present chapter describes the various turbulence models utilized in this dissertation. The used turbulence model are the algebraic turbulence model by Baldwin & Lomax (BB) [4], the 1-equation models by Baldwin & Barth (BL) [3] and Spalart & Allmaras (SA) [52] and the 2-equation $K-\omega$ (KO) [34] model by Menter. In order to be able to compare the nature of the utilized turbulence models a short review of turbulence models for aerodynamic flows will be presented first.

3.1 Short review of turbulence modeling

In the preceding chapter 2 the time averaging process was addressed and the concept of an eddy-viscosity was introduced. When the time variations in the mean flow are small, the time averaging process is straight forward and the mean velocity the U_i component is calculated by

$$U_i = \frac{1}{\Delta t} \int_{t_0-\Delta t/2}^{t_0+\Delta t/2} \tilde{u} dt \ . \tag{3.1}$$

If the time variations in the mean flow are large a condition on the time averaging period [26] can be derived

$$\frac{\left(\int_{t_0-\Delta t/2}^{t_0+\Delta t/2} \tilde{u}_i dt - \int_{t_0+\Delta t/2}^{t_0+3\Delta t/2} \tilde{u}_i dt \right)}{\int_{t_0}^{t_0+\Delta t} \tilde{u}_i dt} = \frac{U(t_0+\Delta t) - U(t_0)}{U(t_0+\Delta t/2)} << 1 \tag{3.2}$$

If the above condition can not be satisfied a sample averaging can be utilized

$$U_i = \frac{1}{n} \sum_{i=1}^{i=1,n} \tilde{u} \ , \tag{3.3}$$

where n is the number of repeat experiments. In computational fluid dynamic the length of the time averaging process, (Δt), is some how arbitrary. When the time averaging process has been carried out on the momentum equations no sign is left of it. This means on the other hand, that when integrating in time the time averaged momentum equations a mean velocity will always be the outcome and the variation of this mean velocity should always be compared with the global time step utilized in the integration process. A way to avoid the time averaging process can be the Large Eddy Simulation, LES, although the basic of the method has been established by another view point.

The LES approach is based on a space-averaging instead of a time-averaging and the time dependent details of the large eddies are calculated by use of a simple subgrid-scale model. The large eddies are those motion elements which carry most of the kinetic energy and most of the turbulent fluxes and the motion is simulated by a time dependent numerical integration scheme which numerical resolves scales in between a lower limit of order h given by the grid scale and a upper limit given by the extension of the computational domain. The details of these large eddies are related to the dissipation of turbulent kinetic energy where the time scale is the Kolmogorov time scale which typically is several orders of magnitude lower than the integration time used in Navier-Stokes calculations. Even though the basis of the turbulence modeling is totally different in LES and time averaging methods the Navier-Stokes equations has the same appearance, but the eddy-viscosity used in a LES methods is related to the volume of the grid cells.

The eddy-viscosity concept goes back to 1877 by the work of Boussinesq who was the first to introduce

$$\tau_{ij} = -\overline{u_i u_j} = \nu_t \frac{\partial U_i}{\partial x_j} \ . \tag{3.4}$$

Later Prandtl in 1925 related the eddy-viscosity to a length scale, l, of the turbulent motion and derivatives of the mean velocity by

$$\nu_t = l^2 \frac{\partial U_i}{\partial x_j} \ . \tag{3.5}$$

von Karman postulated a linear relation ship, scaled by the von Karman constant κ, between the length scale l and the distance, y, from a solid wall in an attached boundary layer

$$\frac{l}{\delta} = \kappa \frac{y}{\delta} \quad \kappa = 0.41 \ , \tag{3.6}$$

for $y/\delta < 0.2$ where δ is the boundary layer thickness. For $y/\delta > 0.2$ l was assumed constant. van Driest found by measurement that in the laminar sublayer the variation of l was not linear but $l \sim y^2$ so

$$l = \kappa y \left[1 - exp\left(-y^+/A^+\right)\right] = \kappa y D \ , \tag{3.7}$$

where D is the famous van Driest damping function. Similar Klebanoff found by experiments that in the outer part of the boundary layer the length scale l should go to zero which was introduced by the Klebanoff intermittency function F_{Kleb}

$$F_{Kleb} = \left[1 + 5.5\left(\frac{y}{\delta}\right)^6\right]^{-1} \ . \tag{3.8}$$

The work of Prandtl, von Karman, van Driest and Klebanoff is still the basis of many eddy-viscosities models and the relations still serves as calibration tools for new turbulence models based on the eddy-viscosity hypothesis.

The combination of eq.(3.6)-(3.8) is often utilized as a complete turbulence model and the proberly most famous model based on these equations are the Cebeci-Smith model [8]. It is believed that one of the major short comings for such a turbulence model is that no transport of a turbulent quantity is present except for the one inherent in the Navier-Stokes equations.

Most of the work in the concept of eddy-viscosity when concerning transport processes for a turbulent quantity is based on the transport equations for the turbulent kinetic energy K, dissipation of turbulent kinetic energy ϵ and the specific dissipation rate ω [43], [33], [36]. In a very general form the transport equation for K is

$$\frac{\partial K}{\partial t} + U_j \frac{\partial K}{\partial x_j} = \tau_{ij} \frac{\partial U_i}{\partial x_j} - \epsilon + \frac{\partial}{\partial x_j}\left[\left(\nu + \sigma \nu_t/\sigma_k\right) \frac{\partial K}{\partial x_j}\right] \ , \tag{3.9}$$

where τ_{ij} is the Reynolds stress tensor, σ, σ_k is closure coefficients and ϵ is the dissipation of turbulent kinetic energy for which a transport equations can be established

$$\frac{\partial \epsilon}{\partial t} + U_j \frac{\partial \epsilon}{\partial x_j} = C_{\epsilon 1} \frac{\epsilon}{K} \tau_{ij} \frac{\partial U_i}{\partial x_j} - C_{\epsilon 2} \frac{\epsilon^2}{K} + \frac{\partial}{\partial x_j}\left[\left(\nu + \sigma \nu_t/\sigma_\epsilon\right) \frac{\partial \epsilon}{\partial x_j}\right] \ . \tag{3.10}$$

A general form of the transport equation for the specific dissipation rate ω is

$$\frac{\partial \omega}{\partial t} + u_j \frac{\partial \omega}{\partial x_j} = \alpha \frac{\omega}{K} \tau_{ij} \frac{\partial u_i}{\partial x_j} - \beta \omega^2 + \frac{\partial}{\partial x_j} \left[(\nu + \sigma \nu_t) \frac{\partial \omega}{\partial x_j} \right] \quad , \tag{3.11}$$

which is basicly the same equation as Kolmogorov postulated in 1942 with an additional production term.

In the model of U. C. Goldberg [17] the $K - \epsilon$ equation are utilized to establish an algebraic relation ship within a separation bubble for the eddy-viscosity. Outside the separation bubble typically a Cebeci-Smith or a Baldwin-Lomax algebraic turbulence model is applied.

In the half-equation model by Johnson & King model [24], a transport equation for the development in the flow direction of the maximum Reynolds stress, is made up from the transport equation for turbulent kinetic energy, K. The term half-equation model is due to the ordinary differential equation derived.

1-equation models has been and still is a very popular choice. Historically 1-equation models was based on the transport equation for K and the prescription of a length scale such that the eddy-viscosity is

$$\nu_t = l\sqrt{K} \quad , \tag{3.12}$$

where l is prescribed by an algebraic relation. Other mostly used 1-equation models are the Spalart-Allmaras and the Baldwin-Barth model. Where the Spalart-Allmaras model is derived from empiricism and dimensional analysis the Baldwin-Barth model is derived from combination of the $K - \epsilon$ model. The Baldwin-Barth models is, as derived from the $K - \epsilon$ model, basicly a 2-equation model where some terms has been removed in order to have a 1-equation model. The 2-equation Baldwin-Barth model was modified by U. C. Goldberg [18] to become pointwise, so the distance to the nearest wall did not appear in the turbulence model.

Typically 2-equation models are grouped into $K - \epsilon$ and $K - \omega$ models where the eddy-viscosity is

$$\nu_t = C_\mu \frac{K^2}{\epsilon} \quad , \quad \nu_t = \frac{K}{\omega} \quad . \tag{3.13}$$

The variety of the models are very large [61] where the biggest variation are found in the utilized damping functions. Menter has combined the free

stream independence of the $K-\epsilon$ model with the accuracy of the $K-\omega$ model in the near wall region.

Beyond the Boussinesq approximation is the second moment closure [62]. These method can be grouped in two where the first approach is to solve an differential equation for the Reynolds stresses and the other is the algebraic Reynolds stress models. By solving for the Reynolds stresses normally third order moment are introduced which must be modeled in some way.

Considering aerodynamic flows transition plays a major role in the computation of maximum lift. Even though some turbulence models persist a transition model it should never be trusted [52]. Later in this chapter the transition problem will be addressed.

3.2 The Baldwin-Lomax turbulence model

The Baldwin-Lomax turbulence model is pattern after the Cebeci-Smith model [8] and is by far the mostly used algebraic turbulence model. It follows the ideas of Prandtl, von Karman, van Driest and Klebanoff and introduce a two layer division of the boundary layer named as the inner and outer part where the eddy-viscosity non-dimensionalized by ν is given by

$$(\nu_t^*) = \begin{cases} (\nu_t^*)_{inner} & \text{for } y \leq y_{crossover} \\ (\nu_t^*)_{outer} & \text{for } y > y_{crossover} \end{cases} , \tag{3.14}$$

where y is the normal distance from the wall and $y_{crossover}$ is the smallest value of y at which values from the inner and outer formulas are identical.

In the inner region the Prandtl-Van Driest formulation is used

$$(\nu_t^*)_{inner} = Re \cdot l^2 \left|\gamma\right| \quad , \tag{3.15}$$

where

$$l = \kappa y \left[1 - e^{-y^+/A^+}\right] \quad , \quad y^+ = \sqrt{Re \left|\gamma_{max}\right|} \cdot y \quad , \tag{3.16}$$

where γ_{max} is the maximum vorticity in the profile, $A^+ = 26$ is the van Driest damping constant and $\kappa = 0.4$ is von Karman's constant. For the outer layer the following relations are proposed

$$(\nu_t^*)_{outer} = Re \cdot K_{Claus} \cdot C_{CP} F_{Kleb} F_{Wake} \quad , \tag{3.17}$$

where

$$F_{Wake} = min\left(y_{\max} F_{\max}; C_{WK} y_{\max} U_{Diff}^2 / F_{\max}\right) \tag{3.18}$$

Here $C_{CP} = 1.6$, $C_{WK} = 0.25$ and the Clauser constant $K_{Claus} = 0.0168$. The quantities $F_{\max}$ and $y_{\max}$ are determined from the function

$$F = y\,|\gamma|\left[1 - e^{-y^+/A^+}\right]. \tag{3.19}$$

In wakes, the exponential term is set to zero. $F_{\max}$ is the maximum value of F occurring in the velocity profile and y_{max} is the value of y where this occurs.

The quantity U_{Diff} is the difference between the minimum and maximum total velocity in the profile

$$U_{Diff} = (\sqrt{U^2 + V^2})_{\max} - (\sqrt{U^2 + V^2})_{\min}, \tag{3.20}$$

where $(\sqrt{U^2 + V^2})_{\min}$ is taken to be zero except in wakes. In wakes the position of the wake is said to be at the position of $(\sqrt{U^2 + V^2})_{\min}$. The function F_{Kleb} is the Klebanoff intermittency factor given by

$$F_{Kleb} = \left[1 + 5.5\left(C_{Kleb} \cdot y/y_{\max}\right)^6\right]^{-1}, \tag{3.21}$$

with $C_{Kleb} = 0.3$.

The Baldwin-Lomax model is difficult applicable in the wake flow behind an airfoil. Examining the streamvice change in eddy-viscosity close to the trailing edge of an airfoil when the models is applied in the basic formulation a large and rapid change is found. To smooth these large variations, an intermittency function is used in the near wake region and is given by, [19]

$$\nu_t(s) = \nu_{t,BL}(s) + [\nu_{t,BL}(s_{te}) - \nu_{t,BL}(s)]\, exp\left(-\frac{s - s_{te}}{\mathcal{B}}\right), \tag{3.22}$$

where s is the distance along constant ξ lines and $\mathcal{B} = 8.0 \cdot Re^{-0.2}$ is a length scale corresponding to at least 20 times the boundary layer thickness for a flat plate. In order to decrease the large variations in the eddy-viscosity close to the trailing edge C_{wk} is taken to be $C_{wk} = 1$ instead of 0.25 [19] in the wake. Further more an under relaxation of the eddy-viscosity is used in the wake in order to stabilize the flow.

3.3 The Baldwin-Barth turbulence model

The Baldwin-Barth turbulence model was one of the first 1-equation turbulence models where no out coming information was needed for a length scale. The model is derived from the $K-\epsilon$ turbulence model by considering an equation for

$$\frac{DR_t}{Dt} = \frac{2R_t}{K}\frac{DK}{Dt} - \frac{R_t}{\epsilon}\frac{D\epsilon}{Dt} \quad , \tag{3.23}$$

where

$$R_t = \frac{K^2}{\nu\epsilon} \quad , \tag{3.24}$$

is the turbulent Reynolds number. As the model is derived from the $K-\epsilon$ model steep gradient close to the wall will be transmitted to the model. Different function is defined in order to make the variation of R_t linear in the near wall region. The transport equation for R_t is

$$\frac{D(R_t)}{Dt} = (C_{\epsilon_2}f_2 - C_{\epsilon_1})\sqrt{R_tP} + \frac{1}{Re}\left(1+2\frac{\nu_t^*}{\sigma_e}\right)\frac{\partial^2 R_t}{\partial x_i \partial x_i} \tag{3.25}$$

$$- \frac{1}{Re\sigma_e}\frac{\partial}{\partial x_i}\left(\nu_t^*\frac{\partial R_t}{\partial x_i}\right) \quad , \tag{3.26}$$

and

$$\nu_t^* = C_\mu R_t D_1 D_2 \quad . \tag{3.27}$$

P is the production term, $C_{\epsilon 1}$, $C_{\epsilon 2}$, C_μ and σ_e are closure constants and f_2 is a damping function. All variables are put in non-dimensional form by use of the free stream velocity U_0 and the chord length of the airfoil c. The utilized closure constants are given in table (3.1).The functions D_1 and D_2 are van Driest damping functions given as

$$\begin{aligned} D_1 &= 1 - exp(-y^+/A_1^+) \\ D_2 &= 1 - exp(-y^+/A_2^+). \end{aligned} \tag{3.28}$$

P is a production term given as

$$P = \nu_t^*\left(\frac{\partial U_i}{\partial x_j} + \frac{\partial U_j}{\partial x_i}\right)\frac{\partial U_i}{\partial x_j} \quad . \tag{3.29}$$

The function f_2 is given by

$$\begin{aligned} f_2(y^+) = & \quad \frac{C_{\epsilon 1}}{C_{\epsilon 2}} + \left(1 - \frac{C_{\epsilon 1}}{C_{\epsilon 2}}\right)\left(\frac{1}{\kappa y^+} + D_1 D_2\right) \\ & \cdot \left(\sqrt{D_1 D_2} + \frac{y^+}{\sqrt{D_1 D_2}}\left[\frac{D_2(1-D_1)}{A^+} + \frac{D_1(1-D_2)}{A_2^+}\right]\right) \quad . \end{aligned} \tag{3.30}$$

κ	$C_{\epsilon 1}$	$C_{\epsilon 2}$	C_μ	A_1^+	A_2^+
0.41	1.2	2.0	0.09	26	10

Table 3.1: *Utilized closure constant for the Baldwin-Barth turbulence model.*

The turbulence model, eq.(3.26), has been discretized by the same procedure as the transport equation for vorticity with a first order accurate upwind scheme for the convective terms and the production term treated explicitly as a source term. The algebraic equations are solved by the same ADI routine as the used for the transport equation for vorticity.

The model has some numerical stability problems, (as also pointed out by Baldwin and Barth). When discretizing the transport equation, eq.(3.26), it is not automatically satisfied that our finite difference approximation of the terms

$$\frac{1}{Re}\left(1+2\frac{\nu_t^*}{\sigma_e}\right)\frac{\partial^2 R_t}{\partial x_i \partial x_i} - \frac{1}{Re\sigma_e}\frac{\partial}{\partial x_i}\left(\nu_t^*\frac{\partial R_t}{\partial x_i}\right) \quad , \tag{3.31}$$

guarantees a diagonal matrix with negative diagonal entries and positive off-diagonal entries. This is only satisfied when ν_t^* varies by only a factor of 3 from one mesh point to another. It is found that this problem do occur with some grid stretching. The problem is rectified by limiting the anti-diffusion term, (the second term in eq.(3.31)), to 20% of the value predicted by the model. The regions where this limiting process has to be applied is typically at cells close to the airfoil and at the top of the boundary layer. The limiting process normally involves 2 or 3 cells normal to the streamvice direction.

In a later, very rarely used, version of the BB model [5] modification was introduced to stabilize numerical the model. It is the authors impression that the numerical benefits of using the latter version on behalf of a less physical model was small compared to the original version outlined above.

The utilized boundary conditions follows the recommendations of Baldwin and Barth. At inflow boundaries the turbulence intensity is assumed to be small and therefore also the eddy-viscosity. By this, the boundary condition for R_t is put equal to 1 which results in an eddy-viscosity lower than 0.09 times the molecular viscosity. At outflow a Neumann condition is

applied for R_t

$$\frac{dR_t}{d\xi} = 0 \ . \tag{3.32}$$

At the surface we require R_t=0. As the variable is located in the center of the cells a value different from zero must be specified. The model was designed to behave linearly in the near wall region with

$$R_t = \frac{\kappa}{C_\mu} y^+ \ , \tag{3.33}$$

so this functional relationship was utilized together with a smoothing function

$$R_{t,i} = \frac{1}{4} \cdot (R_{t,i-1} + 2 \cdot R_{t,i} + R_{t,i+1}) \quad i \in [nk, nx - nk] \ , \tag{3.34}$$

in order to prevent wiggles from forming.

3.4 The Spalart-Allmaras turbulence model.

The Spalart-Allmaras turbulence is an 1-equation turbulence model similar to the BB model. This model also utilize a transport equation for a turbulent quantity but contrary the BB models it contains a destruction term depending implicit of the pressure gradient. The derivation of the SA model is different from the derivation of the BB model and is partly based on dimensional analysis and empiricism. The SA transport equation for the working variable $\mathcal{V}$ strongly related to the eddy-viscosity is

$$\begin{aligned} \frac{D\mathcal{V}}{Dt} = C_{b1}\mathcal{S}\mathcal{V} \ &+ \ \frac{1}{\sigma}\left[\frac{\partial}{\partial x_k}\left((\nu + \mathcal{V})\frac{\partial \mathcal{V}}{\partial x_k}\right) + C_{b2}\left(\frac{\partial \mathcal{V}}{\partial x_k}\frac{\partial \mathcal{V}}{\partial x_k}\right)\right] \\ &- \ C_{w1} f_w \left[\frac{y}{\mathcal{V}}\right]^2 , \end{aligned} \tag{3.35}$$

where $\mathcal{S}$ is a modified vorticity, σ, C_{b2}, C_{w1} are closure constant and f_w is a damping function. All variables are put in non-dimensional form by use of the free stream velocity U_0 and the chord length of the airfoil c. By applying some mathematical transformation the final transport equation in x, y-space for $\mathcal{V}^* = \mathcal{V}/\nu$ is

$$\frac{D\mathcal{V}^*}{Dt} = C_{b1}\mathcal{S}\mathcal{V}^*\left[\frac{C}{U_0}\right] - \frac{1}{Re}C_{w1}f_w\left(\frac{\mathcal{V}^*}{y}\right)^2 \ + \ \frac{1 + C_{b2}}{\sigma Re}\left[\frac{\partial}{\partial x_k}\left(\mathcal{V}^*\frac{\partial \mathcal{V}^*}{\partial x_k}\right)\right]$$

$$+ \frac{1 - C_{b2}\mathcal{V}^*}{\sigma Re} \frac{\partial^2 \mathcal{V}^*}{\partial x_k \partial x_k} \tag{3.36}$$

with the eddy-viscosity, (non-dimensionalized by the kinematic viscosity),

$$\nu_t^* = \mathcal{V}^* f_{v1}, \quad \mathcal{V}^* = \mathcal{V}/\nu, \quad f_{v1} = \frac{\mathcal{V}^{*3}}{\mathcal{V}^{*3} + C_{v1}^3}, \tag{3.37}$$

and

$$\mathcal{S}\left[\frac{c}{U}\right] = \mid \gamma \mid + \frac{\mathcal{V}^*}{\kappa^2 y^2 Re} f_{v2} \tag{3.38}$$

The Spalart-Allmaras model utilize the following closure constants given in table (3.4) and auxiliary relations

$$f_{v2} = 1 - \frac{\mathcal{V}^*}{1 + \mathcal{V}^* f_{v1}}, \quad f_w = g\left[\frac{1 + c_{w3}^6}{g^6 + c_{w3}^6}\right]^{1/6}, \tag{3.39}$$

and

$$g = r + C_{w2}(r^6 - r), \quad r = \frac{\mathcal{V}^*}{\mathcal{S}\kappa^2 y^2} = \frac{\mathcal{V}^*}{\mid \gamma \mid \kappa^2 y^2 Re + \mathcal{V}^* f_{v2}}. \tag{3.40}$$

C_{b1}	C_{b2}	C_{v1}	σ	C_{w1}	C_{w2}	C_{w3}	κ
0.1355	0.622	7.1	2/3	$\frac{C_{b1}}{\kappa^2} + \frac{1+C_{b2}}{\sigma}$	0.3	2	0.41

Table 3.2: Utilized constants for the Spalart-Allmaras turbulence model

The Spalart-Allmaras turbulence model is discretized and solved in the same manner as the Baldwin-Barth turbulence model and with the same outflow boundary condition. At inflow Spalart-Allmaras recommend a value close to zero and zero if the solving procedure does not produce negative eddy viscosities. In the present implementation $\mathcal{V}^* = 1 \cdot 10^{-10}$ was utilized. Similar to the Baldwin-Barth model, this model also require specification of the value in the cell next to the airfoil. This is done by following the model approach

$$\mathcal{V}^* = \kappa y^+, \tag{3.41}$$

and applying the smoothing algortithm eq.(3.34) $\mathcal{V}^*$ for as utilized for the BB model. The production term was treated implicitly toghether with the destruction term in order to further stabilize the numerical integration and enhance the time step.

The argument r introduced in the f_w function acting on the destruction term is numerically very unstable in the present implementation. The function f_{v2} is designet to make $\mathcal{S}$ equal to $1/\kappa y^+$ all the way to the wall and not only in a log layer. If small wiggles is introduced some how in r the wiggles will be transmitted to the destruction term. As the destruction term plays a dominant role it will have a large impact on the solution and next time the r argument is calculated an amplification of the wiggles will occur. It was found that the best way to avoid wiggles from forming was a combination of a small time step and a smoothing of r along a boundary layer station by

$$r_j = \frac{1}{4} \cdot (r_{j-1} + 2 \cdot r_j + r_{j+1}) \quad j \in [2, ny-1] \ . \tag{3.42}$$

3.5 The K-ω / K-ϵ turbulence model

In this section the $K-\omega$ turbulence model by Menter will be described. First the baseline model (BSL) will be described and secondly the shear stress transport (SST) model. The model consist of transport equations for the turbulent kinetic energy K and the dissipation time scale ω. The Menter model is blending the $K-\omega$ model of Wilcox [60], [61] with a standard $K-\epsilon$ model. By doing so the free stream independence of the $K-\epsilon$ model are combined with the near-wall accuracy of the $K-\omega$ model.

3.5.1 The K-ω-BSL turbulence model

The governing transport equation for K is

$$\frac{DK}{Dt} = \tau_{ij}\frac{\partial U_i}{\partial x_j} + \frac{1}{Re}\frac{\partial}{\partial x_j}\left[(1+\sigma_k\nu_t^*)\frac{\partial K}{\partial x_j}\right] - \beta'\omega K \ , \tag{3.43}$$

where σ_k and β' are closure constants. The transport equation for ω is

$$\frac{D\omega}{Dt} = \frac{\Gamma\tau_{ij}}{\nu_t^*}\frac{\partial U_i}{\partial x_j} + \frac{1}{Re}\frac{\partial}{\partial x_j}\left[(1+\sigma_\omega\nu_t^*)\frac{\partial \omega}{\partial x_j}\right] - \beta\omega^2 + \frac{2\sigma_\omega}{\omega}(1-F_1)\frac{\partial K}{\partial x_j}\frac{\partial \omega}{\partial x_j} \ , \tag{3.44}$$

where σ_ω, Γ and β is closure constants. ω has been non-dimensionalized by U_0/c, K by U_0^2, U by U_0 and x_j by the chord length c. F_1 is the blending function which make the formulation equal to the $K-\omega$ in the inner part of the boundary layer and equal to the $K-\epsilon$ model in the outer part of the boundary layer. F_1 equals 1 at the wall and gradually goes to zero in the middle of the boundary layer. The eddy-viscosity is given by

$$\nu_t^* = \frac{K}{\omega} Re \ . \tag{3.45}$$

The closure constant utilized in the $K-\omega$-BSL models are listed in table (3.3) where the blending of the different constants are defined by

$$\phi = F_1\phi_1 + (1-F_1)\phi_2 \ . \tag{3.46}$$

ϕ	σ_k	σ_ω	β	β'	κ	Γ
set 1	0.5	0.5	0.0750	0.09	0.41	$\beta/\beta' - \sigma\kappa^2/\sqrt{\beta'}$
set 2	1.0	0.856	0.0828	0.09	0.41	$\beta/\beta' - \sigma\kappa^2/\sqrt{\beta'}$

Table 3.3: *Utilized closure constants in the $K-\omega$ turbulence model.*

The production term for K, P_k, is

$$\tau_{ij}\frac{\partial U_i}{\partial x_j} = \left[\frac{\nu_t^*}{Re}\left(\frac{\partial U_i}{\partial x_j} + \frac{\partial U_j}{\partial x_i}\right) - \frac{2}{3}\delta_{ij}K\right]\frac{\partial U_i}{\partial x_j} \ , \tag{3.47}$$

which by use of the continuity equation for incompressibe flow reduces to

$$\tau_{ij}\frac{\partial U_i}{\partial x_j} = \frac{\nu_t^*}{Re}\left[2\left(\frac{\partial U}{\partial x}\right)^2 + 2\left(\frac{\partial V}{\partial y}\right)^2 + \left(\frac{\partial U}{\partial y}\right)^2 + \left(\frac{\partial V}{\partial x}\right)^2 + 2\frac{\partial U}{\partial y}\frac{\partial V}{\partial x}\right] . \tag{3.48}$$

Similar the production term for ω, P_ω, is

$$\frac{\tau_{ij}}{\nu_t^*}\frac{\partial U_i}{\partial x_j} = \left[2\left(\frac{\partial U}{\partial x}\right)^2 + 2\left(\frac{\partial V}{\partial y}\right)^2 + \left(\frac{\partial U}{\partial y}\right)^2 + \left(\frac{\partial V}{\partial x}\right)^2 + 2\frac{\partial U}{\partial y}\frac{\partial V}{\partial x}\right] . \tag{3.49}$$

The blending function is defined as

$$\begin{aligned} arg_1 &= min\left(max\left[\frac{\sqrt{K}}{0.09\omega y}\ ;\ \frac{500}{y^2\omega Re}\right]\ ;\ \frac{4\sigma_{\omega 2}K}{CD_{K\omega}y^2}\right), \\ CD_{k\omega} &= max\left(2\sigma_{\omega 2}\frac{1}{\omega}\frac{\partial K}{\partial x_j}\frac{\partial \omega}{\partial x_j}\ ;\ 10^{-20}\right)\ , \\ F_1 &= tanh(arg_1^4)\ . \end{aligned} \tag{3.50}$$

where $\sigma_{\omega 2}$ is σ_ω from set 2 in table (3.3).

Boundary conditions for ω is normally derived from the functional relation ship

$$\omega = \frac{6}{\beta_1 y^2 Re}\quad , \tag{3.51}$$

where β_1 is β from set 1 in table (3.3). By applying this relation ship at a boundary point above the surface a numerical error of around 33% for first derivatives and 78% for second derivatives will be produced if the derivatives are discretized by central approximations [62]. [1] This motivate for a cell vertex centered discretization scheme where the boundary condition of Menter [35]

$$\omega_A = \frac{60}{\beta_1 y_1^2 Re}\ ,\ K_A = 0\ , \tag{3.52}$$

can be applied. (y_1 is the normal distance from the wall to the first calculation point). This mean that the $K-\omega$ model is solved, in contrary to the BB and SA models, in grid points. The discretization is basicly the same as the one used for the BB and SA models applied to cell vertexes. The ADI scheme is also utilized for solving the algebraic equations. In both transport equations the destruction terms are treated implicitly and production terms is treated explicitly together with the cross-derivatives in the ω equation. First order upwind was utilzed for the convective terms. At inflow boundaries the values of K and ω are taken equal to

$$\omega_B = 5\ ,\ \nu_{t,B}^* = 10^{-3}\ ,\ K_B = \frac{\nu_{t,B}^*\omega_B}{Re}\ . \tag{3.53}$$

[1] The numerical error is defined as the deviation from the analytical solution and the actual solution found by the numerical solution.

A limitation of the produktion term for K as proposed by Menter has been implemented. The limiter is constructed as

$$P_k = min(P_k, 20 \cdot D_k) \ , \tag{3.54}$$

where D_k is the dissipation. As Menter claims this limiter prevent wiggles from forming in the shear-strain tensor and prevent unphysical buildup of eddy-viscosity in the stagnation region without affecting the gross flow.

3.5.2 The K-ω-SST turbulence model

The Shear-Stress Transport (SST) model is basicly the same model as the above described $K-\omega$-BSL model with an additional limiter that acts on the eddy-viscosity in the outer part of the boundary layer. The model has some similarity with the Johnson-King model [24] and attempts to account for the important effect of the transport of the pricipal turbulent shear-stress

$$\frac{D\tau}{Dt} = \frac{\partial \tau}{\partial t} + U_i \frac{\partial \tau}{\partial x_i} \ , \tag{3.55}$$

where $\tau = -\rho\overline{uv}$. The limiter is based on the Bradshaw's assumptions,

$$\tau = \rho a_1 K \ , \tag{3.56}$$

with a_1 being a constant. The modified eddy-viscosity is then given by

$$\nu_t = \frac{a_1 K}{max\left(a_1\omega; \gamma F_2\right)} Re \ , \tag{3.57}$$

where

$$F_2 = tanh\left(arg_2^2\right), \quad arg_2 = max\left(2\frac{\sqrt{K}}{0.09\omega y}; \frac{500}{y^2 \omega Re}\right) \ , \tag{3.58}$$

with $a_1 = 0.31$. The constants in the transport equation remains unchanged except for σ_{k1} which changes to 0.85 instead of 0.5

3.6 Transtion

Following the discussion in chapter 1, the process where a flow undergo transtion to a turbulent flow is rarely seen as a sharp interface between

the two states of the flow. Numerical the transition process is devided into two related problems. First, the onset point where the first turbulent flow is present and second the distance where the flow is part-time turbulent before becoming fully turbulent known as the transition length.

Several calculation methods for determining the point of transition has been suggested in the past. These methods can be grouped in methods based only on experimental and analytical methods with inherent empiricism [41] [7]. A very good ingeneering approach, based on experiments, is the Michel criterion, [38] which is valid only for attached flow. In the Michel criterium comparison are made between respectively the Reynolds number based on θ and a distance s. The onset of transtion is assumed located where

$$Re_{\theta,tr} \sim 2.9 Re_{s,tr}^{0.4} \ , \tag{3.59}$$

with

$$Re_\theta = \frac{U_s(\delta)\theta}{\nu} \ , \ Re_s = \frac{U_s(\delta)s}{\nu} \ . \tag{3.60}$$

$U_s(\delta)$ is the total velocity at the boundary layer edge projected on the direction tangential to the airfoil s. s is a distance measured along the profile starting from the front stagnation point and θ is calcualted by the method outlined in chapter 2 section (2.5). The transition point is calculated at every time-station by evaluating Re_θ and Re_s along the airfoil starting from the front stagnation point.

Very little information is in general avaible for the length of the transition zone. Typically the intermittency is simulated by lowering the eddy-viscosity from values predicted by the utilized turbulence model with a intermittency factor [9], [32]. When calculating airfoil flows it is common to make the extension of the intermittency zone long enough to provide a smooth solution when the turbulence models are turned on. This will of course make the transition process very sensitive to the used Navier-Stokes solver. Different strategies has been applied to the turbulence models outlined in the sections above.

For the algebraic turbulence model, BL, the eddy-viscosity is put to zero in regions where flow is considered laminar. A smooth transtion is simulated by the intermittens function [19],

$$\nu_t^*(s) = \nu_{t,BL}^*(s) \cdot \left[1 - exp\left(-\frac{(s - s_{tr})}{g \cdot n \cdot \Delta s}\right)\right] \ , \tag{3.61}$$

where s is a distance measured along the surface of the airfoil, S_{tr} is the assumed position for transition and Δs is the length of the boundary cell at s_{tr}. The parameter g is taken equal to 0.36 and the actual value of $n \cdot \Delta s$ is chosen to give a smooth transition over 2-3 cells in the streamvice direction.

For the Spalart-Allmaras and Baldwin-Barth turbulence models only the convetive part of the transport equations is maintained in laminar regions. For the $K - \omega$ model only the production and destruction terms are put to zero in laminar flows in order to achieve a smooth transtition. For all transport models a smoothing was applied when introducing the viscous and production and destruction terms into the equations in turbulent flow situations. A linear smoothing was applied

$$\mathcal{F}_{tr} = \mathcal{F} \cdot min\left(1, \frac{s - s_{tr}}{\Delta s}\right) \quad , \tag{3.62}$$

where $\mathcal{F}$ can be any terms of production, destruction or viscous.

3.7 Turbulence models applied in non-inertial systems

The turbulence models outlined above is of course also applicable in a non-inertial coordinate system as this is only a practical way of solving the Navier-Stokes equation in case of a moving solid body. On the other hand care should be taken when evaluating quantities involving vorticity. As shown chapter 2 vorticity is not invariant to the choise of reference system and eddy-viscosity is not alowed to be generated just because of another choise of reference system. The inner eddy-viscosity calculated by the Baldwin-Lomax model

$$(\nu_t^*)_{inner} = Re \cdot l^2 |\gamma^I| \quad , \tag{3.63}$$

has to be applied only in the inertial coordinate system of reference. Other wise additional eddy-viscosity would be introduced by an amount proportional with $2\Omega_{rot}$. The equatity y^+ used in damping function must also be based on $|\gamma_A^I|$ in order to be consistent. Considering the strain rate tensor S_{ij}, which is used in production terms, it can easily be shown, by direct calculation, to be invariant to the choise of reference system. When solving transport equations for a turbulent quantity, in a non-inertial coordinate system the relative velocities and the vorticity in the inertial system are applied.

Chapter 4

Turbulent flow past a flat plate

A flow past a flat plate is a simple test case for a turbulent Navier-Stokes calculation if the transition from laminar to turbulent flow is left out of account. In the simplest form only a mild pressure gradient exist in the direction along the plate and no steep gradients are present in the flow. A large knowledge is also available through measurement and it is widely believed that the velocity profile follows an universal law, known as the log-law or the law of the wall. All the implemented turbulence models are based on the assumption of the existence of such log layer limited by a laminar sub-layer below and a outer region on top. Constants in turbulence models are typical tuned by require the velocity to obey the law of the wall

$$u^+ = \frac{1}{\kappa} ln(y^+) + B \quad \kappa = 0.41 \;\; B = 5.0 \;\; , \tag{4.1}$$

for y^+ greater than some value typical around 15. (The integration constant B can normally not be enforced the turbulence models). In the laminar sub-layer below the log-layer the velocity is supposed to follow the functional relation ship

$$u^+ = y^+ \quad . \tag{4.2}$$

As turbulence models typical are made up by assuming eq.(4.1) and eq.(4.2), it is crucial to test an implementation of a turbulence model for a flow where such a velocity distribution should present. If we consider a flow with no or mild pressure gradient along a flat plate it is known that the velocity should follow eq.(4.1) and eq.(4.2) if the Reynolds number based on momentum thickness, Re_θ, is greater than 670, [51].

4.1 Numerical setup

Even though the present code is able to calculate flow past a flat plate with zero thickness another variant of the flat plate calculation has been performed in this case. As the code is developed to handle a c-grid topology used for airfoil flows a c-grid is wrapped around a plate with finite thickness. The leading edge is described by a semi circle and the trailing edge is made by collapsing the two last point of the plate into a single point. This geometry is shown below

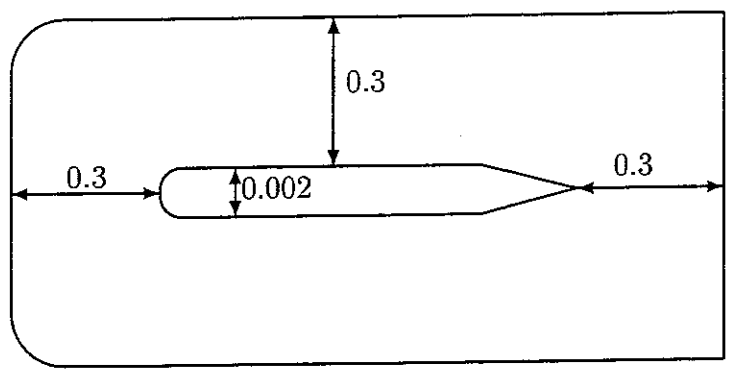

Figure 4.1: *C-grid wrapped around a flat plate. The thickness of the plate has been drawn in another scale.*

Another important aspect can be tested by this geometry namely symmetry of the flow solver. It is the authors believe that if the solver calculate a symmetric solution no implementation errors has been made concerning indexing and the solution algorithm used for solving across the wake can strongly be relied upon in this manner. A requirement is of course that a symmetric solution exist. The Base-function can also be tested in this case as it is known that the Base-function should not be active for this case with zero incidence.

Boundary conditions outlined in chapter 2 section (2.3.1) are utilized at the far-field and inflow boundaries. At outflow boundary inviscid convection of vorticity is applied together with a Neumann condition for the stream-function

$$\frac{\partial \psi}{\partial \xi} = 0 \ . \tag{4.3}$$

The outflow condition for ψ, eq.(4.3), assumes flow parallel to the on-coming flow and is necessary because the outflow boundary is located in a short distance from the trailing edge. By applying far field boundary conditions it is guaranteed that no flow can cross the extremities of the calculation domain, except at the outlet boundary. This is similar to a channel flow with the outer most grid line located in the line of symmetry. In order not to have the flow influenced by a strong pressure gradient the far field boundary is located in a safe distance from the wall.

4.2 Results for flow past a flat plate with finite thickness

In the following results for the geometry described in the section above will be shown. Results will be given in form of velocity plots in wall coordinates and skin friction distribution for a flow with a Reynolds number equal 2 million. The flow has been calculated on different grids where the height of the cell next to the wall was decreased together with increasing the total number of grid points until virtually no changes was observed. The final grid consist of $(nx, ny, nk) = (173, 85, 13)$ with a height of the cell next to the wall of $2 \cdot 10^{-5}$. The total grid together with a zoom of the leading edge is shown on Fig.(4.2).

As the flow configuration is quite similar to an airfoil calculation the convergence history shown in Fig.(4.3) is representative for the Navier-Stokes solver when applied to airfoil flows. The code has been running until the residual was decreased to 10^{-10}, (see chapter 2 section (2.3.2) for the definition of the residual). The convergence of the Navier-Stokes solver applied with the various turbulence models are similar except for the Baldwin-Barth model when comparing the non-dimensionalized time spend to achieve convergence. When measurering the actual cpu time spend greater deviations occurs. In table (4.1) the utilized time step is shown together with the measured time consumption per iteration and the total number of iteration needed. Δt is the time step. δt is cpu time consumption per time step measured over 5000 iterations. N. of iter. is the total number of iteration needed for the calculation. CPU is the total cpu time spend without pre- and post-processing. (The utilized computer was an IBM RISC 6000, model 591).

	BL	BB	SA	$K-\omega$-BSL	$K-\omega$-SST
$\Delta t \cdot 10^4$	2.47	2.25	2.25	2.70	2.70
δt $[s/i]$	0.808	0.983	1.052	1.088	1.162
N. of iter.	8956	11038	8925	7094	7371
CPU $[s]$	7237	10850	9389	7718	8565

Table 4.1: *Statistics for the various turbulence models when applied to a flat plate calculation.*

The results shown in table (4.1) reveals some very interresting general features for the utilized turbulence models. Even though the 2-equations turbulence models solves twice as many equations as the 1-equation models they are less expensive concerning cpu time. One explanation for the low time consumption is the higher available time-step. The time-step used for the calculations are the largest possible in order to get a converged solution. The ratio between the used time step for the turbulence models are common also for airfoil calculations. In general it is difficult to settle if it is the turbulence model that makes the solver stiff or the underlying Navier-Stokes solver because both has limitations of the time-step and the problem is strongly coupled so the solver must be regarded as such. On the other hand, the number of floating point operations for different turbulence models can be compared. In general the algebraic and one-equation turbulence model requires calculation of damping function based on square roots and power terms which are quite expensive in terms of floating point operations. The $K-\omega$ model is distinguished by presence of only one square root term and otherwise squared terms.

The symmetry of the flow has been evaluated by considering the value of the streamfunction at the plate when the residual was decreased to 10^{-10}. It is known that the correct value of ψ_{wall} equals 0. If the solver does not calculate a symmetric flow lift will be generated forcing ψ_{wall} to a value away from zero by the requirement of a unique pressure on surface of the plate. The calculated values of ψ are listed in table (4.2). As the table indicate the flow must be considered as symmetric.

On Fig.(4.4) velocity profiles are depicted in wall coordinates. Comparisons are made with eqs.(4.1) and (4.2), (intersection is set at $y^+ = 11.6$). As one can observe the models can be grouped in two. The BL and the BB

	BL	BB	SA	$K-\omega$-BSL	$K-\omega$-SST
ψ_{wall}	$-2.6 \cdot 10^{-9}$	$5.9 \cdot 10^{-10}$	$-2.4 \cdot 10^{-9}$	$-2.5 \cdot 10^{-9}$	$-1.8 \cdot 10^{-9}$

Table 4.2: *Wall streamfunction values, ψ_A, for a converged solution of a flow past a flat plate*

models both predicts a strong wake at the outer part of the boundary layer and a good agreement with the log-law in major parts of the boundary layer. The SA and the $K-\omega$ models predicts a mild wake and a sooner deviation from the log-law.

Skin friction distributions for the different turbulence models is depicted at Fig.(4.5) where also

$$C_f = 0.0576 Re_x^{-0.2} \quad , \tag{4.4}$$

valid for $Re_x < 10^7$ is plotted, (From [2]). Common for all the models are a drop in skin friction close to the initiation of the plate and the wiggles in the trailing edge region. All models except the SA model produces similar skin friction distributions which not agree especially good with eq.(4.4) in the leading edge region, properly due to the influence of the rounded leading edge. The wiggles observed at the trailing edge is common for the utilized code and is due to the singular behavior of the vorticity at the trailing edge which can be felt some distance away. A poor discretization in this region will amplify this effect. Finally the value of δ and Re_θ was considered and the values are shown in table (4.3) together with reference values,

$$\frac{\delta}{x} = 0.37 \cdot Re_x^{-0.2} \quad Re_\theta = 0.0142 \cdot Re_x^{6/7} \quad , \tag{4.5}$$

valid for $Re_x < 10^7$ [59].
As table (4.3) indicate quite large variation are found in Re_θ and δ but these was expected when comparing the velocity in the outer part of the boundary layer shown on Figs(4.4).

4.3 Summary

The BL, BB, SA, and $K-\omega$ turbulence models has been used for calculating flow past a flat plate. It was found that all models predicts a velocity distribution in good agreement with the law of the wall and the final solution is

	BL	BB	SA	$K-\omega$-BSL	$K-\omega$-SST	Eq.(4.5)
$\delta \cdot 100$	2.54	1.75	2.11	2.25	1.97	2.03
Re_θ	3419	3252	3226	3443	3325	3574

Table 4.3: *Boundary layer thickness and Re_θ for a flat plate calculation. The values are found at $x/c = 0.95$.*

symmetric. Comparing skin friction with an empirical relation showed good agreement mainly in the trailing edge region. The skin friction obtained with the SA model deviate slightly from the other models. Comparing the cpu time consumption needed for getting a converged solution showed that the BL and the $K-\omega$ models was less expensive to use than the two 1-equation models BB and SA.

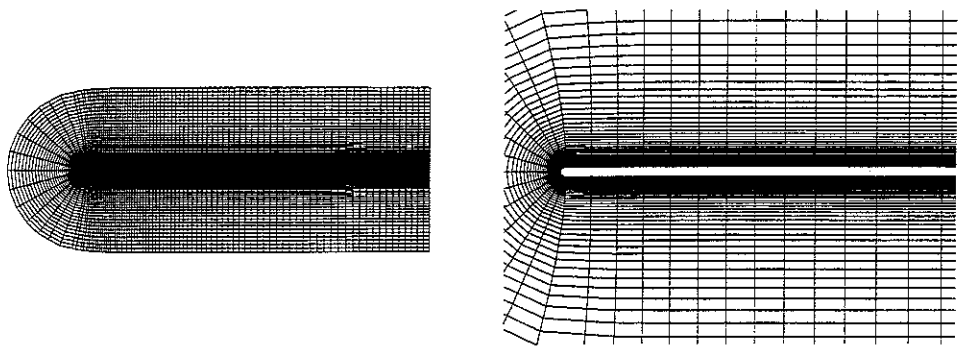

Figure 4.2: *C-grid wrapped around a flat plate.*

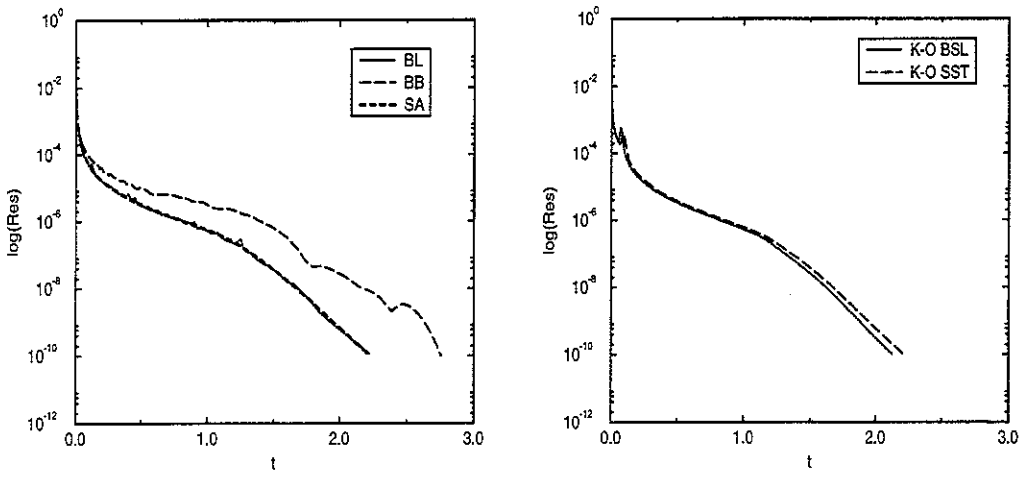

Figure 4.3: *Convergence history for a flow past a flat plate with rounded leading edge. The flow is calculated with the turbulence models outlied in chapter 3 and with a Reynolds number of 2 million.*

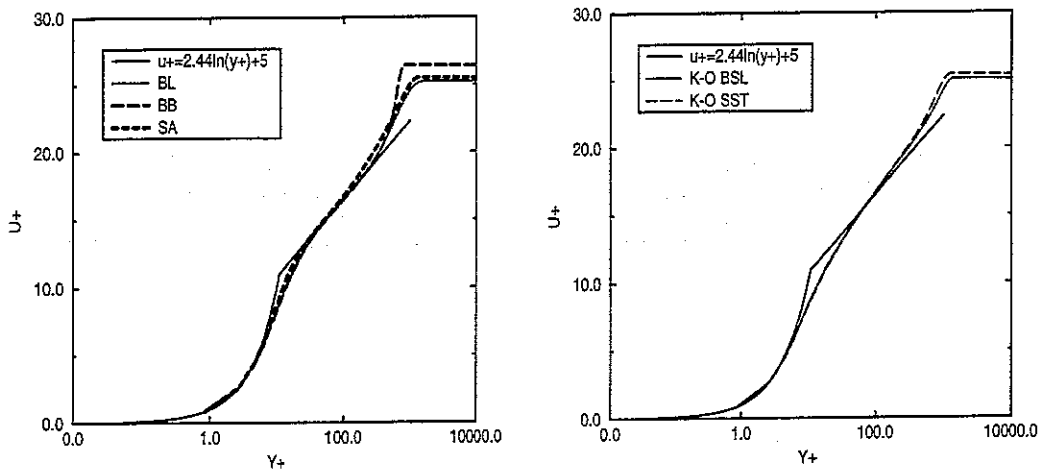

Figure 4.4: *Mean velocity profile calculated with the turbulence models outlied in chapter 3 on a plate with rounded leading edge. The flow is calculated with a Reynolds number of 2 million. The velocity profiles is taken at position x/c=0.95.*

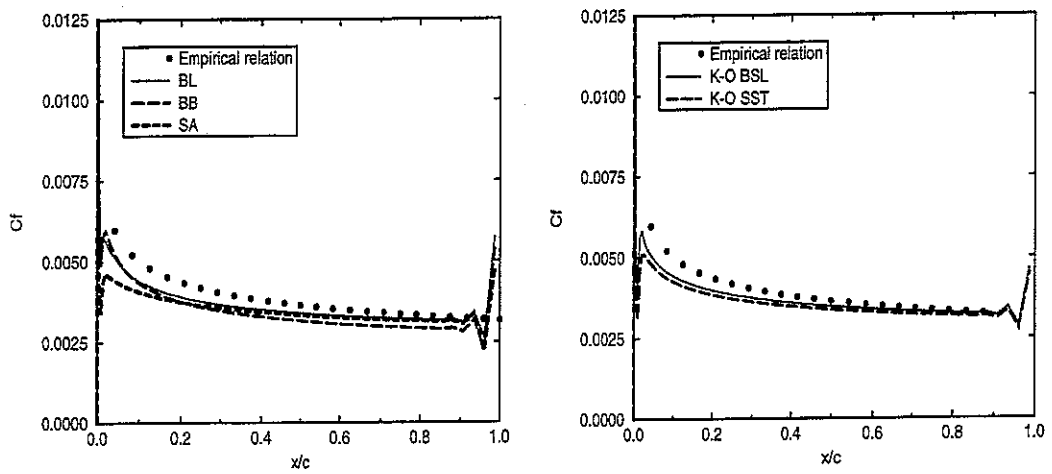

Figure 4.5: *Skin friction distribution calculated with the turbulence models outlied in chapter 3 on a flat plate with rounded leading edge. The flow is calculated with a Reynolds number of 2 million.*

Chapter 5

Laminar flow past airfoils

One of the purposes with the Navier-Stokes code described in the previous chapters was to develop a solver capable of calculating time varying flows. The implementation of the turbulence models described in chapter 3 is considered as an extension to the developed laminar Navier-Stokes solver and it is by this crucial to validate the laminar part of the solver. Three laminar flow situations has been examined, a stationary flow past a NACA 0012 airfoil at low incidence and low Reynolds number, an impulsive start of a NACA 0012 airfoil at low Reynolds number and high incidence, and an oscillating NACA 0012 airfoil at low Reynolds number and moderate incidence.

Visualization taken from the literature are compared with calculated instantaneous streamlines. The visualizations are carried out by photograph of particle trajectories as in unsteady flow near the surface of an airfoil represent neither streamlines nor streaklines. On the other hand, if the exposure time is short enough the traces will coincide nearly with instantaneous streamlines. In the flow situations shown here, where such a good agreement is found between visualizations and computations this minor discrepancies was ignored.

Oscillatory airfoil flow effects, known as dynamical stall effects, will be addressed when it is appropriate. In a later chapter dynamical stall effects will be discussed in details.

5.1 Laminar stationary flow past a NACA 0012 airfoil

In order to validate the laminar flow solver a comparison is carried out with results obtained with a Navier-Stokes solver in primitive variable form developed by N. N. Sørensen [50]. The primitive variable solver, called EllipSys2D, has in many cases provided accurate airfoil data in laminar and turbulent flow situations. The results presented in this content with EllipSys2D has kindly been produced by assistant professor M. Hansen, Technical University of Denmark.

The flow situation to be studied consist of a flow past a NACA 0012 airfoil with an incidence of 3^o. The Reynolds number was taken equal to 1000 and the grid consist of 337 grid points around the airfoil and wake with 49 points in the wake. In the direction normal to the airfoil surface 49 points was distributed with a cell height of the first cell next to the airfoil of $1 \cdot 10^{-3}$. The relative low incidence was chosen for the flow to be stationary but still high enough for the airfoil to produce an appreciable lift necessary for the testing of the Base-function.

On Fig.(5.1) the pressure and skin friction distribution on upper and lower surface of the airfoil are shown. As shown on these two figures virtually equal skin friction distribution was predicted with the two Navier-Stokes solvers, whereas deviations occur mainly in the leading edge region for the pressure distribution. Closely inspection of the skin friction distribution predicted by the two Navier-Stokes solvers prevail small differences in the peak values close to the leading edge. As the pressure in the $\gamma - \psi$ formulation is calculated by the derivatives of γ at the wall, a deviation will be expected in the pressure when the surface distribution of vorticity not is identical for the two Navier-Stokes solvers. As the two different Navier-Stokes solvers predicts similar results in this case and EllipSys2D is widely tested and a good accordance with experiment normally is found it is believed that the present $\gamma - \psi$ formulation also is able to produce reliable results, at least in this case.

5.2 Impulsive start of a NACA 0012 airfoil

In this section an impulsive start of a NACA 0012 airfoil will be considered. The Reynolds number is 1000 and the angle of attack is 34^o. The flow is calculated on a grid with the dimension of 225 grid points in the direction

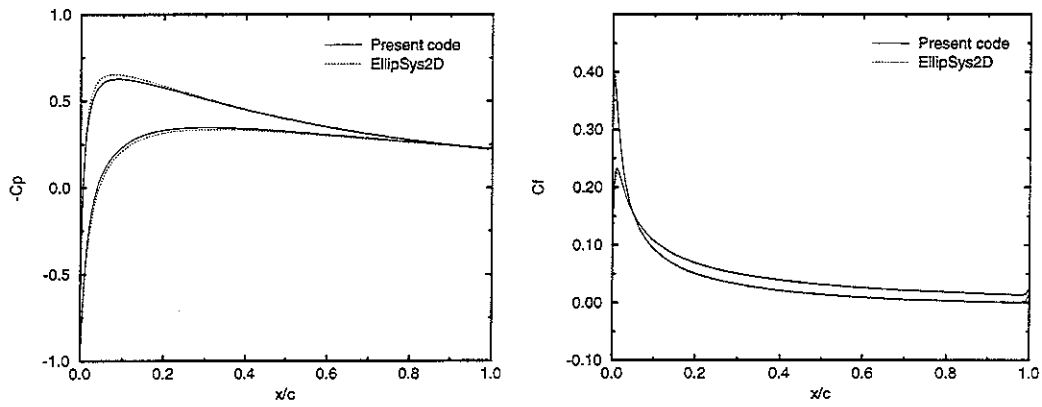

Figure 5.1: *Pressure and skin friction distribution for laminar flow past a NACA 0012 airfoil with an angle of attack $\alpha = 3^o$. The flow was calculated by utilizing a primitive variable and a $\gamma - \psi$ formulation of the Navier-Stokes equations.*

around the airfoil, 33 grid points in the wake and 91 grid points in the normal direction. The height of the cell next to the airfoil was taken equal to 10^{-3} and the applied time step was $\Delta t = 10^{-3}$. The grid was extended 12 chord lengths away in all directions.

At $t = 0$ the flow was at rest. For t greater than zero the flow development is depicted on Figs.(5.4) to (5.13). The development of C_L is depicted in Fig.(5.3). The figures showing instantaneous streamlines are compared with visualizations reported in [11]. Later when referring to structures in the flow this is done by f.i.: "the leading edge vortex, *1* on Fig.(5.4),". Generally an excellent agreement is found when the calculated flow is compared with the visualizations.

As the flow evolve from rest at $t = 0$ to $t = 0.4$, Fig.(5.4), a separation bubble, *1*, builds up at the leading edge. At the same figure the starting vortex *0* originating from moving the rear stagnation point to the trailing edge is convected out into the wake flow. The lift has in the same period dropped from a very high initial value to a local minimum and as the boundary layer is developing the lift begins to increase.

As the leading edge separation bubble, *1*, grows bigger and moves further downstream two new separation bubbles, *2* and *3*, are formed near the leading

edge as seen on Fig.(5.5) at $t = 1.6$. In between the primary leading edge separation bubble, *1*, and the newly created leading edge separation bubble, *3*, a counter clock vice rotating bubble, *2*, exist. The structures formed by *1,2,3* is felt as a thickening of the airfoil which means that the lift is increased due to the attachment of the flow at the trailing edge. The counter rotating bubble, *2*, and the primary leading edge bubble, *1*, is enlarged at $t = 2.8$ as seen on Fig.(5.6). As the primary leading bubble, *1*, is further enlarged the flow de-attach at the trailing edge and the lift starts to decrease. At the same time a new counter rotating trailing edge vortex, *4*, is formed.

At Fig.(5.7) the trailing edge vortex, *4*, has become bigger and a local lift minimum is formed. The flow situation is quite similar to the flow situation at $t = 2.8$ except that the trailing vortex, *4*, is bigger in this case.

The vortex pair consisting of *2* and *4* begins to merge at $t = 3.6$, Fig.(5.8), and the process is initiated by the growth of the trailing edge vortex, *4*. This merging process together with a convection and diffusion process governs the movement of the primary leading edge vortex, *1*, in to the wake as shown on Fig.(5.8). As the trailing edge vortex, *4*, is enlarging the lift is slightly increased. At $t = 4.0$ the merging process of *2* and *4* is nearly finished and the lift decreases slowly. At $t = 4.4$ a large separation area exist, *4* on Fig.(5.10), at the trailing edge, an elongated vortex, *3*, at the leading edge and the primary leading edge separation, *1*, is located in the wake. The lift is advancing a global lift minimum in the investigated time period at $t \sim 4.6$.

At $t = 4.8$ the trailing edge separation, *4* on Fig.(5.11), has started to enter the wake flow. As the trailing edge separation is brought out into the wake, the flow close to the trailing edge is no longer felt as a separation but more as an attached flow. This flow situation will begin to raise the lift as seen on Fig.(5.3). A short living vortex, *6* on Fig.(5.11), is formed as a consequence of the break up of the leading edge bubble, *3* at Fig.(5.10), into two distinct vortices *3* and *5*.

At $t = 5.2$, Fig.(5.12), the flow situation is similar to the earlier realization at $t = 1.6$. Two relatively large separation areas exist, *5* and *3*, in the leading edge and mid-chord regions of the airfoil and the flow is attached in the trailing edge region. The flow situation at $t = 5.2$ is said to attached in the trailing edge region because the center of the vortex now is located behind the trailing edge. The reattachment process from $t = 4.8$ to $t = 5.2$ rapidly increase the lift until a local maximum is established at $t \sim 5.4$. After this local maximum the vortex, *3*, expands and the flow becomes fully separated at the trailing edge and the lift begins to drop.

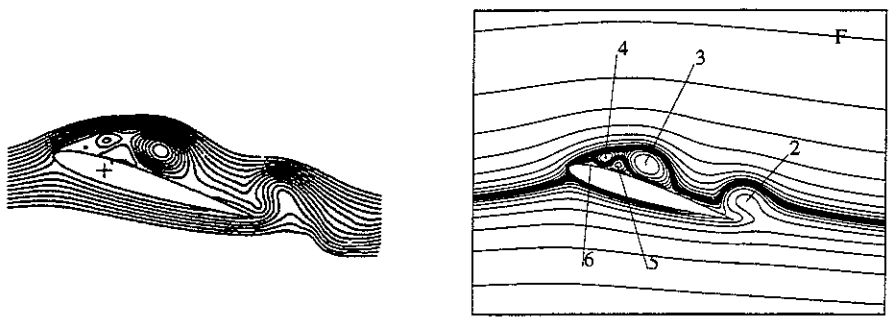

Figure 5.2: *Instantaneous streamlines for and oscillating NACA 0012 at an angle of attack* 17.42 ↓. *Left: From [37]. Right: Present calculation.*

5.3 Flow past an oscillating NACA 0012 airfoil

The flow configuration to be studied consist of an NACA 0012 airfoil oscillating in pitch, for which visualizations has been carried out by Werle [37]. Comparisons are made between the visualizations and instantaneous streamlines in the inertial frame of reference. These comparisons are shown on Figs.(5.16) to (5.24). On Fig.(5.14) and (5.15) the aerodynamic coefficients, C_n, C_t and C_m, are shown together with a zoom of the applied grid. The pitching motion of the airfoil was conducted with the center of rotation located in $(x_0, y_0) = (0.25, 0)$ and with a reduced frequency $k = 0.5$. The sinusoidal pitching motion is centered around a mean angle of attack $\overline{\alpha} = 10^o$ and amplitude $\Delta\alpha = 10^o$. The Reynolds number is 5000. The utilized grid has 312 grid points around the airfoil with 91 grid points in the normal direction and 33 grid points in the wake. The height of the cell next to the airfoil surface was taken equal to $1.6 \cdot 10^{-4}$. In [37] oscillation was initiated after a stationary solution was found at the lowest incidence and by adopting the same procedure in the present calculation an eminent agreement is found between the two different computations as shown on Fig.(5.2).

On Fig.(5.14) the normal lift coefficient, C_n is depicted as a function of the incidence. As the lift is multi valued, depending on the way the incidence is reached, the lift curve is often referred to as a hysteresis curve or hysteresis loop. It is clearly seen that the upstroke lift coefficients are comparable with static ones, at least when the incidence is low, but not at downstroke where

the generated lift is not comparable with static ones and greatly exceed the static lift coefficient in some parts of the hysteresis curve. This is a distinguished feature of dynamical stall but because the Reynolds number is low and the flow is laminar the flow situation is normally not classified as dynamic stall. At least the upstroke part of the hysteresis curve has to some extend been described by the "Ericsson's mowing wall" [40] effect : When the back of the airfoil is displaced downwards the conventional boundary layer separation is delayed because of a time lag. This time lag is associated with the relative high velocity of the wall to the oncoming flow compared to the time needed to develop the boundary layer.

The flow at downstroke is govern by massive separation which is initiated at upstroke by formation of a leading edge and trailing edge separation bubble, *1* and *2* on Fig.(5.18). The formation of these two vortices is seen as the beginning of stall on the lift curve. When the incidence becomes high the static tendency to develop separation can still be compensated by the high momentum fluid in the boundary layer so the lift is still maintained at a high level. As the incidence becomes higher, $\alpha = 18.49^o \uparrow$, the high momentum fluid at the trailing edge can no longer compensate for the effect of moving the rear part of the airfoil downwards and separation, *2* on Fig.(5.18), is initiated at the trailing edge. Even though the flow has started to separate at the trailing edge the high lift is still present. Further more the time lag associated with the development of the separation are decreased due to the lowering of the angular velocity.

Reaching maximum incidence $\alpha = 20.00^o \rightarrow$, Fig.(5.19), the angular velocity goes to zero and the trailing edge separation *2* now quickly becomes larger. The leading edge vortex *1* breaks up into three new vortices *3,4* and *5* which are clearly seen on the visualization. The process is rapid and is may be related to an accumulation of vorticity in the leading edge region which suddenly roll up into a vortex. At maximum incidence the flow at mid-chord of the airfoil is still attached. The flow at the trailing edge is now fully de-attached and the lift has started to decrease.

At $\alpha = 17.42^o \downarrow$ the flow is entering a situation with a local minimum in lift. The primary trailing edge separation bubble, *2* on Fig.(5.21), is leaving the airfoil and the three leading edge vortices, *3,4,5*, has enlarged and yet another small vortex, *6*, is formed in the leading edge region.

After the local lift minimum is passed the flow situation at $\alpha = 11.39^o \downarrow$, Fig.(5.22), produces a lift which is higher than the value produced at the upstroke part of the hysteresis curve. The flow structures is quite organized

with a sequence of counter and clock vice rotating vortices along the upper side of the airfoil as seen on Fig.(5.22). The flow is now heading towards a situation with a local lift maximum.

As the vortices at the upper side of the airfoil are brought downstream by convection these growth bigger as seen on Fig.(5.23) for $\alpha = 4.72^o \downarrow$. When the flow passing on top of the vortex, *3* on Fig.(5.23), no longer come close to the trailing edge, as the vortex moves towards the wake, a lift maximum is passed and the lift now quickly becomes smaller. This process continues until the vortex *3* virtually is in the wake and the flow at the trailing edge begin to re-attache, Fig.(5.23).

From $\alpha = 4.72^o \downarrow$ and until $\alpha \sim 2^o \downarrow$ the lift coefficient is similar to the values at upstroke part. After this the lift suddenly is increased due to a flow situation where the pattern of the separation, *4,6,7* on Fig.(5.24), is felt as a thickening of the airfoil due to the attached flow at the trailing edge. The lift increases until the vortex *4* on Fig.(5.24) begins to leave the airfoil.

5.4 Summary

Comparing pressure and skin friction distribution for a NACA 0012 airfoil at 3^o of incidence and with a Reynolds number equal 1000 obtained by the present $\gamma - \psi$ formulation of the Navier-Stokes equation and a primitive variable formulation showed small deviations mainly in the leading edge pressure distribution.

The Navier-Stokes solver has been tested and compared with experiments for two different types of time varying flows. It was found that both the calculation of the instantaneous start and the oscillating airfoil showed good agreement when comparing instantaneous streamlines with streaklines obtained experimentally. This conclude that the Navier-Stokes are able to compute a time varying flow for both a stationary and oscillating airfoil.

Some indication of how flow structures are organized in a separated flow which exhibits high or low lift was found. It was found that when the flow was separated and the streamlines limiting the massive separated areas, from the non-separated outer flow, gets close to the trailing edge of the airfoil a situation with high lift was encountered. When these streamlines did not get close to the trailing edge a situation with low lift was encountered. These features was found in the non-oscillating airfoil flow as well in the oscillating airfoil flow.

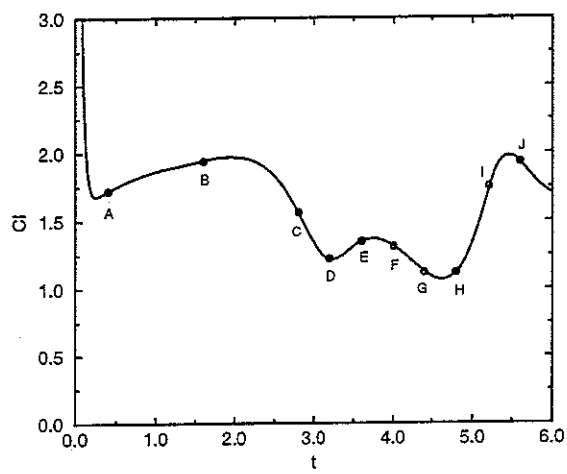

Figure 5.3: *Lift coefficient as function of time. The circles indicates positions for the plots presented in Figs.(5.4) to (5.13).*

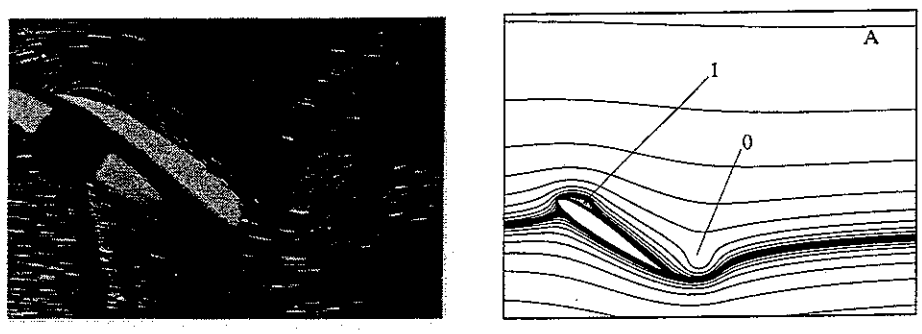

Figure 5.4: *Flow situation for an impulsive start of a NACA 0012 airfoil at t=0.4.*

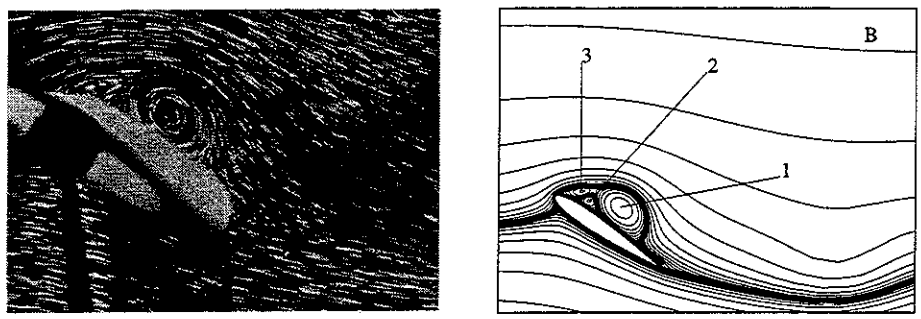

Figure 5.5: *Flow situation for an impulsive start of a NACA 0012 airfoil at t=1.6.*

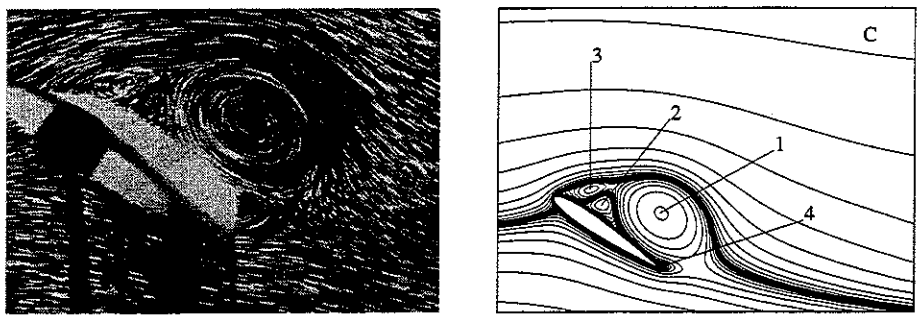

Figure 5.6: *Flow situation for an impulsive start of a NACA 0012 airfoil at t=2.8.*

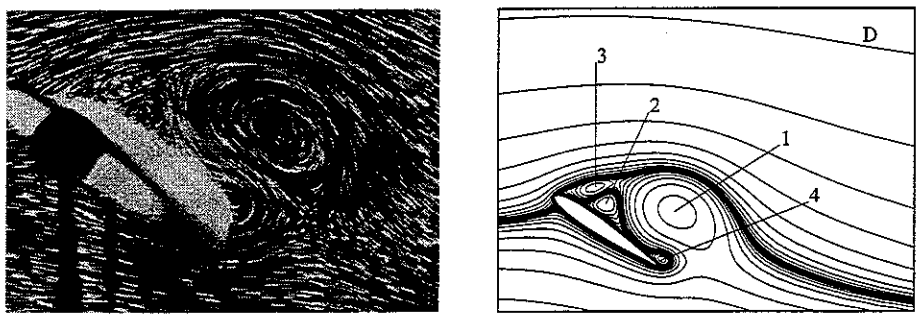

Figure 5.7: *Flow situation for an impulsive start of a NACA 0012 airfoil at t=3.2.*

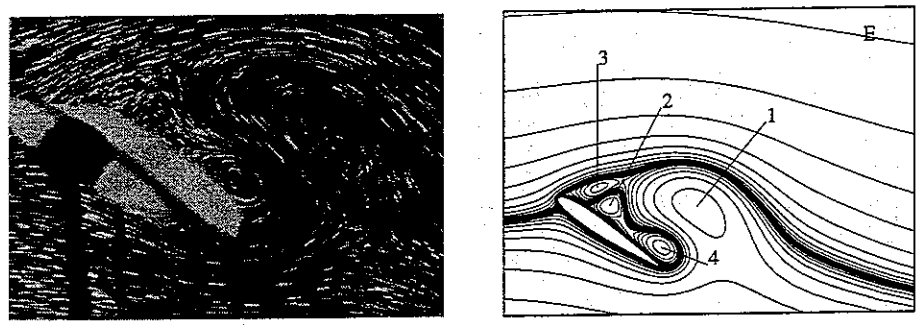

Figure 5.8: *Flow situation for an impulsive start of a NACA 0012 airfoil at t=3.6.*

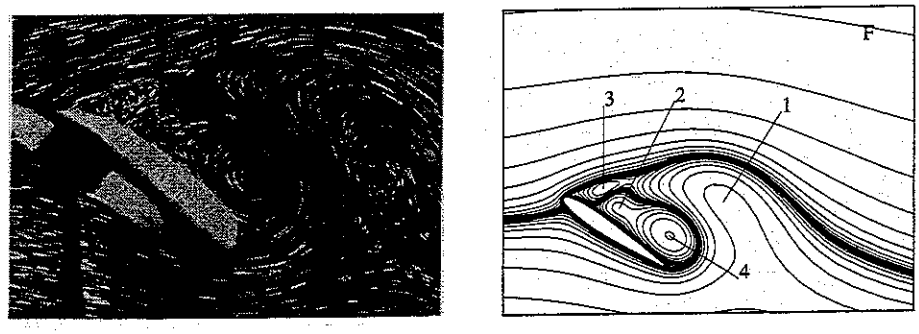

Figure 5.9: *Flow situation for an impulsive start of a NACA 0012 airfoil at t=4.0*

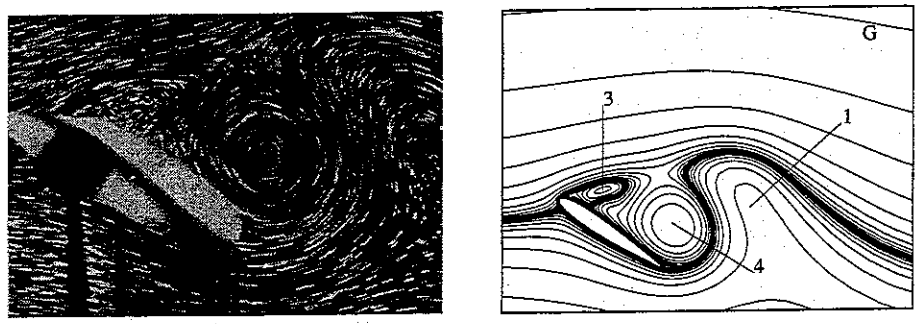

Figure 5.10: *Flow situation for an impulsive start of a NACA 0012 airfoil at t=4.4.*

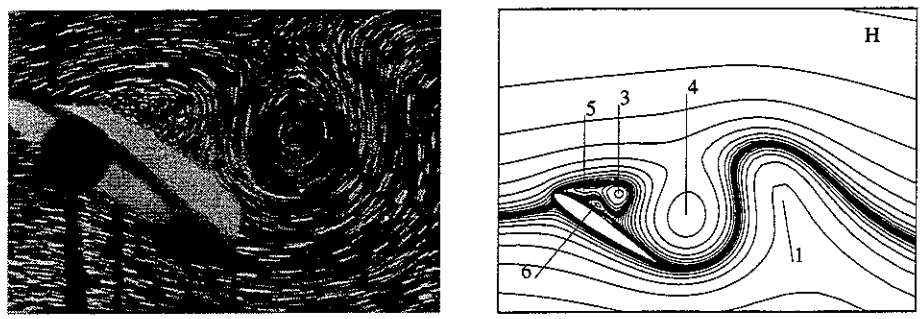

Figure 5.11: *Flow situation for an impulsive start of a NACA 0012 airfoil at t=4.8.*

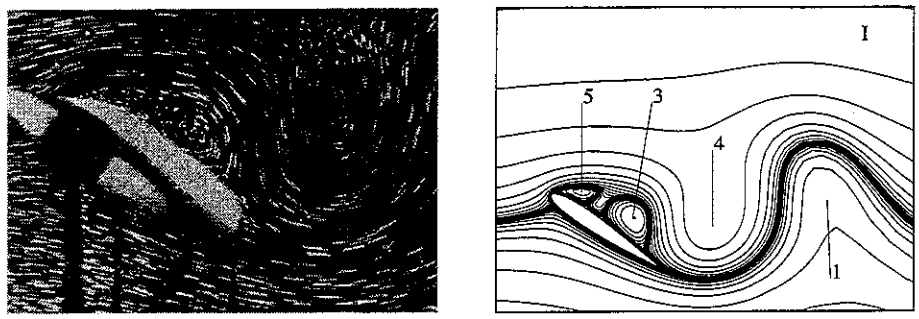

Figure 5.12: *Flow situation for an impulsive start of a NACA 0012 airfoil at t=5.2.*

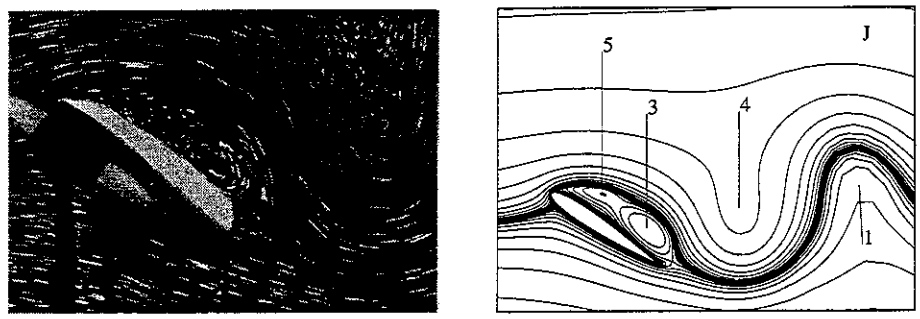

Figure 5.13: *Flow situation for an impulsive start of a NACA 0012 airfoil at t=5.6.*

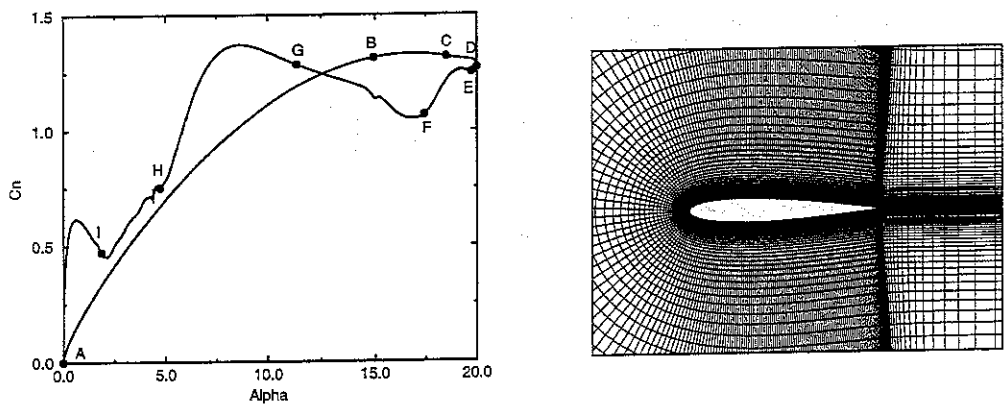

Figure 5.14: *Normal coefficient, C_n, hysteresis curve and utilized grid for an oscillating NACA 0012 airfoil. Re= 5000, $k = 0.5$, $\overline{\alpha} = 10^o$, $\Delta\alpha = 10^o$. The circles indicates positions for the plots presented in Figs.(5.16) to (5.24).*

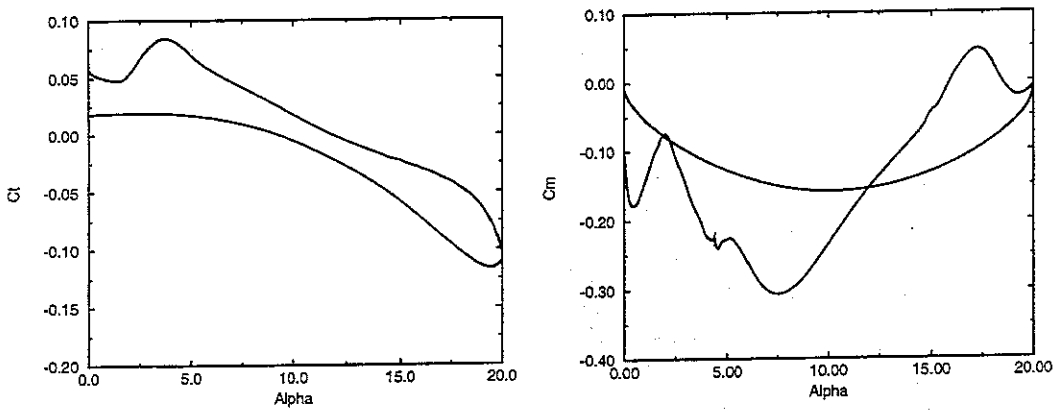

Figure 5.15: *Tangential coefficient, (C_t), and moment coefficient, (C_t), as function of the angle of attack α.*

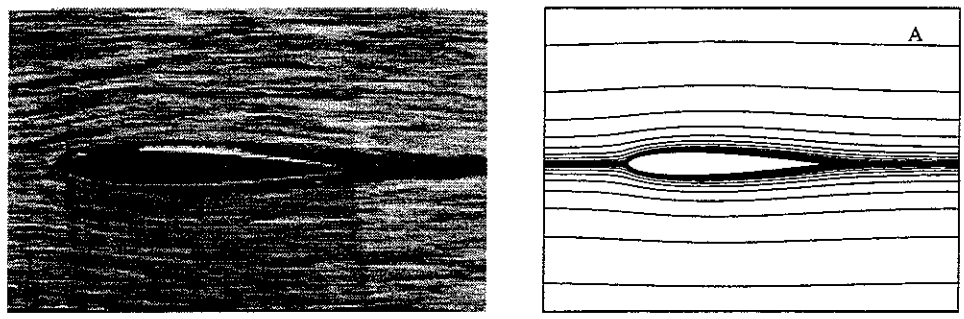

Figure 5.16: *Flow situation for an oscillating NACA 0012 at* $\alpha = 0^o$.

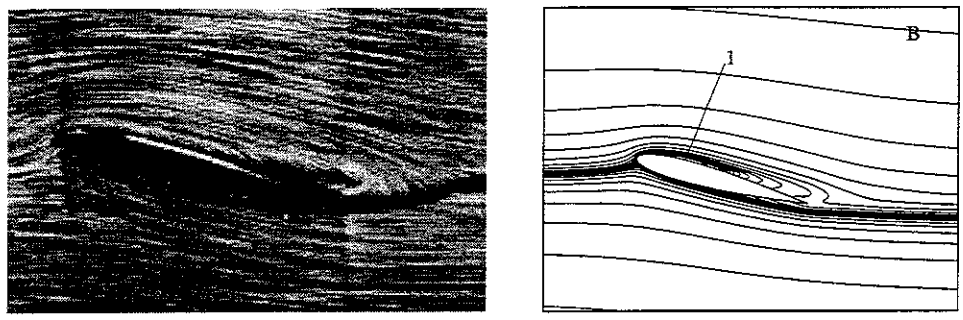

Figure 5.17: *Flow situation for an oscillating NACA 0012 at* $\alpha = 14.94^o \uparrow$.

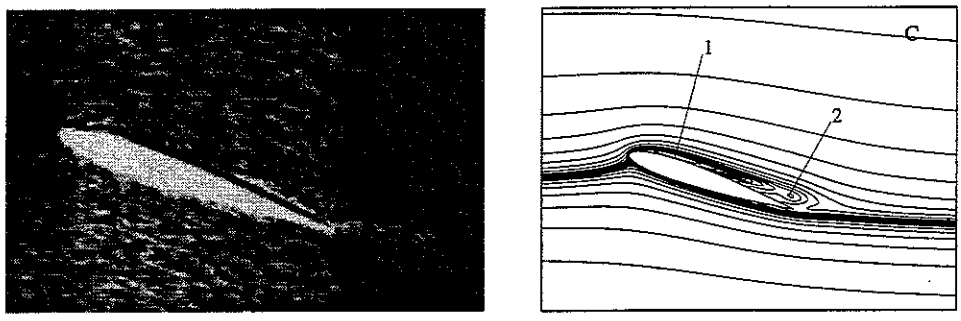

Figure 5.18: *Flow situation for an oscillating NACA 0012 at* $\alpha = 18.49^o \uparrow$.

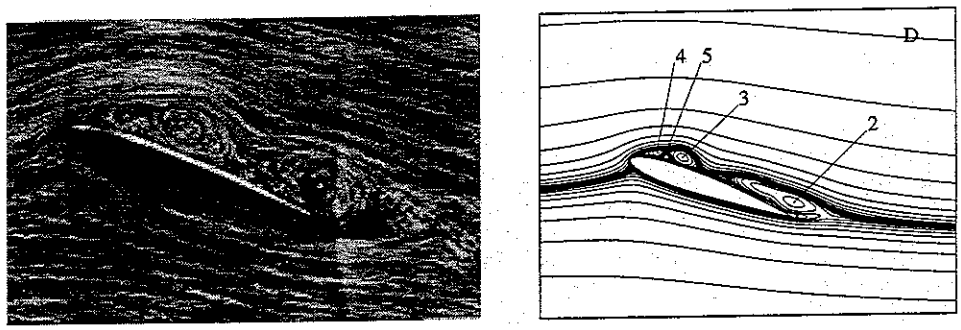

Figure 5.19: *Flow situation for an oscillating NACA 0012 at* $\alpha = 20.00^o \rightarrow$.

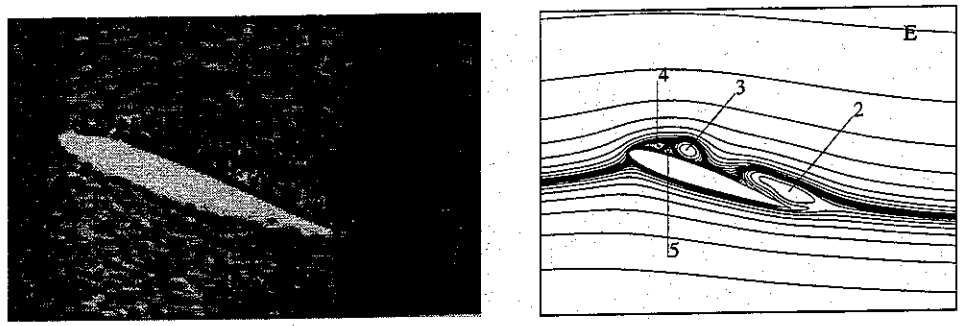

Figure 5.20: *Flow situation for an oscillating NACA 0012 at* $\alpha = 19.72^o \downarrow$.

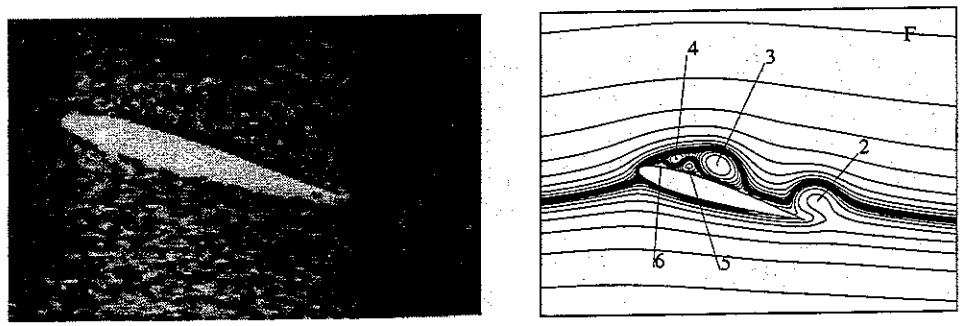

Figure 5.21: *Flow situation for an oscillating NACA 0012 at* $\alpha = 17.42^o \downarrow$.

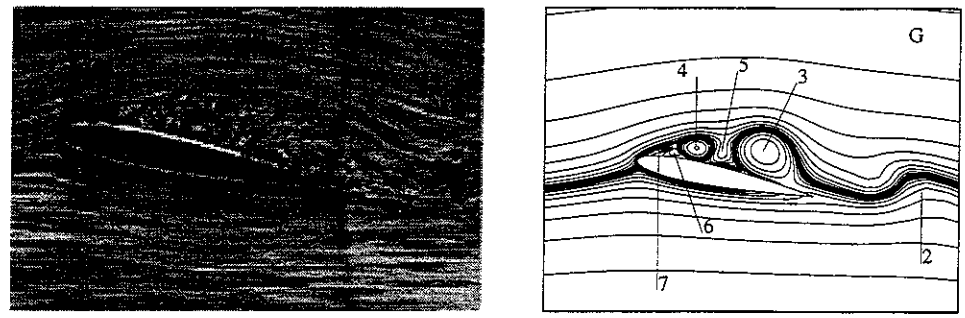

Figure 5.22: *Flow situation for an oscillating NACA 0012 at* $\alpha = 11.39^o \downarrow$.

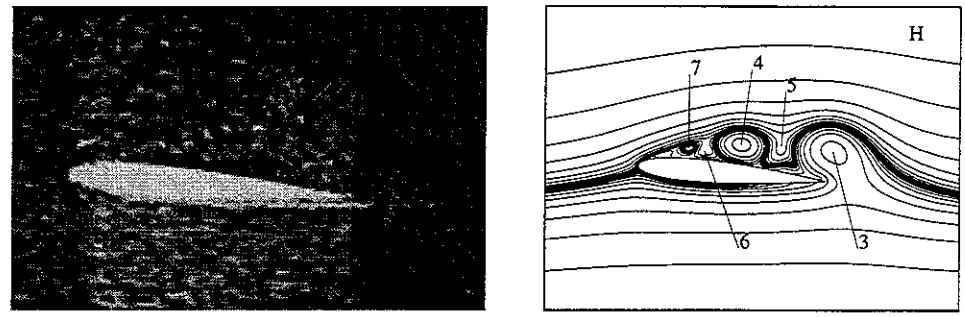

Figure 5.23: *Flow situation for an oscillating NACA 0012 at* $\alpha = 4.72^o \downarrow$.

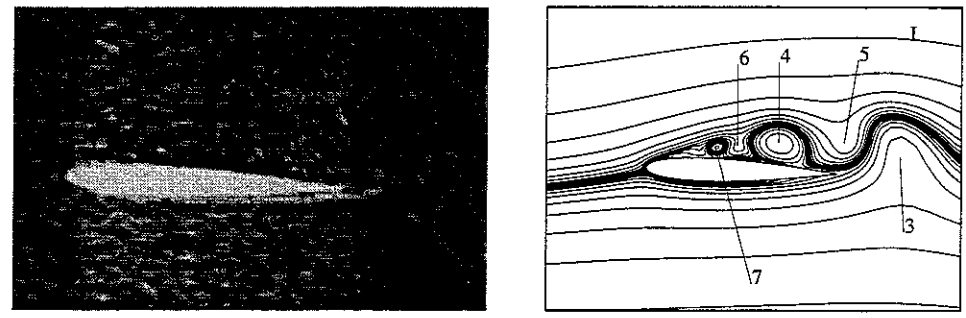

Figure 5.24: *Flow situation for an oscillating NACA 0012 at* $\alpha = 1.84^o \downarrow$.

Chapter 6

Turbulent flow past a stationary airfoil

The work presented in this chapter is partly done within the frame work of *ECARP : European Computational Aerodynamics Research Project, Part II "Validation of CFD Codes and Assessment of Turbulence Models"*.

The present work is focused on calculating flow past an Onera-A airfoil, see Fig.(6), for which a large number of experimental data are available through measurement conducted at the F1 and F2 wind tunnels at Onera in Toulouse, France. The accuracy of measurements is considered lower in the F2 than in the F1 wind tunnel and the difference is profounded at high incidences where the stall incidence measured in the two wind tunnels is considerable different.

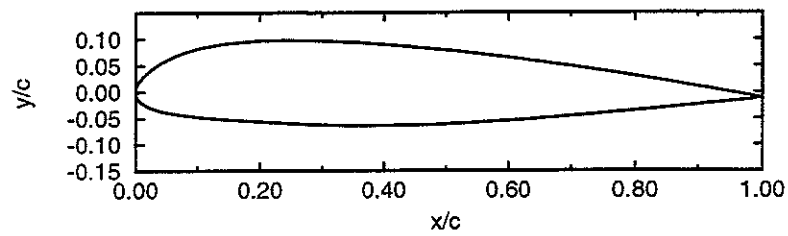

Figure 6.1: Geometry of the Onera-A airfoil

6.1 General discussion of flow past an Onera-A airfoil

The Onera-A airfoil is a suitable test case for computational fluid dynamics as the physics of the flow is well described through thoroughly conducted measurements. At the same time the flow is not easy calculated because transition and an interaction between a leading and trailing edge separation is believed to be present. This may on the other hands leave many open questions concerning how and where the transition from laminar to turbulent flow occur.

Within the frame work of *ECARP* some partners found that the prediction of a trailing edge separation strongly interact with the presence of a leading edge separation in the computation. If a leading edge separation was predicted the overall turbulence intensity could be increased, and by this also the downstream eddy-viscosity, causing the flow to be attached in the trailing edge region. It is believed that the correct pressure and skin friction distribution only can be predicted if the separation pattern was captured correctly.

For all the measurement transition is fixed by transition strips at $x/c = 0.3$ on the lower side and is free on the upper side. The presence of a leading edge bubble seams to be the origin of transition for most angles of attack. Analysis of skin friction measurement [19], leads to take a fixed transition at $x/c = 0.12$ at the upper side for all angles of attack. By calculation done by partners in *ECARP*, indications was found on that especially at angles of attack near stall that the transition position moves further upstream. In spite of that, the transition points was kept fixed at these positions. The reason for that was the basis of the *ECARP*-work where the main subject was to compare turbulence models and not to investigate the transition process. By this the danger of not knowing the capacity of flow prediction of the applied turbulence models was introduced, when they was applied with a process which does not follows the physical transition mechanism.

Many partners within ECARP applied a local time stepping algorithm for solving the Navier-Stokes equations. The use of a local time step has no influence on the flow as long as the flow is stationary. As will be shown later on, by use of a time true solver, the existence of a stationary solution are questioned at incidences above stall except when the incidence is very high ($\alpha \sim 40^o$). By partners doing local time step computations this fact

was reported as non converged solutions and gave in general a very high lift at incidences above the measured stall incidence. Utilizing a local time stepping algorithm and the prescription of a transition position that maybe not in accordance with the real transition positions can make comparisons of turbulence models very difficult. On the other hand, when all turbulence models are applied with the same transition points and by only regarding results below or near the stall incidence at least a judgement of the turbulence models can be made on this basis and the results can be viewed in light of the measurement.

All the calculations presented in the following sections was performed on a grid provided by the *ECARP* project with every second normal grid line removed. It consist of 177 grid points around the airfoil and 64 grid points in the normal direction where the original grid contains of 353 grid points around the airfoil. The height of the boundary cells was distributed with small cell heights in the front stagnation region and larger cell heights in the trailing edge region. Computations showed that y^+ every where was below 2.5 in the boundary cells. The outer boundary was located around 11 chord length away. On Fig.(6.2) results obtained on the original grid and on the grid with every second grid line removed are shown.

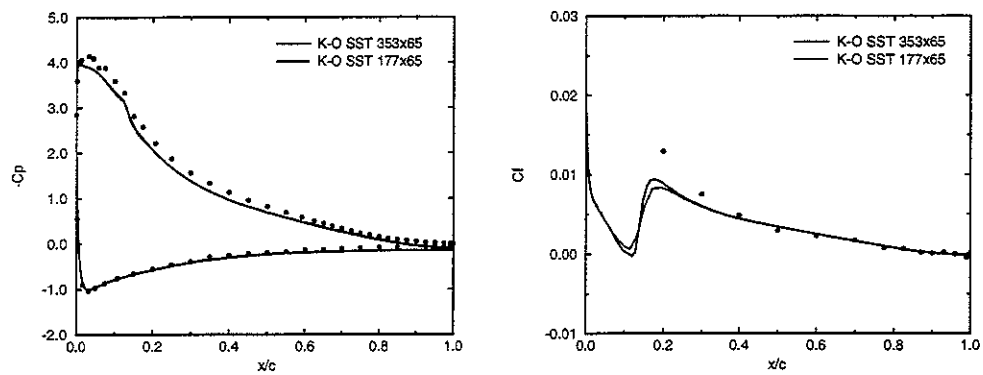

Figure 6.2: *Pressure and skin friction (upper surface) coefficient distribution on the surface of the Onera-A airfoil calculated with the $K-\omega$-SST turbulence model on two different grids. The angle of attack equal 13.3° and the Reynolds number is 2 million. Circles are experimental results from the F1 wind tunnel.*

As shown on Fig.(6.2) only small deviations occur in the solutions obtained on the two different grids and the largest deviations are found in the skin friction development close to the point of transition. One calculation on the $353x65$ grid demanded approximately 9 hours of computation time on a CRAY-C92A with an overall floating point performance of 382.4 mflops. The solution of the transport equation for γ used 583.3 mflops and the transport equations for K and ω used 560.8 mflops and the solution of the Poisson equation for ψ was done with 473.2 mflops. The very large time consumption leads to do further calculations only on the grid with $177x65$ grid points.

The results shown in the following sections are in general considered when the residual was reduced to $1 \cdot 10^{-7}$ for stationary flow situations. It was often found that the transition mechanism made further residual reduction very time consuming and was typically unnecessary when flow properties not close to the transition point was considered. Flow properties close to the point of transition exhibited a tendency to fluctuate in time with very small variations but still large enough to influence the overall residual long time after the main flow was converged. Only tiny influence from the fluctuations was found in the global coefficients such as lift and drag. In some cases, f.i. where an unsteady separation bubble is present, a residual reduction was not possible and in these cases mean values obtained after the residual reduction was stagnated are considered.

6.2 Results for the Onera-A airfoil up to incidence equal 17.6°

In this section result obtained with the various turbulence models outlined in chapter 3 section (3.3.2) to (3.3.5) will be shown for flow past the Onera-A airfoil with a Reynolds number equal 2 million and incidences equal 10.1^o, 13.3^o and 17.6^o. At the largest incidence measurement taken from the F1 wind tunnel experiments suggest lift stall to occur around $\alpha = 17.6^o$ so this incidence is interesting because stall is typically difficult to capture correctly. One special incidence, $\alpha = 13.3^o$, is treated profound and all the results are shown on Figs.(6.4) to (6.7).

Following the discussions done previously, the C_p distribution and the C_f distribution are strongly linked and should not be treated separately but basically the pressure distribution found by applying all the turbulence

models coincidence fairly well with the experimental results. The BL model is the one which produce the largest overall C_f value after transition, except at $\alpha = 17.6^o$ where wiggles occur. As Fig.(6.5) indicate the BL model needs a quite aggressive smoothing procedure, (see chapter 3 section (3.3.6)), in order to have a smooth pressure and skin friction distribution. The 1- and 2-equation turbulence models needs only a linear smoothing over a short distance, typical 3 to 4 cells, in order to produce a smooth transition.

For $\alpha = 10.1^o$ and 13.3^o the predicted pressure distribution is found to be in good accordance with the measurement as shown on Fig.(6.4) and Fig.(6.5). The most pronounced difference in the results obtained by the different turbulence models is found in the results obtained by the BB model. This model predict a lower skin friction distribution than the other models and is the only model that computed a noticeable trailing edge separation at $\alpha = 13.3^o$.

The skin friction and pressure distribution at $\alpha = 10.1^o$ and 13.3^o produced by the SA and the $K-\omega$ models is comparable, with the SA model giving nearly identical results as the $K-\omega$-BSL model. It is quite clear that the limiter introduced in the $K-\omega$-SST model gives a lower C_f value than the BSL model and provides a better agreement with the experiments. Generally it can be observed that when the skin friction is in good agreement with the experiments greater deviations occur between the measured and computed C_p distribution. Typically all the models tends to underpredict the C_f distribution in the transition region. This can be on account of the smoothing procedure and there might also be a grid-dependence as indicated on Fig.(6.2).

In Fig.(6.6) local quantities are shown for $\alpha = 13.3^0$ at x/c equal 0.5, 0.86, 0.9 and 0.96 for the U-velocity component and the principal turbulent shear-stress

$$\tau_{xy} = \overline{uv} = -\nu_t \frac{\partial U}{\partial y} \quad , \tag{6.1}$$

along a straight line orthogonal to the surface of the airfoil at the considered position. Care should be taken when conclusions are drawn because the measurement of U and τ_{xy} was only available from the F2 wind tunnel where the accuracy is considered lower than in the F1 wind tunnel. On the other hand the deviation of lift and drag from the two different set of experimental data are not very large at this incidence so the data from F2 can certainly be used.

The C_p and C_f data are from the F1 wind tunnel and especially the C_f distribution at the trailing edge indicate a smaller separation than the measured U-velocity distribution. The calculated C_f distribution is reflected in the calculated τ_{xy} distribution by the amount of back flow in the near wall region. The BB model predict local values fairly well but deviate from the measured skin friction distribution at the trailing edge. Actually the BB model is the only model which calculate a separation comparable with the F2 measurements but the normal extension of the de-attached flow is slightly underpredicted. The BL model predicts results in lowest agreement with the experiments for all the compared quantities. The SA model gives similar results to the ones obtained with the $K-\omega$-BSL model and the SST model is seen as a clear improvement to the BSL model. The $K-\omega$-SST model calculated a skin friction distribution in very good agreement with the measured skin friction but the U and τ_{xy} distribution deviate from the measurements.

On Fig.(6.7) the calculated momentum and displacement thickness are shown. A good agreement between the calculated and measured displacement thickness is found for nearly all the applied turbulence models except the BL model. Again it is seen that the results obtained with the SA model are comparable to those obtained by the $K-\omega$-BSL model. When comparing the calculated momentum thickness large deviations occur between the calculations and the measurements for $x/c > 0.7$ at the upper surface. The large deviation seem as in dis-order with the calculated velocity profiles at least for the BB model. Closely inspection of the measured velocities shows a lower boundary layer thickness than the calculated. As the momentum thickness is more sensitive to the boundary layer thickness than the displacement thickness due to the squared velocity a large deviation will be expected when the boundary layer thickness does not correspond to each other.

At $\alpha = 17.6^{o}$ all models predicts leading edge separation as shown on Fig.(6.5). The BB model predicts a very little leading edge separation and a large trailing edge separation. The convergence history showed a stagnation in residual reduction and occurrency of spikes of large residuals. These spikes of large residuals are believed to originate from the boundary condition for R_t at the airfoil. The flow was only temporary altered due to this instability. The SA and the $K-\omega$-BSL/SST turbulence models predicts a larger leading edge separation than the BB model but a smaller trailing edge separation. The results obtained with the BL model is regarded as being in error due to the wiggles in the leading edge region. The $K-\omega$-BSL model calculated a

nearly steady flow where the unsteadyness originated from a tiny pulsation of the leading edge separation. The two 1-equation turbulence models predicts a strong suction peak close the leading edge which makes the lift coefficient large. The suction peak found by the $K-\omega$ models coincidence better with the experiment and the lift coefficient is by this found to be in better agreement with experiments.

In table (6.2) lift and drag coefficients are listed for the computed flow past the Onera-A airfoil. By comparing the calculated results with experiments a general good agreement is found for the results obtained by the $K-\omega$-SST model in the predicted lift with a tendency to under estimate the lift coefficients for α equal 10.1^o and 13.3^o and a tendency to over estimate the lift coefficient for α equal 17.6. In general large variations between measured and calculated drag coefficients are found. The drag coefficient which is as important as the lift is in general more difficult to calculate due the large dependence of the pressure distribution on the drag coefficient.

6.2.1 Transition considerations

The Michel transition criterion was utilized for examining the hypothesis that the upper transition point was located at $x/c = 0.12$. In the calculations the transition point at the lower surface was kept fixed at $x/c = 0.3$. The calculations was performed with the $K-\omega$-SST model. Three calculations was performed at incidences equal $\alpha = 6^o$, 8^o and 10.1^o. For these three incidences the Michel criterion predicts the upper side transition point at the positions shown in the table (6.1).

C_l and transition positions				
α	x/c	$C_{l,Michel}$	$C_{l,0.12}$	$C_{l,F1}$
6.0^o	0.16	0.81	0.80	0.88
8.0^o	0.12	1.00	1.00	1.09
10.1^o	0.11	1.20	1.21	1.30

Table 6.1: *Transition positions predicted at the upper side of the Onera-A airfoil with the Michel criterion. Subscript Michel indicate values obtained with the transition position predicted by the Michel criterion,* 0.12 *indicate transition at* $x/c = 012$ *at the upper surface and F1 is experimental data from wind tunnel F1.*

The transition points shown in table (6.1) correspond well with the experimental estimated position $x/c = 0.12$, at least for incidences 8^o and 10.1^o. At lower incidences the Michel criterion indicate a transition point located further downstream. The predicted lift is seen to be virtually independent of the location of the transition point.

At higher angles of attack no stationary transition point was found with the Michel criterion due to a part time presence of a leading edge separation bubble. As the Michel criterion in the beginning of a calculation predicts a transition point close to the ones at lower incidences a leading edge separation bubble builds up in front of the transition point. As the leading edge separation bubble builds up a programmed logic will put the transition point ahead of the separation bubble [1]. When the transition point is located in front of the bubble eddy-viscosity will be produced behind the transition point and the downstream flow will re-attach. When the separation bubble no longer is present the Michel criterion will find the same early stage transition point and the leading edge bubble will appear again. This unsteady motion will continue through out the calculation.

In the previous section it was postulated that the origin of transition process was a leading edge separation for most angles of attack. All the computations performed in this sub-section gives no indication on the presence of a leading edge separation bubble for incidences lower than 10.1^o. On the other hand the calculation performed on the grid consisting of $353x65$ grid points shown on Fig.(6.2) indicate a small leading edge separation which was not captured on the $177x65$ grid. If there exist such a grid dependence also at lower incidences the Michel criterion can not be utilized for the flow past the Onera-A airfoil but then it must believed that the transition process originate from the presence of a leading edge bubble.

6.3 Results for the Onera-A airfoil at incidences higher than 17.6°

In this section the BL, BB and the $K-\omega$ turbulence models will be applied to an instantaneous start of the Onera-A airfoil. The incidences considered are 25^o and 40^o which are incidences where the flow is fully separated.

[1] The Michel criterion is only valid for attached flow, see chapter 3 section (3.3.6).

At an incidence of 25.0^o the flow is fully separated. The lift history for the impulsive start of the Onera-A airfoil is depicted on Fig.(6.8). Due to the facts that none of the models would accepts the high gradients present in the very beginning of the flow, all the calculation has been initiated by first invoking the turbulence model after 0.125 dimensionless seconds. In this flow onset period the lift which initially was very high is decreased to a low value.

The only model that predicts a stationary flow for $\alpha = 25^o$ is the BB model. The BB, BL and the $K-\omega$-SST models predicts the same pattern in the stall onset phase. All three models computes an increase in lift with a peak just before onset of stall. After onset of stall the lift drop to a low value and recovers to a nearly constant value almost equal for all the applied turbulence models. Closely inspection shows nearly the same peak-valley pattern for the BL model and $K-\omega$-SST model. The result obtained with $K-\omega$-BSL model deviate in the sense that no peak and valley pattern is observed in the stall onset phase.

At very high incidence, $\alpha = 40^o$, all the utilized transport models gave nearly identical results as shown on Fig.(6.8). The evolution of C_l is sinusoidal with a decreasing amplitude ending with a stationary solution after approximately $t = 40$. The algebraic BL model gave the same start-up motion as the transport models but the value of C_l continuously oscillate with a constant frequency and with same amplitude every second period.

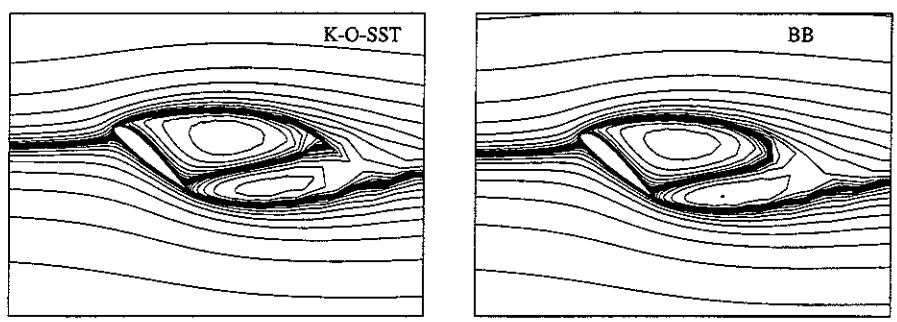

Figure 6.3: *Flow past an Onera-A airfoil at 40^o of incidence calculated with the $K-\omega$-SST (left) and the BB (right) turbulence model.*

On Fig.(6.3) the streamlines obtained by applying the BB and the $K-\omega$-SST turbulence models for the flow with the incidence of 40^o are shown. As the figure indicate only limited variations are found in the flow. It is

interesting to observe that the flow at high incidence is nearly independent of the utilized turbulence model. The reason why all transport models gives similar results at high incidences is proberly found in the use of a time true solver combined with a transport process of the turbulent quantities. When the solver correctly models the larger structures of the flow the influence of the eddy-viscosity will mainly be in dissipation of turbulent kinetic energy in the small scale range and the formulation is then close to an large eddy formulation.

The Spalart-Allmaras model could not be applied to the impulsive start case with $\alpha = 25^o$ and $\alpha = 40^o$. The growth rate of eddy-viscosity is low and the flow creates structures forcing the model to predict large negative eddy-viscosities.

6.4 Summary

The flow past an Onera-A airfoil has been calculated by utilizing turbulence models varying from algebraic to 2-equations turbulence models. It was found that the BB model predicts results in good agreement with experimental results at an incidence equal 13.3^o. The SA and the $K-\omega$-BSL models predicts results comparable to each others. The $K-\omega$-SST model predict the flow in overall best agreement with the experiments and the predicted skin friction distribution is in very good agreement with the measurements. The $K-\omega$ turbulence models was the most robust turbulence models relative to the other models.

The transition point was predicted by the Michel criterion for incidences equal 6^o, 8.0^o and 10.1^o. A good agreement was found with an experimental estimated transition point at the incidences 8.0^o and 10.1^o.

At high incidences, $\alpha = 25^o$, the influence from applying different turbulence models begins to vanish. Quite similar development of lift in time was found by applying different turbulence models. At very high incidence $\alpha = 40^o$ all transport turbulence models gave nearly identical solutions and the algebraic BL model predicted an unsteady motion with sinusoidal lift variation in time.

Lift coefficients C_l						
α	BL	BB	SA	$K-\omega$-BSL	$K-\omega$-SST	F1
10.1	1.24	1.20	1.22	1.19	1.21	1.30
13.3	1.52	1.49	1.51	1.50	1.49	1.57
17.6	$\overline{1.87}$	1.81	1.80	$\overline{1.82}$	1.76	1.66
25.0	$\overline{0.75}$	0.81	-	$\overline{0.88}$	$\overline{0.95}$	-
40.0	$\overline{0.90}$	0.75	-	0.71	0.71	-

Max/min lift coefficients C_l				
α	BL	$K-\omega$-BSL	$K-\omega$-SST	F1
17.6	1.90/1.86	1.83/1.80	-	1.66
25.0	1.01/0.64	1.03/0.74	1.17/0.77	-
40.0	1.41/0.43	-	-	-

Drag coefficients C_d						
α	BL	BB	SA	$K-\omega$-BSL	$K-\omega$ -SST	F1
10.1	0.007	0.008	0.017	0.009	0.017	0.015
13.3	0.029	0.019	0.018	0.022	0.020	0.021
17.6	$\overline{0.053}$	0.045	0.049	$\overline{0.065}$	0.065	-
25.0	$\overline{0.247}$	0.315	-	$\overline{0.262}$	$\overline{0.223}$	-
40.0	$\overline{0.835}$	0.617	-	0.616	0.610	-

Max/min drag coefficients C_d				
α	BL	$K-\omega$-BSL	$K-\omega$-SST	F1
17.6	0.065/0.037	0.070/0.060	-	0.021
25.0	0.323/0.166	0.333/0.178	0.312/0.157	-
40.0	1.191/0.570	-	-	-

Table 6.2: Lift and drag coefficients for the Onera-A airfoil obtained with the various turbulence models. An overline denotes a mean value for a non-stationary solution and a '-' denotes that no solution was obtained or no data was available. In the tables with headings Max/min maximum and minimum values are shown for the non-stationary solutions.

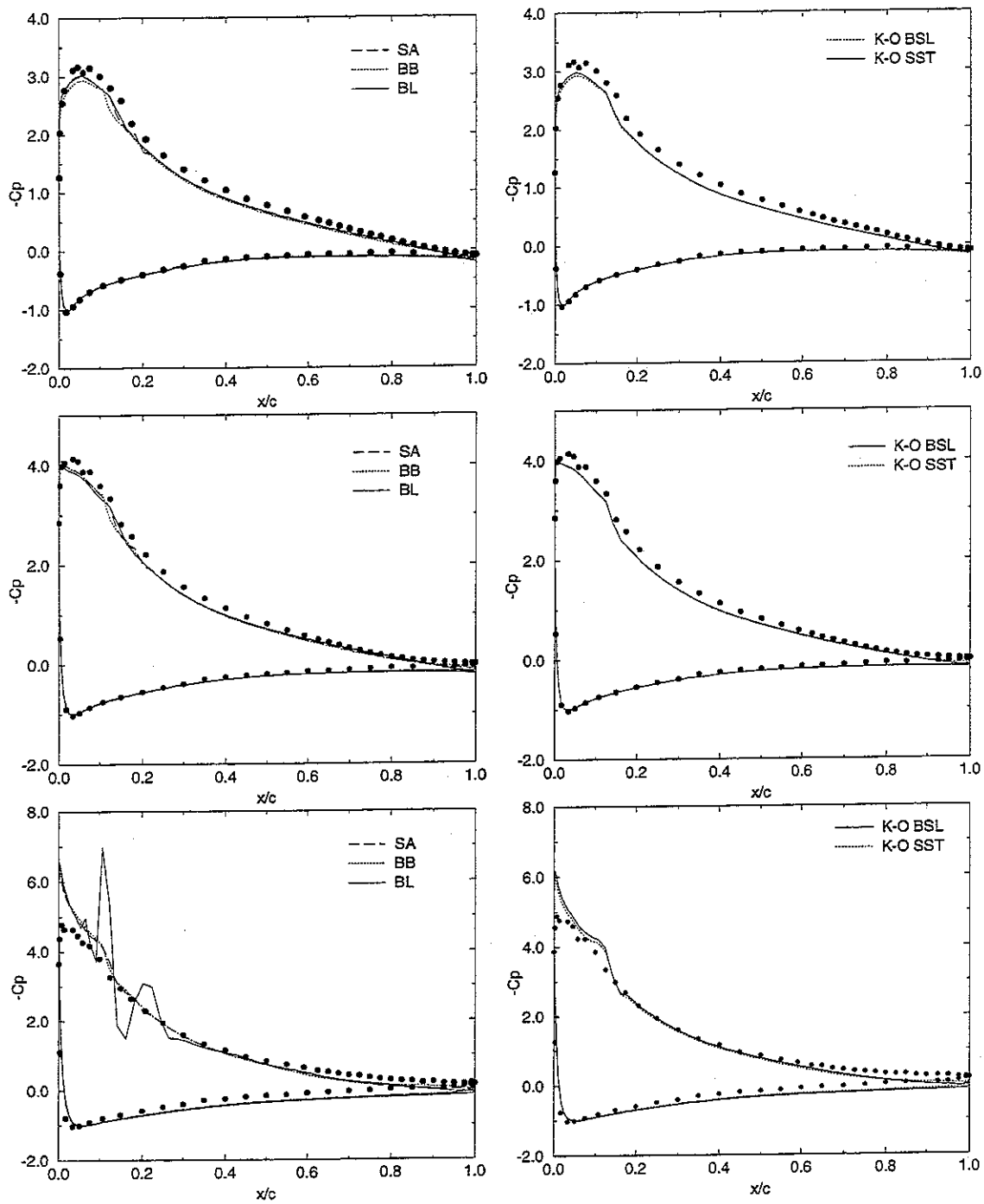

Figure 6.4: *Surface pressure distribution on an Onera-A airfoil. Upper row:* $\alpha = 10.1°$. *Middle row:* $\alpha = 10.1°$. *Lower row:* $\alpha = 17.6°$. *Circles are experimental results from the F1 wind tunnel.*

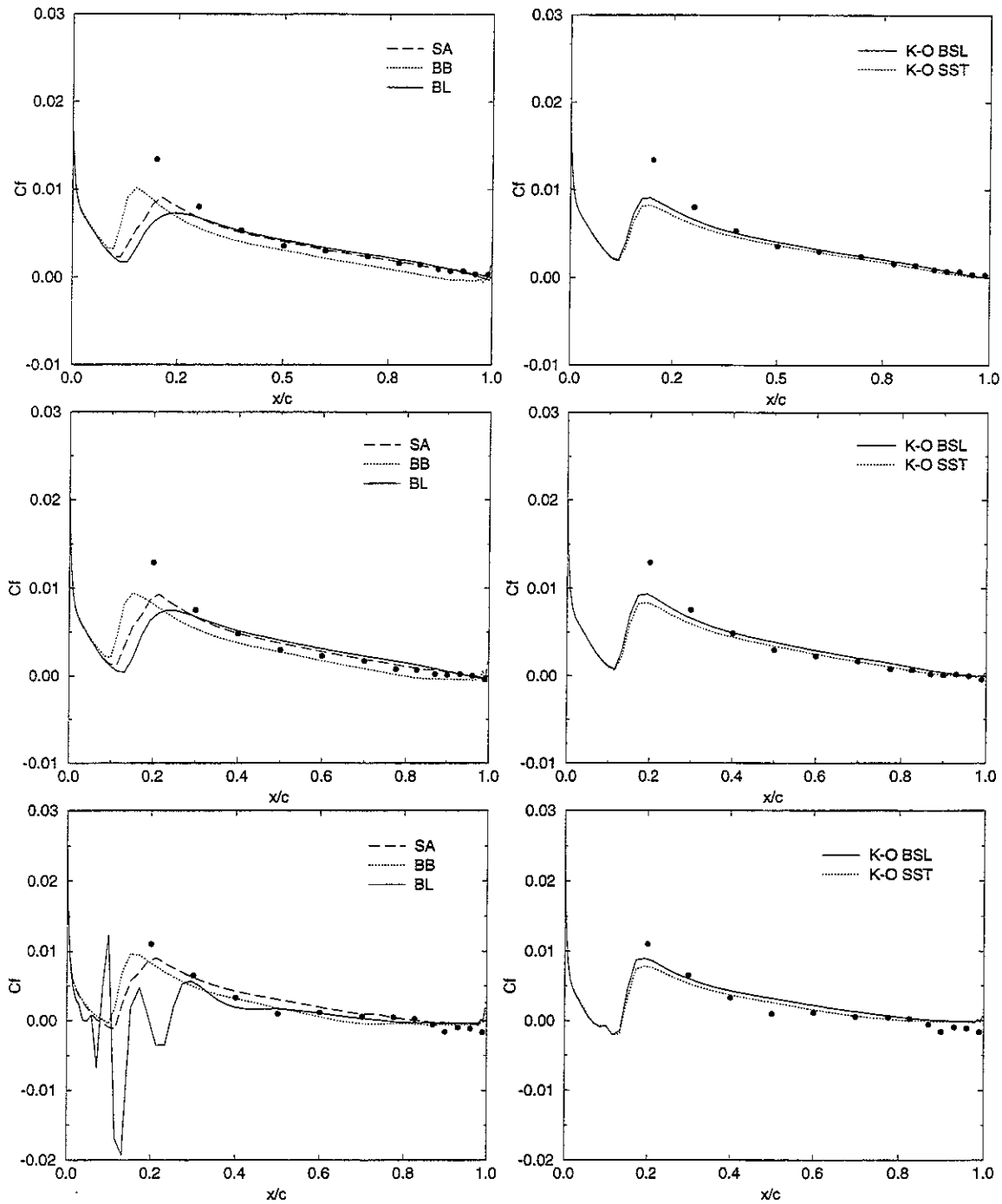

Figure 6.5: *Skin friction distribution on the upper surface of an Onera-A airfoil. Upper row:* $\alpha = 10.1^o$. *Middle row:* $\alpha = 10.1^o$. *Lower row:* $\alpha = 17.6^o$. *Circles are experimental results from the F1 wind tunnel.*

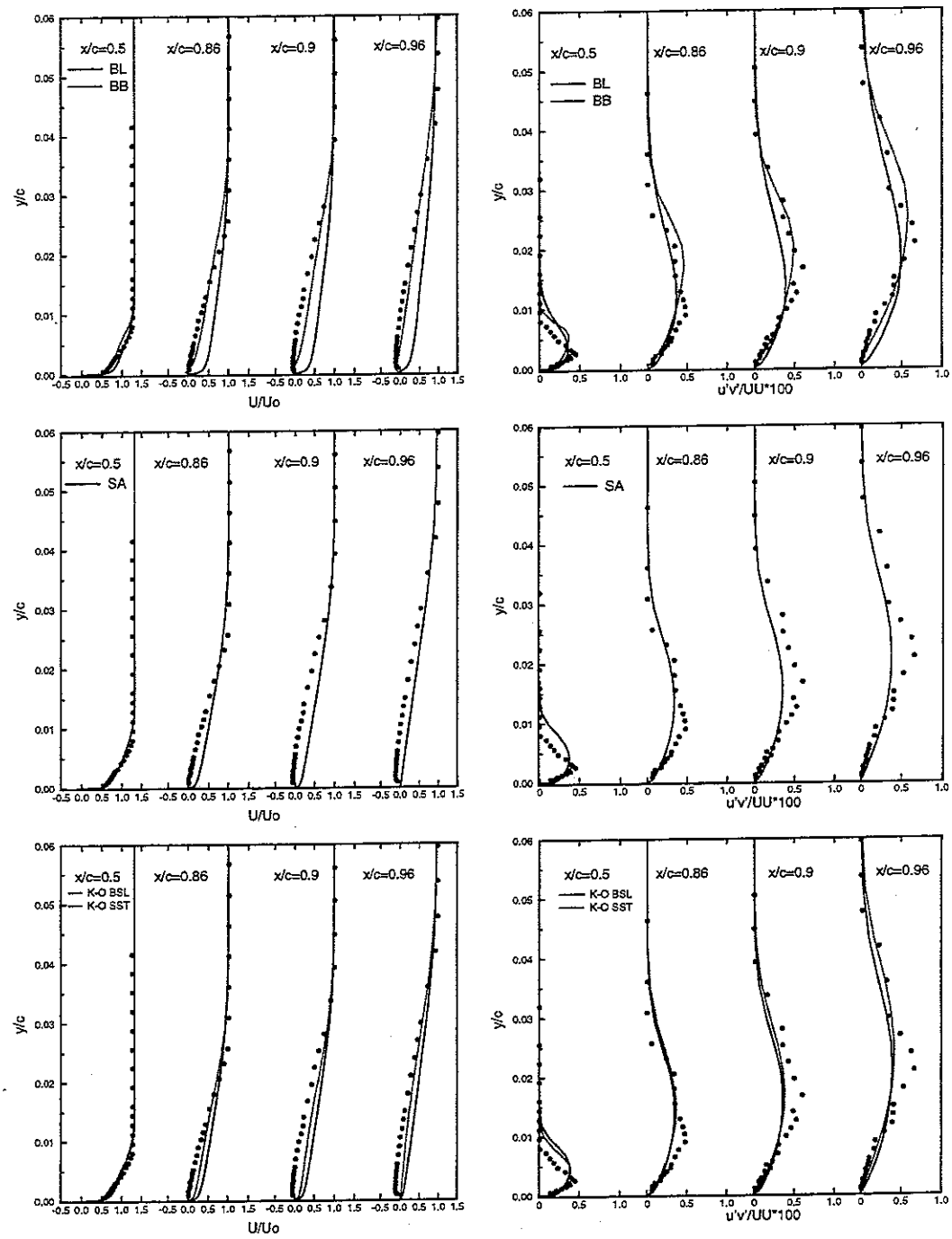

Figure 6.6: *Mean velocity and shear stress profile calculated with the BL, BB, SA and $K-\omega$-BSL/SST turbulence models. The angle of attack equals 13.3° and the Reynolds number is 2 million. Circles are experimental results from the F2 wind tunnel.*

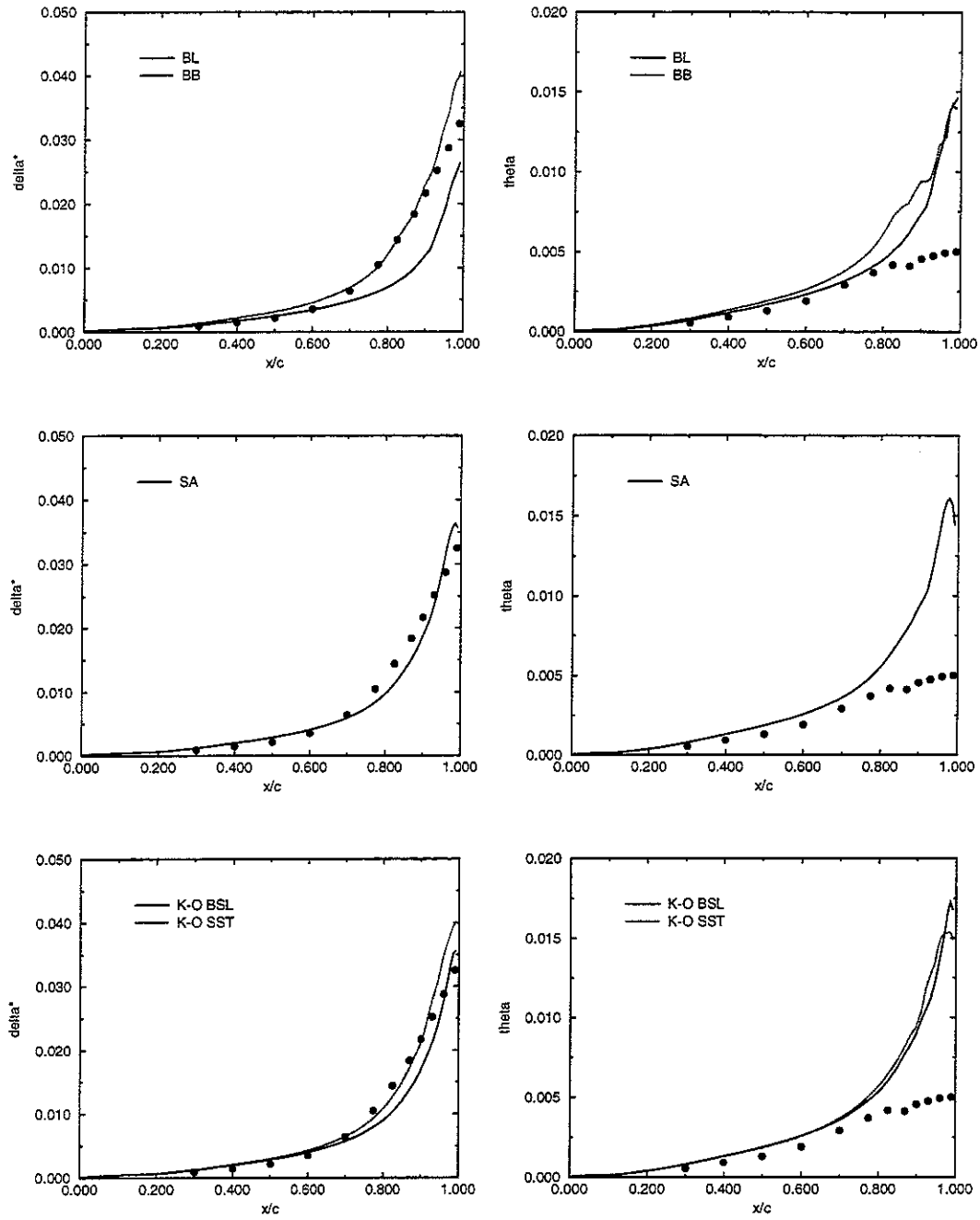

Figure 6.7: *Displacement and momentum thickness calculated with the BL, BB, SA and $K-\omega$-BSL/SST turbulence models. The angle of attack equals 13.3° and the Reynolds number is 2 million. Circles are experimental results from the F2 wind tunnel.*

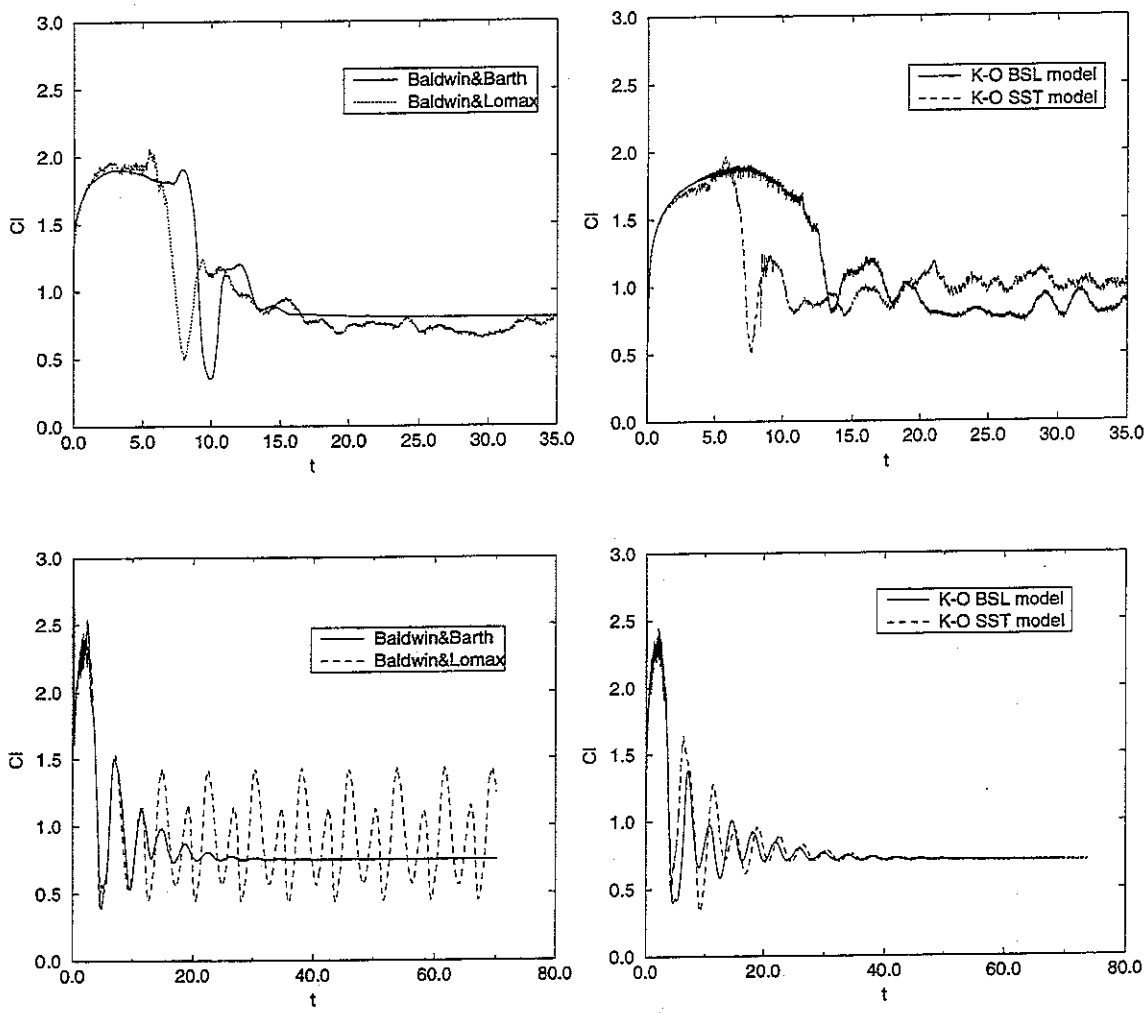

Figure 6.8: *Lift time history for a instantaneous start of a Onera-A airfoil at an angle of attack equal 25° (upper row) and 40° (lower row). The flow is calculated by utilizing the Bl, BB, and the $K-\omega$ turbulence models.*

Chapter 7

Turbulent flow past an airfoil oscillating in pitch

In this section turbulent flow past an airfoil oscillating in pitch will be presented. The flow is calculated by the vorticity-streamfunction formulation of the Navier-Stokes equations outlined in the previous chapters. The flow to be considered is a light and deep stall flow situation for a NACA 0015 airfoil. Before presenting the results a general discussion of the phenomenon dynamic stall will done.

7.1 General description of dynamic stall

As mentioned in the introduction oscillatory airfoil flows is linked to phenomenon called dynamic stall, which is a subject of large interest due to the unsteady loads of e.g. helicopter rotors. The term dynamic stall refers to the unsteady separation on an airfoil subject to a forced movement typically of sinusoidal form where the lift-stall is significant different from static stall. Generally three distinct dynamical flow situation is considered, stall onset, a light stall and deep stall case [29], [28] [27]. A typical development of lift, moment and drag as a function of incidence for the three basic dynamic stall situations are shown on Fig.(7.1).

Stall onset is considered where the maximum incidence is equal or below the static lift-stall angle. The hysteresis loop is narrow and a tendency to overshoot the static lift is found at down-stroke. The flow is typically unseparated through out the rotation and the tendency to overshoot the static

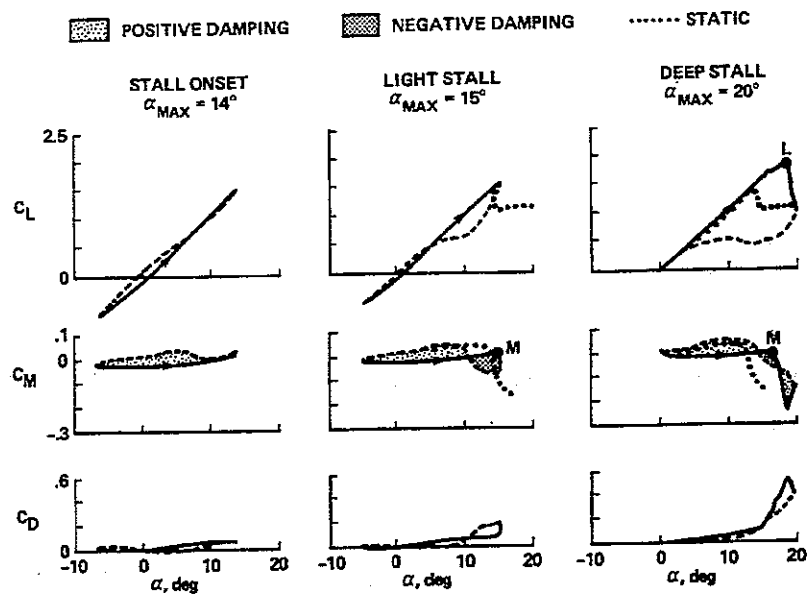

Figure 7.1: *Unsteady forces and moments in three dynamic-stall regimes:* $M_0 = 0.3$, $\alpha = \alpha_0 + 10°cost(2 \cdot k \cdot t)$, $k = 0.1$. *Capital M refers to moment-stall and L to lift-stall. From [29].*

lift counterparts is due to a time lag for the development of the boundary layer. The development of the boundary layer is typically slower than the corresponding movement of the airfoil.

The light stall case is considered when the maximum incidence in the pitching motion is higher than the static lift-stall angle. In this case the hysteresis curve mostly shows concave form at the up-stroke motion. The maximum lift found at the up-stroke can greatly exceed the static counterpart, but the actual evolution of lift, moment and drag at the up-stoke is greatly influenced by the reduced frequency as shown on Fig.(7.2). That the maximum lift encountered at the up-stroke motion exceed the static ones is again partly described by the time lag for developing the separation and by flow realizations described below for the deep stall case.

The deep stall case is considered when the maximum incidence greatly exceed the the static lift-stall incidence. After passing the static stall incidence, lift continuously increases until and abrupt and strong lift-stall occur. The deep stall case is considered as being viscous dominated and the existence of

a vortex like structured formed between the static stall incidence and maximum incidence at up stroke in the leading edge region is supposed to play a dominant role [30], [6]. As the static stall incidence is reached the boundary layer separate in the trailing edge region and soon after an attached vortex is formed near the leading edge. The formation of a vortex like structure in the leading edge region is believed to originate from a concentration of vorticity, due to different time scales for generation and transport of vorticity, which suddenly erupt.

Ones the vortex is formed the pressure in the leading edge region will decrease fast and as the vortex de-attaches the surface and is passing the airfoil in the oncoming flow direction the overall static pressure on the suction side will decrease and lift is increased. By this process the high lift is no longer generated by the pressure peak in the leading edge region as in the static case with trailing edge separation but by the over all low pressure along the airfoils suction side.

As the pressure peak is no longer present in the leading edge region the pressure drag will decrease and can even change orientation. The moment will in the same time change dramatically due to another distribution of pressure mainly at the upper surface. When the vortex passes the trailing edge the lift can no longer be held at a high level and the dynamic lift-stall occur. The extension of the separation area is in the order of the chord length and even though the incidence is decreasing the time scale for reattachment are long so the static lift is, if ever realized at down-stroke, postponed long after the static lift-stall incidence is reached.

The unsteady forces shown on Fig.(7.1) are some how idealized cases. The flow development is strongly influenced by a number of parameters where the ones with largest impact on the flow is the maximum incidence α_{max}, the reduced frequency k, and the geometry of the airfoil (mainly the leading edge) [31]. If the Reynolds number are high enough $> 1.5 \cdot 10^6$ normally no Reynolds number effect are found. On Fig.(7.2) the effects of varying the reduced frequency are shown for the deep stall case.

The dynamic stall case is divided into two stall mechanism named, by the nature of separation, as leading edge or trailing edge stall. The airfoil shape has the largest influence in the light stall case. On an airfoil with a blunt nose separation is typically initiated by a trailing edge separation which is spread upstream as the incidence is increased. The pressure in the leading edge region will, for airfoils with trailing edge separation, still be high enough to compensate for the looses in the trailing edge region. Airfoils with moderate

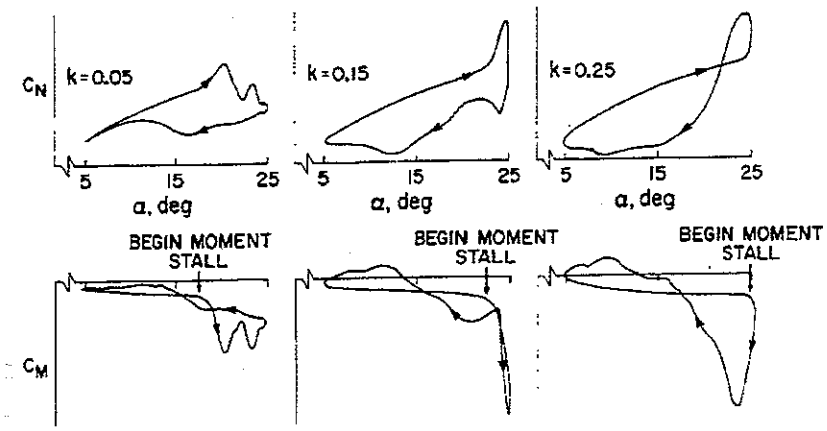

Figure 7.2: *Variation of normal force and pitching moment with reduced frequency for a NACA 0012. From [31].*

sharp leading edges has a tendency to produce leading edge separation before trailing edge separation. This leading edge separation spreads rapidly in the downstream direction. This process produce a relative strong vortex which makes the changes in the aerodynamic coefficients occur more fast than for a trailing edge separating airfoil.

Dynamic stall is typically computed by two different strategies when the full Navier-Stokes equations are considered. In one strategy the Navier-Stokes equations are solved in an inertial frame of reference and for each time step a new grid is calculated [15] [25]. This method is preferable when the non-inertial terms gives rise to numerical instabilities in the chosen integration and discretization scheme. Another method, which is similar to the present method, is to solve the Navier-Stokes equations in the rotating frame of reference an include the terms arising from the non-inertial coordinate system.

7.2 Numerical setup for calculation of dynamic stall

In the following two sections the vorticity-streamfunction Navier-Stokes solver with the turbulence models outlined in Chapter 3 will be applied to two oscil-

lating airfoil flow, one which is considered as light-stall and another considered as a deep-stall case. Results are compared with measurement [16]. The grid utilized for the calculations consist of 382 grid points around the airfoil and wake with 64 points in the wake. 65 grid points was distributed between the airfoil and outer boundary with a distance to the grid point next to the wall of $3 \cdot 10^{-5}$. The outer boundary was located 12 chord lengths away.

The BB and $K-\omega$ models was calculated by utilizing a time-step of $2.5 \cdot 10^{-3}$ and due to stability problems with the SA model a time-step of $1.5 \cdot 10^{-3}$ was utilized. Further more the $f_w(r)$ function in the SA model was put equal to one due to the very unstable behavior of the argument r. This is of course a violation of the Spalart-Allmaras turbulence model where the destruction term was designed to vanish in the outer part of the boundary layer. On the other hand the $f_w(r)$ function is supposed to be equal to one in the major part of the boundary layer and deviate slightly from one in the laminar sub-layer in case of a strong pressure gradient. The analysis done by Spalart and Allmaras leading to f_w are based on attached boundary layer flow in order to produce a log-layer and a calculation performed for flow past a flat plate with $f_w = 1$ showed that the additive constant B in the law of the wall is altered to a higher value.

7.3 Dynamic light stall airfoil flows

The flow considered in this section is a turbulent flow past a NACA 0015 with a mean angle of attack $\overline{\alpha} = 11.37$ and with an amplitude of the oscillations $\Delta\alpha = 7.55$. The Reynolds number is 1.5 million and the reduced frequency equals $k = 0.102$.

On Fig.(7.3) to Fig.(7.7) C_n, C_t and C_m are shown. The values are taken from the second cycle but only very small variations are found from the first to the next cycles. Oscillations was initiated after 7 non-dimensionalized seconds. Observations found with different flow situations at onset of oscillations showed that no changes was found from utilizing a fully converged solution or a solution obtained after 7 non-dimensionalized seconds.

For the 1-equations turbulence models BB and SA a general good agreement are found with the measurement as shown on Fig.(7.4) and Fig.(7.5). The BB model over estimate lift at up-stroke whereas the SA model make a under estimate of the lift at up-stroke. At down-stroke the agreement with measurement are similar quite good for the BB and SA models, with the BB

model tending to over predict lift for incidence higher than $\alpha \sim 15^o \downarrow$ caused by a to slowly separation process. The moment are by the one-equations turbulence models predicted in good agreement with the measurement at up-stroke and down-stroke, except just after maximum incidence. The drag are similar in quite good agreement with the measurements. As both lift, drag and moment are predicted in good agreement with the measurement it is believed that some of the flow realizations typical for dynamic stall are captured by the calculations.

On Fig.(7.8) instantaneous streamlines are shown for the flow calculated by the Spalart-Allmaras model. In general the separation pattern is comparable to static flow situations at up-stroke. This was some how expected due to the low reduced frequency. As the incidence increases a separation is formed at the trailing edge which is first noticed around $\alpha = 13.3^o \uparrow$, Fig.(7.8.c). This separation bubble becomes bigger as the incidence increases and a counter rotating vortex is formed closed to the trailing edge, Fig(7.8.f). Passing maximum incidence the separation continuously becomes bigger even though the incidence is becoming smaller. This is explained by the time lag between the development of the boundary layer and the pitching motion of the airfoil.

Around $\alpha = 14.6^o \downarrow$ Fig.(7.8.h) the reattachment process has started and continue until $\alpha \sim 10^o \downarrow$. At this incidence the lift has not regained the static counter part due to the time needed for building up the boundary layer. From $\alpha \sim 10^o \downarrow$ an until minimum incidence very little lift variations are found. In this region of incidence the boundary layer is developing towards the static counter part at minimum incidence. At minimum incidence the lift is comparable with the static one and equals the realization of the beginning of the second cycle.

The very high lift calculated by the $K-\omega$-SST model around maximum indence, Fig.(7.7), is on account of a formation of two very strong vortices in the leading edge region and one strong vortex in the trailing edge region. The presence of an attached vortex in the leading edge reading is felt as an thickening of the airfoil and raise the pressure in this region. In this situation the flow is clearly an un-physical realization and an investigation of the flow gave no indication of how to remedy the problem or alter the turbulence model.

The $K-\omega$-BSL model produces result which again must be considered as un-physical. The model gave only limited separation close to maximum incidence followed by a rapid attachment of the flow producing a high lift at

down-stroke.

The flow situation calculated by the BL model is characterized by very little separation in the trailing edge region. (Please notice that the loop is counter clock vice). This was some how expected because the BL models normally has difficulties in predicting separation close to the static stall incidence.

7.4 Dynamic deep stall airfoil flows

The flow to be considered is a turbulent flow past a NACA 0015 with a mean angle of attack $\overline{\alpha} = 19.58$ and with an amplitude of the oscillations $\Delta\alpha = 6.83$. The Reynolds number is 1.5 million and the reduced frequency equals $k = 0.154$.

Global variables, C_n, C_t and C_m, obtained in the second cycle after oscillations was initiated, are shown on Figs.(7.3) to (7.7) for the flow calculated with the various turbulence models outlined in chapter 3. Oscillations was initiated after 2 non-dimensionalized seconds. Only limited influence was found in the first hysteresis loop due to the initial solution and the influence was disappeared when entering the second cycle.

Quite large deviations occur from the first to the second cycle but after the second cycle only small changes was found in the cycles. In general deviations occur between the calculated results and measured values in the second. cycle but it is believed that some major features of the flow is captured well with the BB, SA and $K-\omega$-SST models and to some extend also the $K-\omega$-BSL model. The BB and SA model predicts fairly well the incidence where the lift begins to increase rapidly close to maximum incidence and the strong diminution of lift at maximum incidence. The $K-\omega$-SST model calculate a to early lift-raise. Similar all three models, (BB, SA and $K-\omega$-SST), correctly predicts an increase in lift at down-stroke just after maximum incidence. Close to maximum incidence very strong variations occur. As the angular velocity goes to zero the lift begins to decrease and close to the point where the angular velocity begins to increase a sudden lift increase is encountered followed by a rapid decrease.

The measurement suggest a lift plateau at an incidence around 22.5^o for both up- and down-stroke movement. None of the models capture this plateau and the lift raise is for all models seen as an pure increase with no tendency to a level off, around an incidence of 22.5^o. In general the S-shape of

the up-stroke part of the hysteresis curve is not captured by any of the utilized turbulence models. Maybe some of the explanation of why the S-shape is not captured by any of the utilized turbulence models should be found in the flow at minimum incidence. Here all models does not calculate the path of lift-recovery to a value close to the static ones at minimum incidence. In general the up-stroke part calculated with the BB, SA and $K-\omega$-SST models look similar with a different off-set.

A good agreement with measurement is found for the drag coefficient calculated with the SA and BB model. The to soon up-stroke lift raise predicted by the $K-\omega$-SST model produce a clear impact on the drag coefficient as seen on Fig.(7.7). The early increase in lift makes C_t decreasing and is due to a to early generation of a strong vortex in the leading edge region.

On Fig.(7.9) instantaneous streamlines for the flow calculated in the second cycle by the Baldwin-Barth model is shown [1]. As the pictures indicates quite large variation with massive separation occur in this flow situation. The separation is initiated by a trailing edge separation, *1*, clearly seen at $\alpha = 23.2^o \uparrow$ on Fig.(7.9.a). The flow in the leading edge region is still attached an a high pressure peak can be maintained so the lift is still high. Around $\alpha = 25.4^o \uparrow$ Fig.(7.9.c) a flow situation with nearly maximum lift is found. The flow pattern is felt as a thickening of the airfoil where the leading edge pressure peak no longer is present but the large and elongated separation bubble lower the static pressure overall on the airfoils upper surface. This makes the pressure drag decreasing fast as seen on Fig.(7.4). At $\alpha = 26.1^o \uparrow$ Fig.(7.9.d) a very strong vortex is formed, *2*, in the leading edge region. As the strong vortex in the leading edge region quickly becomes bigger and moves further downstream the lift can no longer be held at a high level and decreases fast.

Just after maximum incidence a sudden lift raise is encountered followed by a decreasing lift situation. The situation is characterized by the enlargement of a trailing edge vortex *3* as seen on Fig.(7.9.f). The lift continuously decreases until the leading edge vortex, *2*, created before maximum incidence and the trailing edge vortex ,*3*, created around maximum incidence, has entered the wake flow. After that, the flow at the trailing edge is attached and an increasing lift situation is encountered at $\alpha = 25.2^o \downarrow$ Fig.(7.9.h). The

[1] The same reference methods as used in chapter 5 is applied when discussing structures in the flow.

flow is separated in the leading edge region and this separation *4* is expanding mainly in the downstream direction as seen on Fig.(7.9.h to i). When the separation expands into the wake around $\alpha \sim 24.5^o \downarrow$ the lift is no longer maintained at a high level.

The flow evolution from $\alpha = 24.2^o \downarrow$ and back to the initial situation of the hysteresis loop are more calm. The flow is govern by expansion and shedding of a trailing edge separation, *5* on Fig(7.9.j), and the shedding of the large elongated vortex, *4*, formed at $\alpha \sim 25^0 \downarrow$ making the flow to re-attach from the front part of the airfoil.

7.5 Summary

Two different dynamic stall situations, a light and deep stall case, has been computed by applying the BL, BB, SA, and $K-\omega$-BSL/SST turbulence models. The 1-equation turbulence models BB and SA gave results for both the light and deep stall case in good agreement with experimental data. The algebraic BL turbulence model failed to produce results in vicinity of the experiments. The $K-\omega$-SST model gave fairly good results for the deep stall case but gave results which did not gets close to experiments near maximum incidence in the light stall case. The $K-\omega$-BSL predicted some general features of the flow for the deep stall case but fail to produce a separation large enough in the light stall case.

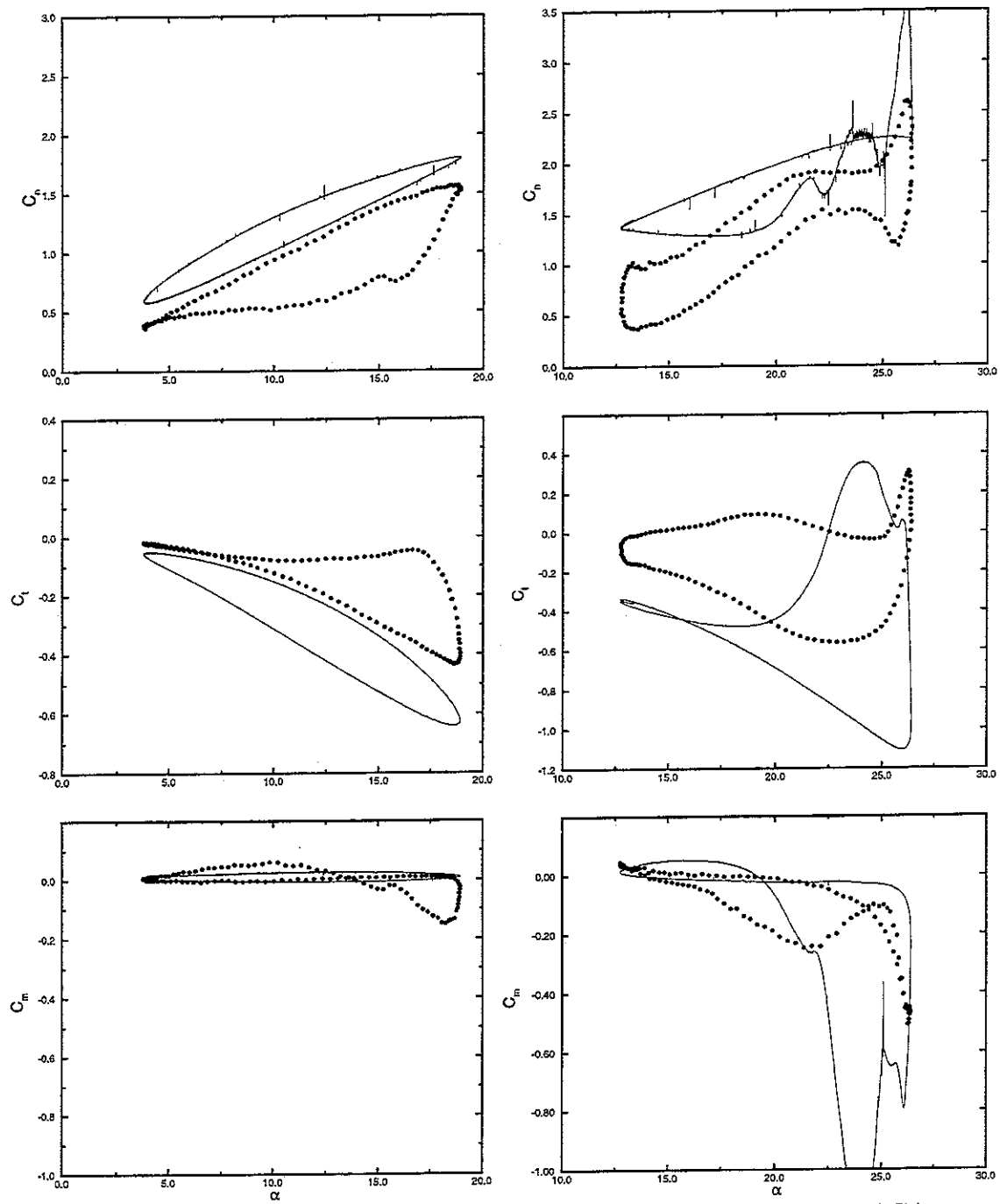

Figure 7.3: *Hysteresis curves for C_n, C_t, C_m for turbulent flow past a NACA 0015 airfoil calculated with the Baldwin-Lomax turbulence model. Left :* $k = 0.102$, $\overline{\alpha} = 11.37^o$, $\Delta\alpha = 7.55^o$. *Right:* $k = 0.154$, $\overline{\alpha} = 19.58^o$, $\Delta\alpha = 6.83^o$. *Maiximum lift is* $C_n = 3.62$ *and minimum moment is* $C_m = -1.15$.

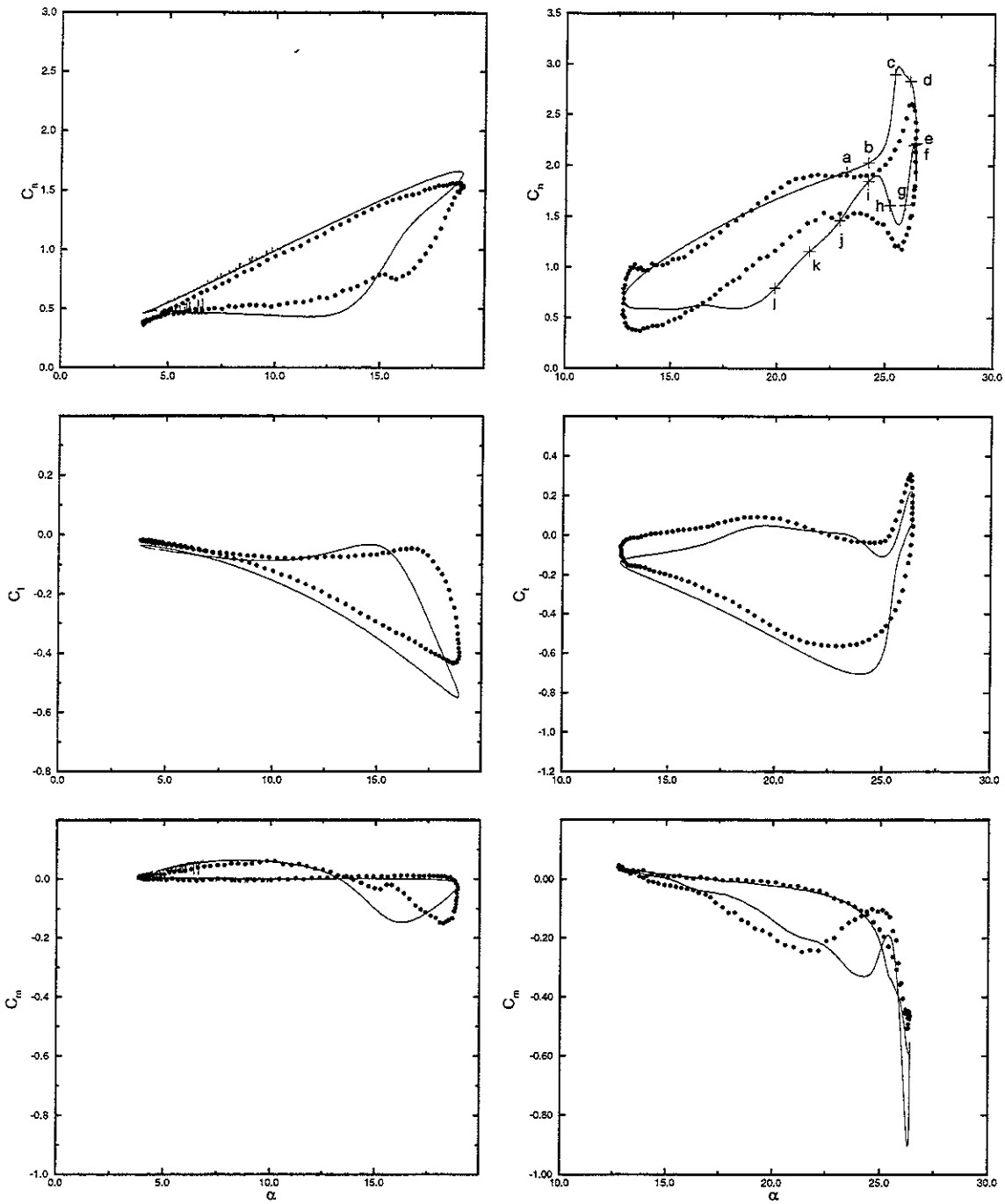

Figure 7.4: *Hysteresis curves for C_n, C_t, C_m for turbulent flow past a NACA 0015 airfoil calculated with the Baldwin-Barth turbulence model. Left:* $k = 0.102$, $\overline{\alpha} = 11.37^o$, $\Delta\alpha = 7.55^o$. *Right:* $k = 0.154$, $\overline{\alpha} = 19.58^o$, $\Delta\alpha = 6.83^o$. *(The letters and marks are refering to Fig.(7.9)).*

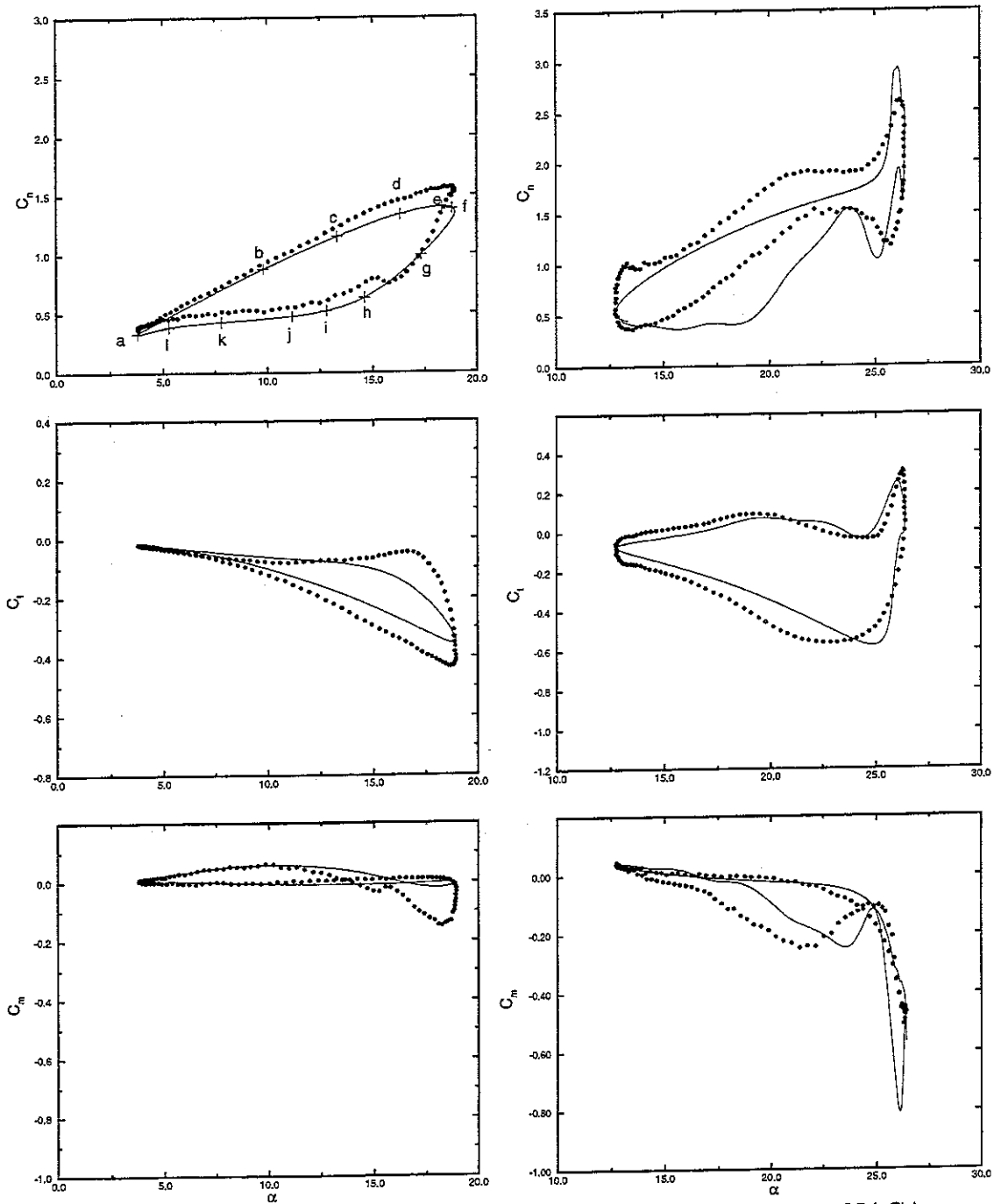

Figure 7.5: *Hysteresis curves for C_n, C_t, C_m for turbulent flow past a NACA 0015 airfoil calculated with the Spalart-Allmaras turbulence model. Left:* $k = 0.102$, $\overline{\alpha} = 11.37^o$, $\Delta\alpha = 7.55^o$. *Right:* $k = 0.154$, $\overline{\alpha} = 19.58^o$, $\Delta\alpha = 6.83^o$.*(The letters and marks are refering to Fig.(7.8)).*

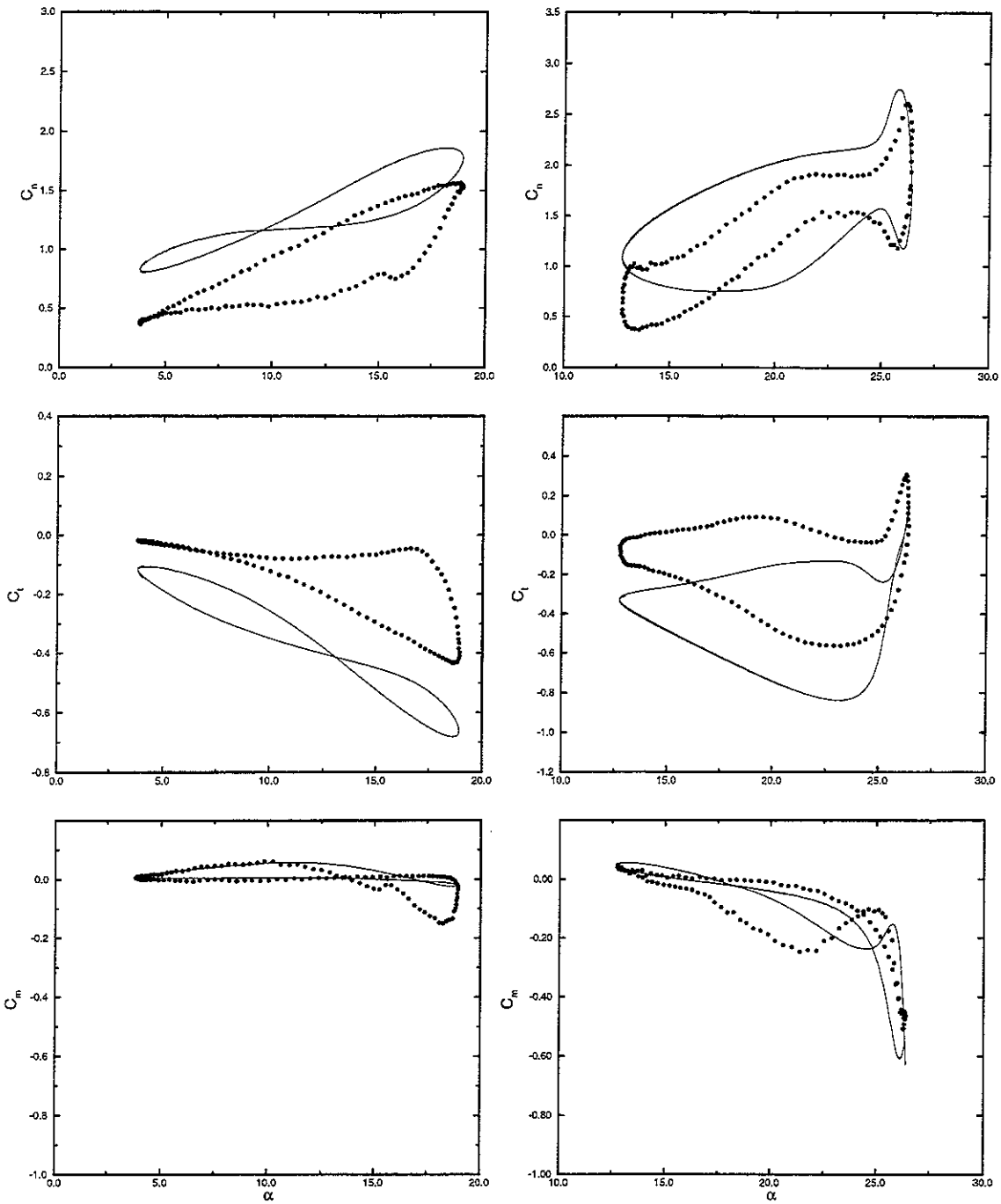

Figure 7.6: *Hysteresis curves for C_n, C_t, C_m for turbulent flow past a NACA 0015 airfoil calculated with the $K-\omega$-BSL turbulence model. Left:* $k = 0.102$, $\overline{\alpha} = 11.37^o$, $\Delta\alpha = 7.55^0$. *Right:* $k = 0.154$, $\overline{\alpha} = 19.58^o$, $\Delta\alpha = 6.83^o$.

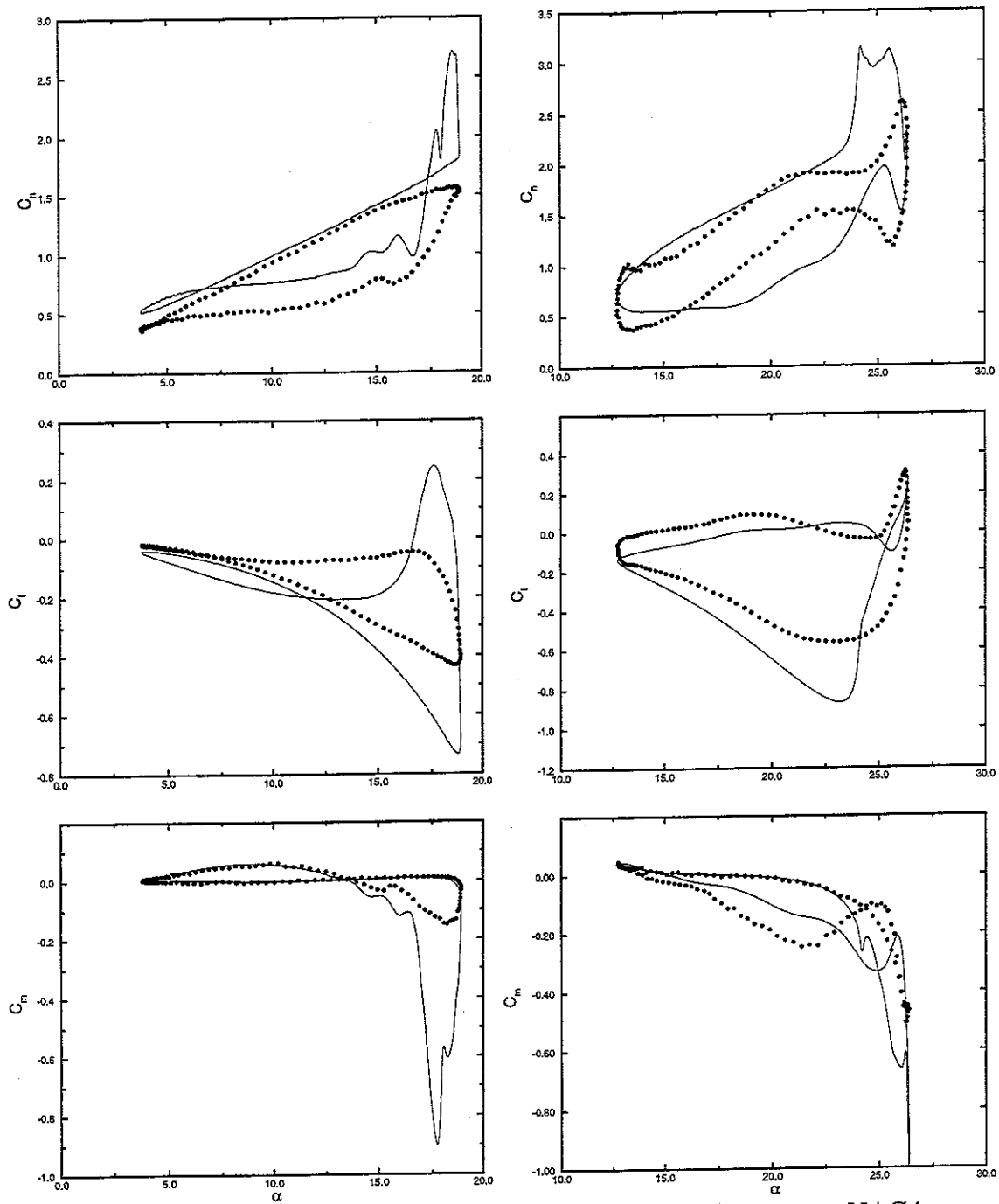

Figure 7.7: *Hysteresis curves for C_n, C_t, C_m for turbulent flow past a NACA 0015 airfoil calculated with the $K-\omega$-SST turbulence model. Left:* $k = 0.102$, $\overline{\alpha} = 11.37^o$, $\Delta\alpha = 7.55^o$. *Right:* $k = 0.154$, $\overline{\alpha} = 19.58^o$, $\Delta\alpha = 6.83^o$.

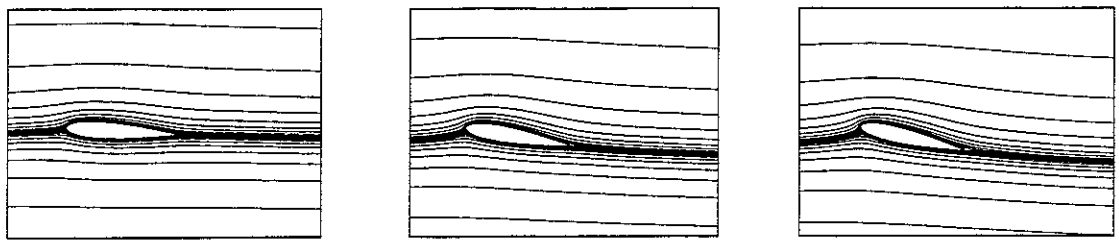

$(a) : 3.8^o \uparrow$ $(b) : 9.8^o \uparrow$ $(c) : 13.3^o \uparrow$

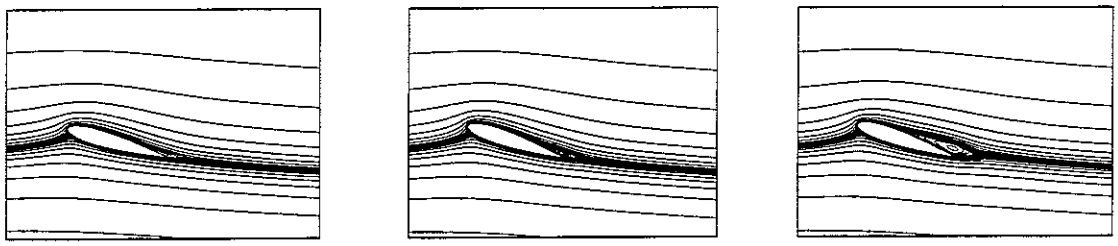

$(d) : 16.3^o \uparrow$ $(e) : 18.3^o \uparrow$ $(f) : 18.8^o \uparrow$

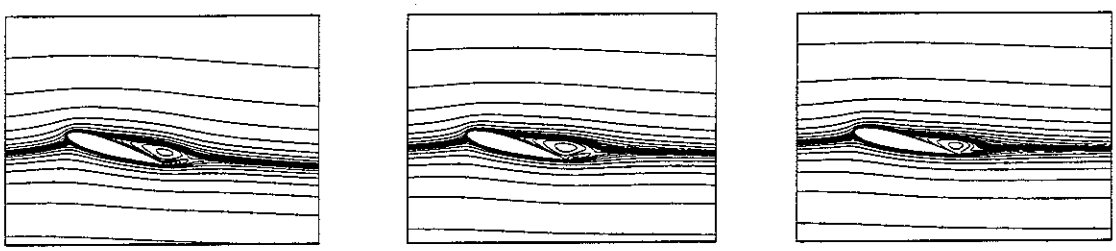

$(g) : 17.3^o \downarrow$ $(h) : 14.6^o \downarrow$ $(i) : 12.8^o \downarrow$

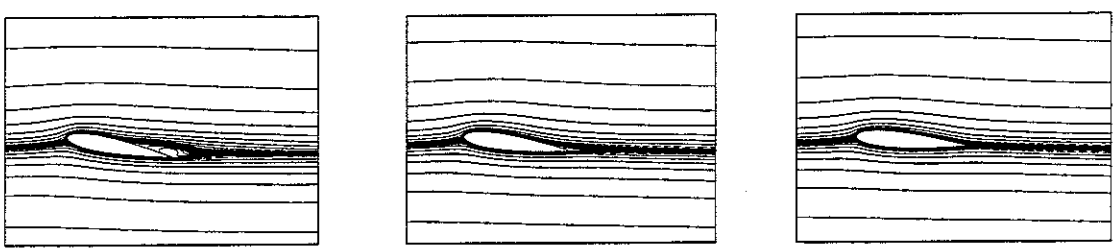

$(j) : 11.2^o \downarrow$ $(k) : 7.9^o \downarrow$ $(l) : 5.3^o \downarrow$

Figure 7.8: Instantaneous streamlines for an oscillating NACA 0015 obtained in the 2nd cycle. The flow is calculated with the SA turbulence model with a mean incidence $\overline{\alpha} = 11.37^0$ and amplitude of the oscillation $\Delta\alpha = 7.55^o$. The reduced frequency is $k = 0.102$ and the Reynolds number is $Re = 1.5$ million. (The letters are refering to Fig.(7.5)).

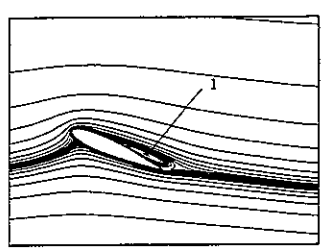

$(a) : 23.2^o \uparrow$

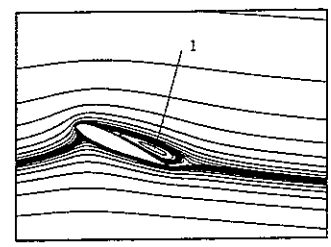

$(b) : 24.4^o \uparrow$

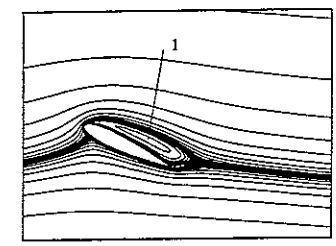

$(c) : 25.4^o \uparrow$

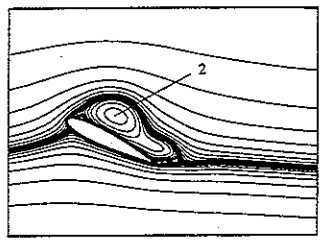

$(d) : 26.1^o \uparrow$

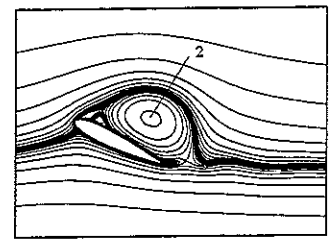

$(e) : 26.4^o \uparrow$

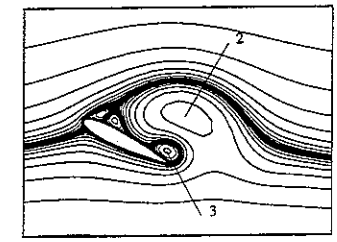

$(f) : 26.3^o \downarrow$

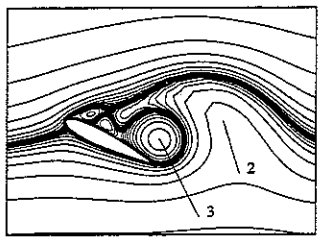

$(g) : 25.9^o \downarrow$

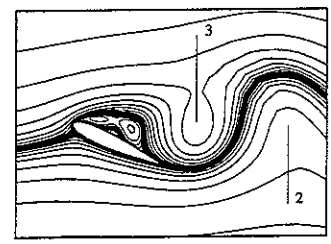

$(h) : 25.2^o \downarrow$

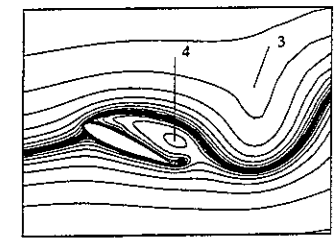

$(i) : 24.2^o \downarrow$

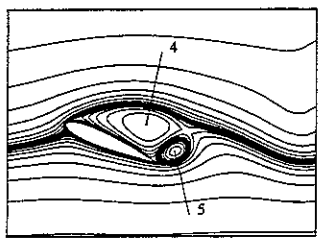

$(j) : 22.9^o \downarrow$

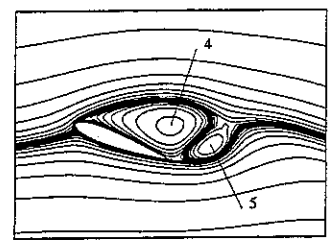

$(k) : 21.5^o \downarrow$

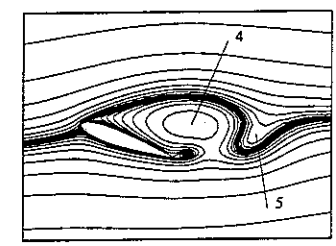

$(l) : 19.9^o \downarrow$

Figure 7.9: Instantaneous streamlines for an oscillating NACA 0015 obtained in the 2nd cycle. The flow is calculated with the BB turbulence model with a mean incidence $\overline{\alpha} = 19.58^o$ and amplitude of the oscillation $\Delta\alpha = 6.83^o$. The reduced frequency is $k = 0.154$ and the Reynolds number is $Re = 1.5$ million. (The letters are refering to Fig.(7.4)).

Conclusion

A 2-dimensional Navier-Stokes solver based on a vorticity and streamfunction has been developeds. Turbulence was simulated by time averaging the Navier-Stokes equations in primitive variable form, introducing vorticity and streamfunction based on mean values and adopting the eddy-viscosity concept for modeling the Reynolds stresses. The eddy-viscosity was calculated by utilizing the algebraic Baldwin-Lomax model, the 1-equations turbulence models by Baldwin & Barth and Spalart & Allmaras and the 2-equation $K-\omega$-BSL/SST turbulence model of Menter.

Boundary conditions for vorticity and streamfunction has been considered profoundly and a new method has been suggested for determining vorticity and streamfunction distributions at limiting boundaries of the calculation domain. This new method includes a pressure constrain derived from the primitive variable formulation of the Navier-Stokes equations and guarantees a unique pressure distribution on bodies, (a viscous Kutta condition), for flow in multiply connected regions. The method utilize a Base-function which only varies with the geometry of the flow configuration.

Three different laminar flow situations past a NACA 0012 has been considered, a stationary flow at moderate incidence, an impulsive start at high incidence and an airfoil oscillating in pitch between 0 and 20^o of incidence. In the stationary case a code to code validation showed that the pressure distribution was predicted slightly lower with the present formulation than with a primitive variable formulation. Nearly equal skin friction distribution was calculated with the two different Navier-Stokes solvers. The two unsteady laminar flow cases showed very good agreement when calculated instantaneous streamlines was compared with visualizations found in the literature.

As a basic test case for the Navier-Stokes solver a turbulent flow past a flat plate with rounded leading edge was regarded. It was found that the Navier-Stokes solver complemented by the five different turbulence models calculated

a symmetric flow with presence of a velocity distribution following the law of the wall closely. Comparisons of skin friction, boundary layer thickness and Reynolds number based on the momentum thickness with empirical relations showed good agreement. Finally, the convergence history of the different turbulence models was considered. It was found that the $K-\omega$ models was very numerical stable and could be applied with a larger time step than the algebraic and 1-equation turbulence models. The SA model was numerical very unstable. In the overall performance of the turbulence models when applied to a flat plate flow the $K-\omega$ model require smaller calculation time than the 1-equation models and only slightly more than the algebraic BL model.

A turbulent flow past a stationary Onera-A airfoil was calculated at incidences between 6^o and 40^o. Transition was enforced, at same position for all incidences, in accordance with experimental observations. The calculated flow was compared with experiments for three different incidences, two below stall and one at stall onset. In general all models underpredicts the lift below stall and over predicts lift at stall onset. Comparing Reynolds stresses and mean velocities indicate that the $K-\omega$-SST and the BB model is well suited for this type of airfoil flows.

The Michel criterion was applied to investigate the hypothesis of a fixed transition point for all incidences. Computations was performed at incidences 6^o, 8^o and 10.1^o and especially for the two highest incidences good agreement with the experimental estimated transition point was found. At higher incidences the Michel criterion could not be applied due to the presence of a leading edge separation bubble.

An impulsive start of a flow past a stationary Onera-A airfoil was computed for two incidences, $\alpha = 25^o$ and $\alpha = 40^o$. (Lift stall is experimental determined at an incidence around $\alpha \sim 17.6^o$). At incidence $\alpha = 25^o$ a stationary solution was predicted by the BB model whereas the BL, SA and $K-\omega$-BSL/SST models predicted an unsteady flow. For this incidence only limited influence from the applied turbulence models was found on the results. At incidence $\alpha = 40^o$ the influence on the flow situation from the different turbulence models applied vanished when turbulence transport models was applied. All turbulence transport models predicted the same oscillatory lift pattern and the solution became stationary after 40 non-dimensionalized seconds. The BL model did not predict a stationary solution in this case. Instead a constant oscillatory lift evolution in time was found. The SA model could not be applied in this case.

A turbulent flow past an NACA 0015 airfoil oscillating in pitch has been investigated. A light and deep stall case has been considered and the results obtained by the various turbulence models was compared with experimental results. In general very large different flow structures was found by utilizing the different turbulence models. The algebraic BL model fails to produce results in the vicinity of the measurements in both cases. The 1-equation models, BB and SA, gave the best results in both the light and deep stall case. The $K-\omega$-SST model predicted flow patterns comparable with experiments in the deep stall case but predicted non-physical results in the light stall case. The $K-\omega$-BSL model is believed to capture the major flow evolution in the deep stall case but predicted to little separation in the light stall case.

The new method to establish boundary distribution of vorticity and streamfunction has been tested for many different flow situations steady as well as unsteady flow cases. It is believed that the method clearly has made the vorticity-streamfunction formulation of the Navier-Stokes equations a valuable alternative to the primitive variable formulation when airfoil flows, especially in a non-inertial frame of reference, are considered. However, indication was found on a slightly underprediction of the pressure distribution for airfoil flows.

A possible extension of the present work is to enforce the no slip condition on solid surfaces explicitly and it could also be profitable to implement a local time stepping solution algorithm to lower the computation time needed for stationary computations. The new method to establish boundary distribution of vorticity and streamfunction is only tested for a single body in a multiply connected region. As the extension to several bodies in multiply connected regions is supposed to be straight forward a proof obtained by a calculation would definitely be appreciated.

Bibliography

[1] Andersen, C. F. Numerisk simulering af strømning omkring 2-dimensionale legemer. *Master thesis, Technincal University of Denmark, Department of Fluid Mechanics*, AFM-EP 92-07, 1992.

[2] Arpaci, V. S. and Larsen, P. S. *Convection heat transfer.* Prentice-Hall International, London, 1984.

[3] Baldwin, B. S. and Barth, T. J. A one-equation turbulence transport model for high reynolds number wall-bounded flows. NASA Technical Memorandum 102847 102847, NASA Ames Research Center, Ames Research Center, Moffet Field, California 94035-1000, 1990.

[4] Baldwin, B. S. and Lomax, H. Thin layer approximation and algebraic model for separated turbulent flows. *AIAA Paper*, 78-257, 1978.

[5] Baldwin, B.S. and Barth, J.T. A one-equation turbulence transport model for high reynolds number wall-bounded flows. *AIAA Paper presented at the 29th Aerospace Sciences Meeting, Reno Nevada*, AIAA 91-0610, Januar 7-10 1991.

[6] Beddoes, T. S. A qulitative discussion of dynamic stall. In *Special Course on Unsteady Aerodynamics.* AGARG Report No. 679, March 1980.

[7] Cebeci, T. Essential ingredients of a method for low reynolds-number airfoils. *AIAA Journal*, Vol. 27(No. 12):pp. 1680–1688, December 1989.

[8] Cebeci, T. and Smith, A.M.O. Analysis of turbulent boundary layers. *Series in Appl. Math. & Mech.*, Vol. XV, Acedemic Press, 1974.

[9] Chen, K.K. and Thyson, N.A. Emmons spot theory to flows on blunt bodies. *AIAA Journal*, Vol.9(No. 5):pp.821–826, May 1971.

[10] Cousteix, J. Basic concepts on boundary layers. *In AGARD Report: Special Course on Skin Friction Drag Reduction*, AGARD-R-786, March 1992.

[11] Daube, O., Loc, Ta Phouc, Monnet, P. and Coutanceau, M. Ecoulement instationaire decolle d'un fluide incompressible autour d'un profil: une comparison theorie-experience. *Conf. Poc. 386: Unsteady Aerodynamics-Fundamental and Applications to Aircraft Dynamics.*, 1985.

[12] Davis, R. L. and Carter, J. E. Three-dimensional viscous flow solutions with a vorticity-stream function formulation. *AIAA Journal*, Vol. 27(No. 7):pp. 892–900, July 1989.

[13] Deconink, H. Upwind methods and multidimensional splittings for the euler equations. In *Paper presented at the VKI LS 1991-01, Computational Fluid Dynamics*, 1991.

[14] Dick, E. A flux-vector splitting method for steady navier-stokes equations. *Int. Journal for Numerical Methods in Fluids*, Vol.8:pp. 317–326, 1988.

[15] Ekaterinaris, J. A., Srinivasan, G.R. and McCroskey, W. J. Present capabilities of predicting two-dimensional dynamic stall. paper no. 2. In *AGARD 75th FLUID DYNAMICS PANEL MEETING and SYMPOSIUM on AERODYNAMICS AND AEROACOUSITCS OF ROTOCRAFS*, October 1994.

[16] Galbraith, R. A. McD., Gracey, M. W. and Leitch, E. Summary of pressure data for thirteen aerofoils on the university of glasgow's aerofoil database. G.U. Aero Report 9221, University of Glasgow, 1992.

[17] Goldberg, U. C. Separated flow treatment with a new turbulence model. *AIAA Journal*, Vol. 24(No. 10):pp. 1711–1713, October 1985.

[18] Goldberg, U. C. Toward a pointwise turbulence model for wall-bounded and free shear flows. *Journal of Fluids Engineering*, Vol. 116:pp.72–76, March 1994.

[19] Haase, W., Brandsma, F., Elsholz,. E., Leschziner, M., and Schwamborn, D. *EUROVAL, A European initiative on validation of*

CFD codes., volume 42 of *Notes on Numerical Fluid Mechanics.* Vieweg Verlag, 1993.

[20] Hafez, M. Variational approaches to cfd: Applications to potential, euler and navier-stokes equations. *Paper presented at the Lecture Series held at the von Kaman Instute for Fluid Dynamics, VKI LS 1993-04*, 1993.

[21] Hansen, M. O. L. *Vorticity-velocity formulation of the Navier-Stokes equations for aerodynamic flows.* PhD thesis, Ph.D. dissertation, AFM 94-07, Department of Fluid Mechanics, Techninal University of Denmark., 1994.

[22] Hirsch, C. *Numerical Computation of Internal and External Flows, vol. 2.* John Wiley & Sons, 1994.

[23] Johansen, J. Simulering af strømning omkring stationært og oscillerende vingeprofil. *Master thesis presented at the Department of Fluid Mechanics, Technincal University of Denmark*, AFM-EP 93-09, 1993.

[24] Johnson, D.A. Transonic separated flow predictions with an eddy-visosity/reynolds-stress closure model. *AIAA Journal*, Vol. 25(No. 2):pp. 252–259, June 1986.

[25] Kim, S.-W., Zaman, K. B. M. Q., and Panda, J. Numerical investigation of unsteady transitional flow over oscillating airfoil. *Transactions of the ASME*, Vol. 117:pp. 10–16, March 1995.

[26] Launder, B.E. An introduction to single-point closure methodology. *Paper pressented at von Karman Institutes for Fluid Dynamics, LS 1993-02.*, February 1993.

[27] Leishman, J. G. and Beddoes, T. S. A generalized model for airfoil unsteady aerodynamic behaviour and dynamic stall using the indical method. *Paper presented at the 42nd. Annual Forum of the American Helicopter Society, Washington D. C.*, June 1986.

[28] McCroskey, W. J. The phenomenon of dynamic stall. *NASA Technical Memorandum 81264*, 1981.

[29] McCroskey, W. J. Unsteady airfoils. *Ann. Review of Fluid Mechanics*, vol. 14:pp. 285–311, 1982.

[30] McCroskey, W. J. and Pucci, S. L. Viscous-inviscid interaction on oscillating airfoils in subsonic flow. *AIAA Journal*, Vol. 20(No. 2):pp.167–174., February 1982.

[31] McCroskey, W. J., Carr, W. L. and McAlister, K. W. Dynamic stall experiments on oscillating airfols. *AIAA Journal*, Vol. 14(No. 1):pp.57–63, January 1976.

[32] Mehta, U., Chang, K.C. and Cebeci, T. Relative advatages of thin-layer navier-stokes and interactive boundary-layer procedures. *NASA Technical Memorandum 86778*, November 1985.

[33] Menter, F. R. Performance of popular turbulence models for attached and separated adverse pressure gradient flows. *AIAA Journal*, Vol. 30(No. 8):pp.2066–2072pp. 2066–2072, August 1992.

[34] Menter, F. R. Zonal two equation $k - \omega$ turbulence model for aerodynamic flows. AIAA Paper AIAA 93-2906, July 6-9 1993.

[35] Menter, F. R. Two-equation eddy-viscosity turbulence models for engineering applications. *AIAA*, 32(8):1598–1604, August 1994.

[36] Menter, F. R. A comparison of some recent eddy-voscosity turbulence models. *Transactions of the ASME*, Vol. 118:pp. 514–519, September 1996.

[37] Metha, U. B. Dynamic stall of an oscillating airfoil. *In : Unsteady Aerodynamic. AGARD CONFERENCE PROCEEDINGS No. 227*, 1977.

[38] Michel, R. Etude de la transition sur les profiles d'aile. *ONERA Report 1/1578-A, See White, F. M. Viscous fluid flow p.442.*, 1952.

[39] Mukhopadhyay, S. and Basu, B. C. Second-order accurate no-slip conditions for solving problems of incompressible viscous flows. *Journal of Computational Physics*, (No. 111):pp. 53–61, 1994.

[40] Nixon, D. A new explanation for the occurence of dynamical stall. In *AIAA Paper 95-2267*, 1995. Paper presented at the 26th AIAA Fluid Dynamics Conference, June 19-22, 1995/San Diego.

[41] Jaffe, N.A., Okamura, T. T., and Smith, A. M. O. Determination of spatial amplification factor and their application to prediting transition. *AIAA Journal*, Vol. 8(No. 2):pp. 301–308, February 1970.

[42] Oshima, H. and Ramaprian, B. R. Velocity measurement over a pitching airfoil. *AIAA Journal*, Vol. 35(No. 1), January 1997.

[43] Patel, V. C., Rodi, W. and Scheurer, G. Turbulence models for near-wall and low reynolds number flows: A review. *AIAA Journal*, Vol. 23(No. 9):pp. 1308–1319, September 1985.

[44] Peaceman, D. W. and Rachfors, H. H. The numeriacal solution of parabolic and elliptical differential equations. *SIAM Journal*, Vol. 3:pp. 28–41, 1955.

[45] Peyret, R. and Taylor, T. D. *Computational Methods for Fluid Flow.* Springer-Verlag New York Inc. ISBN 3-540-13851-X, 1990.

[46] Richardson, S. M. and Cornish, A. R. H. Solution of three-dimensional incompressible flow problems. *Journal of fluid Mechanics*, Vol. 82(part 2):pp. 309–319, 1977.

[47] Saffman, P. G. *Vortex Dynamics.* Cambridge University Press, 1992.

[48] Shen, W.-Z. and Loc, T.-P. A coupling fnite difference / particle method for the resolution of 2d navier-stokes equations in velocity-vorticity form. *To appear in Journal of Physics*, Submitted December 1994.

[49] Shen, When-Shong and Loc, Ta Phouc. Simulation of 2d external viscous flows by means of a domain decomposition method using an influence matrix technique. *International Journal for Numerical Methods in Fluids.*, Vol. 20.:pp. 1111–1136, 1995.

[50] Sørensen, N. N. *General Purpose Flow Solver Applied to Flow over Hills.* PhD thesis, Risø National Laboratory, Roskilde, Denmark, June 1995. Risø-R-827-(EN).

[51] Spalart, P. R. Direct simulation of a turbulent boundary layer upto $re_\theta = 1410$. *J.of Fluid Mechanics*, vol. 187:pp. 61–98, 1988.

[52] Spalart, P. R. and Allmaras, S. R. A one eqaution turbulence model for aerodynamic flows. *AIAA Paper 92-0439*, Januar 1992.

[53] Speziale, C. G. On the advantages of the vorticity-velocity formulation of the equations of fluid dynamics. Report CR-178076, ICASE 86/18, NASA Langley Research Center, Hampton, 1986.

[54] Stock, H. W. and Haase, W. Determination of length scales in algebraic turbulence models for navier-stokes methods. *AIAA Journal*, Vol. 27(No. 1):pp. 5–14, Januar 1989.

[55] Tennekes, H. and Lumley, J.L. *A first course in turbulence.* The Massachusetts Institute of Technology, ISBN 0 262 20019 8, June 1977.

[56] Thomas, J. L. and Salas, M. D. Far-field boundary conditions for transonic lifting solutions to the euler equations. *AIAA Journal*, Vol. 24(No. 7):pp. 1074–1080, July 1968.

[57] Tokunaga, H., Tanaka, T., Ichinose, K. and Satofuka, N. Numerical solutions of the incompressible flows in multiply connected domains by the vorticity-stream function formulation. *Computers Fluids*, Vol.23(No.2):pp. 241–249, 1994.

[58] Wachspress, E. L. *Iterative Solutions of Elliptic Systems.* Prentice Hall, 1966.

[59] White, F. M. *Viscous Fluid Flow.* 1952.

[60] Wilcox, D.C. Reasessment of the scale-determining equation for advaced turbulence models. *AIAA Journal*, Vol. 26(No. 11):pp. 1299–1310, November 1988.

[61] Wilcox, D.C. Comparison of two-equation turbulence models for boundary layers with pressure gradient. *AIAA Journal*, Vol. 31.(No. 8.):pp.1414–1421, August 1993.

[62] Wilcox, D.C. *Turbulence Modeling for CFD.* DCW Industries, Inc., ISBN 0-9636051-0-0, November 1994.

[63] Wu, J. C. and Gulcat, U. Separate treatment of attached and deattached flow regions in general viscous flows. *AIAA Journal*, Vol. 19(No. 1):pp. 20–27, 1979.

[64] Wu, J.-Z., Wu, X.-H., MA, H.-Y. and Wu, J.-M. Dynamic vorticity condition: Theoretical analysis and numerical implementation. *International Journal for Numerical Methods in Fluids*, Vol. 19:pp. 905–938, 1994.

[65] Yeo, W. R., Wood, P. E. and Hrymak, A. N. A numerical study of laminar 90-degree bend duct flow with different discretization schemes. *Journal of Fluids engineering*, Vol. 113:pp. 563–568, December 1991.

[66] Zhang, X. D., Trepanier, J.-Y., Reggio, M. and Camaro, R. Time-accurate local time stepping method based on flux updating. *AIAA Journal*, Vol. 32(No. 9):pp. 1926–1929, 1994.

Nomenclature

Roman

Symbol	Definition
a^+, a^-	coefficient in MUSCL approximation
A	boundary with no slip condition, airfoil boundary
A^+	van Driest damping constant
B	boundary of domain $\mathcal{O}$, inflow boundary in c-grid topology
B	additive constant in the law of the wall
c	chord length of airfoil
C^1, C^2, C^3	metric coefficients
C_1, C_2	overlapping region in c-grid topology
C_{b1}, C_{b2}	closure coefficient
C_{CP}	closure constant
C_d	drag coefficient
$CD_{K\omega}$	cross derivative for $K-\omega$ model
$C_{\epsilon 1}$, $C_{\epsilon 2}$	closure constants
C_f	friction coefficient
C_{Kleb}	closure constant
C_l	lift coefficient
C_m	moment coefficient
C_μ	closure coeeficient
C_n	normal pressure coefficient
C_p	pressure coefficient
C_t	tangential pressure coefficient
C_{w1}	closure constant
C_{wk}, C_{w1}	closure constant
D_1, D_2	outflow boundary in c-grid topology
D_1, D_2	van Driest damping function

Roman cont.

f	frequency
f_2, f_w	damping function
$\mathcal{F}$	term of production, destruction or viscous
F_1	blending function
F_{Kleb}	Klebanoff intermittency factor
g	limiter in SA model; constant in intermittency function
i	counter in the ξ direction
$\mathbf{J}$	Jacobian for the transformation $x, y \rightarrow \xi, \eta$
$\mathbf{J}^{-1}$	Jacobian for the transformation $\xi, \eta \rightarrow x, y$
j	counter in the η direction
J^{-1}	magnitude of J^{-1}
k	reduced frequency
K	turbulent kinetic energy
K_{Claus}	Clauser constant
l	length scale
$\mathcal{L}$	differential operator
$\mathbf{M}$	coefficient matrix for γ and derivatives of γ
n	direction normal to a boundary
nk	number of points along C
nx	number of gridpoints in ξ direction
ny	number of gridpoints in η direction
N	number of solid bodies
$\mathcal{O}$	domain limited by $A \cup B$
$\tilde{p}$	instantaneous pressure
P	time-averaged pressure; Production term in BB model
$\mathcal{P}$	source term
r	argument for damping function in SA model
Re	$\frac{U_0 c}{\nu}$, Reynolds number
R_t	turbulent Reynolds number

Roman cont.

s	direction tangential to a boundary
$\mathcal{S}$	magnitude of modified vorticity
S_γ	source term in momentum eq. for γ
t	time
T	time averaging period
U	time averaged velocity in x-direction
$\vec{U}$	mean velocity vector
U_0	free stream velocity
u_i	velocity fluctuation
U_i	time-averaged velocity
$\tilde{u}_i$	instantaneous velocity
$\mathcal{V}$	working variable in SA model
$\mathcal{V}^*$	$\mathcal{V}/\nu$
V	time averaged velocity in y-direction
W	time averaged velocity in z-direction
x_0	point of ratation
x, y	Cartesian co-ordinate
x^I, y^I	Cartesian co-ordinate in inertial coordinate system
$\mathcal{X}, \mathcal{Y}$	non-inertial coordinate system

Greek

Symbol	Definition
α	angle of attack
$\overline{\alpha}$	mean angle of attack
β, β'	closure constants
χ	constant determined by the viscous Kutta condition
δ	boundary layer thickness
δ_{ij}	Kronecker delta
δ^*	displacement thickness
Δ	finite-diference operator
$\Delta\alpha$	variation of attack
Δs	streamwise length
ϵ_{ijk}	permutation tensor
ϵ	dissipation of turbulent kinetic energy or $1 + \nu_t/\nu$
η	coordinate in a curvelinaer system
η_x, η_y	metric coefficients
γ	vorticity based on time-averaged velocity U
$\tilde{\gamma}$	instantaneous vorticity
γ'	vorticity based on instantaneous velocity $\tilde{u}$
Γ	closure constant
θ	momentum thickness
κ	von Karman constant
ν	kinematic viscosity
ν_t	eddy-viscosity
ν_t^*	ν_t/ν, eddy-viscosity nondimensionalzied with ν
ω	specific dissipation rate
Ω	angular velocity
Ω_{rot}	angular frequency
$\dot{\Omega}$	time derivative of Ω

Greek cont.

ϕ	set of closure constants
ϕ_e^+	reconstructed east cell face value for outflow
ϕ_e^-	reconstructed east cell face value for inflow
ψ	streamfunction which is a solution to the Navier-Stokes eqs.
$\overline{\psi}_A$	boundary condition for ψ on A
$\overline{\psi}_B$	boundary condition for ψ on B
ψ_1	streamfunction which not is a solution to the Navier-Stokes eqs.
ψ^+	$\psi_1 - \psi$
ρ	density of a fluid
$\sigma_e, \sigma_k, \sigma_\omega$	closure coefficient
τ_{ij}	Reynolds stress tensor
τ_{xy}	principal turbulent shear-stress
ξ	coordinate in a curvelinaer system
ξ_x, ξ_y	metric coefficients

Subscripts

Symbol	Definition
a	solid wall for a channel flow
b	solid wall for a channel flow
A	on a boundary with no slip condition
B	on a boundary with slip condition
δ	value at boundary layer edge
e	east cell face values
f	friction
i, j	note point i, j
max	maximum value
min	minimum value

Subscripts cont.

n	number of bodies
p	pressure
s	evaluated tangential to the airfoil
t	time differentation
te	tailing edge
θ	based on momentum thisckness
tr	transition
w	west cell face values
$wall$	evaluated along solid wall
x	differentation with respect to the x-direction
y	differentation with respect to the y-direction
η	differentation with respect to the η-direction
ξ	differentation with respect to the ξ-direction

Superscripts

Symbol	Definition
c	contra-variant component
I	value with respect an inertial reference system
k	time-station
$(\ )^+$	reconstructed cell face values for outflow
$(\ )^-$	reconstructed cell face values for inflow
$\dot{}$	first derivative with respect to t
$\ddot{}$	second derivative with respect to t
$+$	sublayer-scaled value
$*$	non-dimensionalized number

Auxilary

Symbol	Definition
arg	argument for a function
Res	Residual
$(\ )_{inner}$	value in inner part of boundary layer
$(\ )_{outer}$	value in inner part of boundary layer

Appendix A

Derivation of the vorticity-pressure coupling at a solid wall

In this appendix the derivation of the pressure-vorticity coupling will be derived for a laminar flow case. The extension to turbulent flow with an eddy-viscosity is straight forward.

At a solid wall the Navier-Stokes equations reduces to

$$\vec{P}_{x,y} = \begin{pmatrix} \frac{\partial P}{\partial x} \\ \\ \frac{\partial P}{\partial y} \end{pmatrix} = \begin{pmatrix} \frac{1}{Re}\left[\frac{\partial^2 U}{\partial x^2} + \frac{\partial^2 U}{\partial y^2}\right] \\ \\ \frac{1}{Re}\left[\frac{\partial^2 V}{\partial x^2} + \frac{\partial^2 V}{\partial y^2}\right] \end{pmatrix} \tag{A.1}$$

A vector $\vec{n}$ normal to the solid wall and a vector $\vec{s}$ tangential to the wall and orthogonal to $\vec{n}$ is

$$\vec{n} = \left(\frac{\partial x}{\partial n}, \frac{\partial y}{\partial n}\right) \quad , \quad \vec{s} = \left(\frac{\partial x}{\partial s}, \frac{\partial y}{\partial s}\right) \quad . \tag{A.2}$$

The vector product of $\vec{P}_{x,y}$ and $\vec{s}$ equals

$$\vec{P}_{x,y} \cdot \vec{s} = \frac{\partial P}{\partial s} = \frac{1}{Re}\left(\left[\frac{\partial^2 U}{\partial x^2} + \frac{\partial^2 U}{\partial y^2}\right]\frac{\partial x}{\partial s} + \left[\frac{\partial^2 V}{\partial x^2} + \frac{\partial^2 V}{\partial y^2}\right]\frac{\partial y}{\partial s}\right) \quad . \tag{A.3}$$

Vorticity is defined as

$$\gamma = \frac{\partial V}{\partial x} - \frac{\partial U}{\partial y} \quad , \tag{A.4}$$

and the x and y derivatives of γ equals

$$\frac{\partial \gamma}{\partial x} = \frac{\partial^2 V}{\partial x^2} - \frac{\partial^2 U}{\partial x \partial y} \tag{A.5}$$

$$\frac{\partial \gamma}{\partial y} = -\frac{\partial^2 U}{\partial y^2} + \frac{\partial^2 V}{\partial x \partial y} \tag{A.6}$$

which by use of the continuity equation reduces to

$$\frac{\partial \gamma}{\partial x} = \frac{\partial^2 V}{\partial x^2} + \frac{\partial^2 V}{\partial y^2} \tag{A.7}$$

$$\frac{\partial \gamma}{\partial y} = -\frac{\partial^2 U}{\partial x^2} - \frac{\partial^2 U}{\partial y^2} \ . \tag{A.8}$$

These derivatives of γ can be recognized as the terms inside the brackets of eq.(A.3) which now can be written in terms of these derivatives

$$\frac{\partial P}{\partial s} = \frac{1}{Re}\left(-\frac{\partial \gamma}{\partial y}\frac{\partial x}{\partial s} + \frac{\partial \gamma}{\partial x}\frac{\partial y}{\partial s}\right) \ , \tag{A.9}$$

or

$$\frac{\partial P}{\partial s} = \frac{1}{Re}\left(-\frac{\partial \gamma}{\partial y}\frac{\partial y}{\partial n} - \frac{\partial \gamma}{\partial x}\frac{\partial x}{\partial n}\right) \ , \tag{A.10}$$

because $\vec{n}$ and $\vec{s}$ are orthognal. The terms within the bracket of eq.(A.10) is identical to minus the normal derivative of γ

$$\frac{\partial \gamma}{\partial n} = \frac{\partial \gamma}{\partial y}\frac{\partial y}{\partial n} + \frac{\partial \gamma}{\partial x}\frac{\partial x}{\partial n} \ . \tag{A.11}$$

and by this

$$\frac{\partial P}{\partial s} = -\frac{1}{Re}\frac{\partial \gamma}{\partial n} \ . \tag{A.12}$$